RAPID SOLIDIFICATION OF STAINLESS STEELS AND FeAl ORDERED ALLOY

BY CAPACITOR DISCHARGE WELDING

Shankar Venkataraman
B. E., Madras University, 1984

A thesis submitted to the faculty
of the Oregon Graduate Center
in partial fulfillment of the
requirements for the degree
Master of Science
in
Materials Science and Engineering

September, 1986

The thesis "Rapid Solidification of Stainless Steels and FeAl Ordered Alloy by Capacitor Discharge Welding" by Shankar Venkataraman has been examined and approved by the following Examination Committee:

_____
Jack H. Devletian
Associate Professor
Thesis Research Advisor

_____
William E. Wood
Professor

_____
S. Shankar
Assistant Professor

_____
Anthony E. Bell
Associate Research Professor

ACKNOWLEDGEMENTS

TABLE OF CONTENTS

LIST OF SYMBOLS

Definition of parameters:

A   – fully austenitic solidification mode

AF   – austenitic-ferritic solidification mode

a   – cross sectional area

C_0 – composition of bulk liquid

C_L^* – composition of liquid at the solid-liquid interface

C_S^* – composition of solid at the solid-liquid interface

D   – diffusion coefficient

D_L – diffusion coefficient of solute at the interface

F   – fully ferritic solidification mode

FA   – ferritic-austenitic solidification mode

f   – fractional energy discharged in the welding arc

G   – thermal gradient

ΔG – free energy change

G_L – thermal gradient in the liquid at the interface

G_S – thermal gradient in the solid at the interface

G_C – concentration gradient at the interface

h   – stability parameter

K_L – thermal conductivity of liquid

K_S – thermal conductivity of solid

K   – average thermal conductivity $(K_L + K_S)/2$

k   – equilibrium partition coefficient

L   – total melt depth

l_s – solute diffusion length

l_t – thermal diffusion length

l_c – capillary length

m_L – slope of the liquidus line

P – solute Peclet number ρ/l_s

Q – activation energy

q – power density

R – growth rate

R_g – universal gas constant

ΔS – melting entropy

t – time

T – temperature

T_I – temperature of solid–liquid interface

T_m – melting temperature

ΔT_0 – solidification range

V_0 – velocity of sound in liquid metal

Γ – Gibbs–Thompson parameter $= \sigma/\Delta S$

θ – dendrite inclination angle to heat flow directio

λ_s – perturbation wavelength at the interface

λ_0 – primary dendrite arm spacing at $\theta = 0$

λ_1 – primary dendrite arm spacing

λ_2 – secondary dendtite arm spacing

ξ_c – solutal stability parameter

ρ – dendrite tip radius

σ – liquid–solid interfacial energy

Ω – supersaturation in the liquid at the dendrite tip

$$= (C_L^* - C_0)/C_L^*(1-k)$$

w – perturbation frequency

LIST OF TABLES

LIST OF FIGURES

Page

ABSTRACT

Rapid Solidification of Stainless Steels and FeAl Ordered
Alloy by Capacitor Discharge Welding

Shankar Venkataraman
Oregon Graduate Center, 1986

Supervising Professor: Jack H. Devletian

Capacitor discharge welding (CDW) is unique among joining processes
as it is the only one capable of producing joints up to 12 mm diameter
at cooling rates exceeding 10^6 K/s under a unidirectional temperature
gradient. The potential for microstructural modification by CDW was
therefore applied to joining of stainless steels and FeAl ordered alloy
to study solidification phenomena and to optimize CDW in producing high
cooling rates.

The materials used in this investigation included AISI grade 316,
304 and 308 having Cr Eq./Ni Eq. ratios of 1.49, 1.59, and 1.76 respect-
ively, and the high temperature ordered alloy Fe- 40at% Al. The alloys
were welded at different solidification rates by CDW and by conventional
gas tungsten arc welding for reference. Crystal and dendrite growth
morphologies were studied by optical and transmission electron micro-
scopy.

Under rapid cooling conditions, 316 and 304 alloys solidified in a
cellular/cellular dendritic mode as fcc austenite from the melt, while
308 solidified in a similar mode but as partly austenite and bcc
ferrite. Subsequent transformation of the 308 alloy took place comp-
letely to austenite by a massive transformation. The bcc alloy FeAl
also solidified in a single phase cellular structure.

Cooling rates during CDW varied between 10^6 and 5×10^7 K/s in stainless steel. Estimated growth rates were between 9.3 and 33.4 cm/s in stainless steel and between 4.8 and 11 cm/s in FeAl. Solute Peclet numbers were between 16 and 46 for stainless steels and between 1 and 2 for FeAl.

Primary and secondary dendritic spacings (λ_1 and λ_2 respectively) showed a power relation in stainless steels:

$$\lambda_2 \propto \lambda_1^{0.39}$$

λ_1 and λ_2 converged upon extrapolation at a dendrite arm spacing of $0.27 \mu m$. The variation of solute Peclet number with growth rate also indicated solidification close to absolute stability and convergence of primary and secondary dendritic spacings was attributed to proximity of the dendritic to cellular transition in stainless steels.

Dendrite morphology depended upon crystallographic orientation relative to the unidirectional gradient vector. Dendrite arm spacing and tendency for side arm growth increased with angle between primary dendrite/cell orientation and gradient vector. Equiaxed dendrites with an unusual morphology observed in FeAl welds, were nucleated by oxide inclusions present from prior powder consolidation processing.

Key variables in producing rapid cooling rates were identified as capacitance, voltage, stud diameter and ignition tip length. As an arc process, CDW was found to be a unique way to study rapid solidification phenomena.

I. INTRODUCTION

Control of segregation in metallic materials has been the goal of process metallurgists throughout the evolution of casting and welding processes. Suppression of segregation avoids problems like hot and cold cracking during processing, and susceptibility to corrosion and stress corrosion cracking, poor fatigue and impact properties while in service. Rapid solidification at rates of the order of 10^6 K/s was discovered by Duwez [1] to produce segregation-free and metastable alloys not possible by conventional techniques. These metastable cryst-alline structures and metallic glasses have much higher strength, wear and corrosion resistance than materials processed by traditional methods while still retaining high ductility. Since these materials have to be produced in small dimensions like foil, splats, powder or wire, consolidation is necessary in order to use them in the bulk form for engineering applications. Hence, production, consolidation, and joining of rapidly solidified crystalline materials without losing the meta-stable crystalline structures, grain refinement, etc., for structural applications is a much desired goal.

While the techniques of processing have advanced considerably, the fundamental problem of segregation and growth during conventional as well as rapid solidification has only recently gained attention [2]. From this angle, it is desired to predict the scale of segrega-tion, and the formation and stability of metastable structures.
Advances toward such a theory have been made for rapid solidification [3] and it is of interest to study its general applicability to process-ing of engineering alloys.

Stainless steels are among the most useful structural materials under severe environments requiring high reliability. Application of rapid solidification to austenitic stainless steels has been found to suppress hot cracking and improve strength [4]. A large amount of work has been done to characterise structures produced by varying compositions and cooling rates under conventional welding conditions [5-12]. By contrast, many interesting phenomena occurring during Rapid Solidification Processing (RSP) of these materials have not been fully explainable. Joining of powder processed and consolidated stainless steels is also an application where study is required.

Intermetallic ordered alloys like Ni_3Al have been known for high strength at elevated temperatures for many years [13]. Recently, attention has focused on equiatomic ordered aluminides of Fe, Co and Ni of the B2 crystal structure in order to utilise their low cost and excellent high temperature properties [14]. Their use is prevented by an extreme lack of room temperature ductility at present. Rapid solidification has been found as a promising means towards improving ductility in these alloys. Their weldability has not been studied so far. It is of great interest then, to study rapid solidification and joining of FeAl.

Capacitor discharge welding (CDW) has quite recently been found capable of very high cooling rates during solidification [15]. It is unique among joining processes in that it is the only one capable of producing joints upto 12 mm in diameter at cooling rates greater than 10^6 K/s. Here, it is necessary to study the CDW process with a view to obtain controlled cooling rates.

Thus, it is abundantly clear that a study of rapid solidification of stainless steels and FeAl intermetallic alloy by the CDW process is important due to the potential for microstructural modification and its application to joining of RSP materials, dissimilar metals, and composites, which are materials difficult to weld by conventional methods.

The objectives of the following study are therefore:

(a) To describe solidification phenomena and microstructures produced by rapid solidification during CDW of austenitic stainless steels and FeAl intermetallic ordered alloy at cooling rates greater than 10^6 K/s.

(b) To resolve the effect of composition and cooling rate on the solidification mode in austenitic stainless steels.

(c) To evaluate and optimize the CDW process as a means of attaining rapid solidification.

II. REVIEW

A. Rapid Solidification:

Evolution of solidification theory

Solidification structure and morphology have a profound effect on properties of metallic materials. Hence a lot of effort has been spent on the theoretical development to quantitatively and qualitatively define solidification [16–20] and these have been reviewed extensively [21–23]. In the capacitor discharge welding process, a substrate on which growth can occur is already available. It has also been established as a rapid solidification process (RSP) capable of cooling rates greater than 10^7 K/s [15,24]. Hence, in reviewing the developments in solidification theory, emphasis will be placed on free dendritic growth under unidirectional solidification. This is as opposed to nucleation limited processes like atomization and heat flow limited processes like splat and gun quenching. In that respect solidification during the CDW process is in many respects similar to that during laser and electron beam processing.

In the two-phase solidification process, we consider a single solid phase forming from a liquid. The known quantity in the system is usually the undercooling of the liquid ahead of the solid–liquid interface and it is required to predict the growth velocity and morphology of the solid. The mathematical definition of conditions at the interface are given [2,25] by:

(i) a model providing compositional relationships between the growing solid and the liquid at the interface

(ii) definition of the response of the interface to local

conditions of temperature, pressure, and composition

(iii) relations describing heat flow

(iv) relations describing solute diffusion across the interface.

Thermodynamically, growth of the dendrite can be related to the under-cooling. The three factors causing undercooling are:

a) the thermal gradient at the interface

b) constitutional supercooling

c) capillary forces at the dendrite tip.

and are expressed in terms of the characteristic lengths [26]:

$l_s = 2D_L/R$, is the solute diffusion length,

$l_t = k \Delta T_0/G$, is length due to thermal diffusion,

and $l_c = \Gamma \Delta T_0 k$, the capillary length,

where D_L is the diffusion coefficient of solute in the liquid. The Gibbs-Thompson parameter Γ, is the ratio of solid/liquid interfacial energy to the melting entropy, and ΔT_0 is the solidification range. k and R are the equilibrium partition coefficient and growth rate respectively. Two dimensionless quantities can be obtained from the above lengths. To completely define dendrite growth, it was found that the tip radius ρ has to be considered in a third dimensionless parameter called the Peclet number:

$$P = \rho/l_s = R\rho/2D,$$

where P is the Peclet number. The undercooling can be expressed as a function of these dimensionless quantities.

One of the first attempts to analyze dendrite growth mathematically was by Ivantsov [27,28], who assumed a parabolic shape for the dendrite

and neglected capillary forces at the dendrite tip. Rutter and Chalmers
[16] developed the constitutional supercooling theory and a corresponding
criterion for stability of the growing dendrite, considering the heat
and mass flow across the interface. The other assumptions used in their
analysis were:

* no convection in the liquid

* diffusional mixing present in the liquid, diffusion in the solid
  being neglected

* steady state conditions

* equilibrium at the liquid-solid interface.

The solute buildup at the interface in the liquid at steady state is
C_0/k, from the phase diagram. The concentration gradient is then given
by:

$$(dC_L/dx)_{x=0} = RC_0(1-k)/kD_L \qquad (1)$$

C_L and C_0 are the compositions of the liquid at distance x from the
interface and that of the bulk liquid respectively. The equilibrium
liquidus temperature T is related to the liquid composition C_L by the
slope of the liquidus line m_L:

$$(dT/dx)_{x=0} = m_L (dC_L/dx)_{x=0} \qquad (2)$$

Constitutional supercooling occurs when the actual temperature gradient
G_L is less than or equal to (dT/dx). Combining (1) and (2), a planar
interface is stable when

$$G_L/R \geq - m_L C_0(1-k)/kD_L \qquad (3)$$

This is the simple constitutional supercooling criterion for stability
derived by Rutter and Chalmers. The analysis of variation in solid
composition during directional solidification was done by Chalmers

et al. [17], including the effects of convection and changes in R. A sound mathematical basis was laid to stability analysis by Mullins and Sekerka [18], who considered undercooling due to all three effects mentioned previously. While the simple constitutional supercooling criterion predicts instability for all velocities exceeding the criterion for a particular value of gradient, the Mullins-Sekerka analysis also predicts stabilisation of a planar interface at high velocities, when surface tension predominates. They termed this phenomenon absolute stability because stability in this regime is independent of the gradient as well as velocity.

In this analysis, a sinusoidal perturbation was imposed upon a planar interface. Considering the undercooling at the interface, a stability function f(w) was derived. Since the thermal gradient in the solid G_S and that in the liquid G_L close to the interface can be different, the stability criterion is given by:

$$- (G_S+G_L)/2 + m_L G_C > h \quad \text{unstable}$$

$$< h \quad \text{stable} \qquad (4)$$

where h is the maximum of the stability function |max f(w)|, and G_C is the composition gradient in the liquid. This theory predicts that the capillary component of the stability function predominates at high perturbation frequencies (at high w) and absolute stability occurrs when

$$R \geq (k-1)m_L C_o D_L/k^2 \Gamma \qquad (5)$$

Γ is the ratio of the liquid-solid interface energy to the melting entropy. The Mullins-Sekerka theory does not predict steady state dendrite growth and is valid only for small amplitude perturbations.

Several theories were developed to optimise dendrite growth using assumptions of maximum growth velocity or minimum undercooling and minimum rate of entropy production [29,30], but were not found to hold for experimental verification [26,31]. Langer and Muller-Krumbhaar [20] proposed a Mullins-Sekerka stability condition applicable at the dendrite tip to replace the maximum velocity assumption. Thus, the dendrite assumes a tip radius that allows it to be marginally stable as determined by the Mullins-Sekerka criterion. This theory has been found to represent true dendrite growth by several studies [31-33]. The above stability analyses can be summarised [23] in an overall stability criterion :

$$\frac{m_L G_c (w^* - R/D_L)}{[w^* - (1-k)R/D_L]} - \Gamma w^2 - \frac{K_S G_S + K_L G_L}{2K} = 0 \qquad (6)$$

$w^* = R/2D_L + [(R/2D_L)^2 + w^2]^{1/2}$, where $w^2 = w_x^2 + w_y^2$ and w_x and w_y are spatial perturbation frequencies. K_S and K_L are the thermal conductivities of the solid and liquid and K is their mean. The interface is stable when the sum of the three terms in (6) < 0.

Stability during Rapid Solidification:

The morphological stability theory is thus seen to integrate thermal, solutal, and capillary effects to predict stability. At high growth rates, stability is predominantly a function of solutal and capillary effects, when thermal gradient effects are negligible. Stability diagrams can be drawn [23,34] showing stability-instability regimes as functions of composition, thermal gradient and growth rate as shown in Figs. 1 and 2. The limit of planar interface stability is given

by the constitutional supercooling criterion at low velocities eq. (3) and in the limit of high velocities by the absolute stability criterion eq. (5). In Fig. 2, the corresponding lines are approximations of eq. (6) which is applicable at the limit of stability. It can be seen that the approximations are good at low and at high velocities. At high velocities, eq. (5) is valid only when the following conditions are met [35]:

(a) The thermal gradient at the interface

$G^* = (K_L G_L + K_S G_S)/(K_L + K_S) > 0$, or, when the heat flow is towards the solid.

(b) The equilibrium partition coefficient k is applicable. This condition will be considered in detail under non-equilibrium effects.

(c) The velocity must be sufficiently far from the limit of constitutional supercooling for the approximation of (5) to be valid, as can be seen from Fig.2.

In surface melting and welding, condition (a) is valid. Condition (c) is valid for most engineering alloys and becomes important for very dilute compositions. The major factors to be considered while applying equation (5) are then, metastable phase formation and departure from equilibrium, which affect condition (b).

Use of Metastable Phase Diagrams

At high solidification rates, the nucleation and/or growth of a thermodynamically stable phase may be competitively suppressed. In such cases, the possible metastable phases can be predicted by

metastable extensions of the equilibrium curves [36]. In growth of eutectics from the melt, it was observed that at high velocities the second phase does not nucleate. This was observed in binary Ag-Cu alloys [3,37] and was also reported in stainless steels [4], which is a ternary system with a two phase eutectic. Metastable extensions of liquidus and solidus curves showed that at high undercoolings, the equilibrium partition coefficient k and liquidus slope m_L may no longer be valid and must be estimated by considering such an extension.

Non-Equilibrium Effects:

Traditional solidification treatments assumed a condition called local equilibrium by which the interface compositions of solid and liquid correspond to an appropriate equilibrium diagram [25]. At high interface velocities approaching the order of the diffusion velocity, it was found that solute concentrations much higher than the solubility limit were observed. Under such conditions, calculations showed that the chemical potential of the excess or 'trapped' solute increased instead of being the same as that of the solvent [38]. This is a departure from equilibrium. Many models have been proposed to predict solute trapping [25,39,40], and the analyses lead to a nonequilibrium partition coefficient given by:

$$k(R) = (k + a_0 R/D_L)/(1 + a_0 R/D_L) \qquad (7)$$

a_0 is a length scale related to the interatomic distance and is estimated to be between 0.5 and 5 nm [3]. The interface velocity can be related to the interface temperature T_I:

$$R = -V_0(\Delta G/R_g T_I) \qquad (8)$$

V_0 is the speed of sound in the liquid metal, ΔG is the molar free energy of solidification R_g is the gas constant and equations (7) and (8) are response functions. Equation (7) can be used to obtain the velocity dependent partition coefficient in equation (5) if the rate of change of k with velocity is relatively small, and/or the absolute value of the rate of change of interface temperature with velocity is relatively large [35]. When the rate of change of interface temperature with velocity is relatively small, large variations in velocity are possible for a given undercooling at a capillary stabilised growth front. Coriell and Sekerka [41] predict that in such cases, significant variations in interface velocity which cause lateral segregation with large wavelengths that cannot be stabilised by capillary forces, can occur. The analysis also indicates the instabilities to be oscillatory in time. In such a case, the absolute stability condition will not be valid. Further, the non-equilibrium partition coefficient in equation (7) is derived only for dilute solutions and no composition dependence is taken into account. Hence its validity in predicting departure from equilibrium for concentrated alloys may be limited.

Another important consideration in rapid solidification is the temperature dependence of diffusion coefficient. It has been shown that order of magnitude changes in D_L can be caused by changes in interface temperature [35]. In that case, the usual Arrhenius type equation can be used:

$$D_L = D_0 \exp[-Q/R_g T] \tag{9}$$

where Q is the activation energy for solute diffusion, D_0 is a proportionality constant. Agreement has been found to within a factor of

2-3 for predictions of stability using equation (5) in Ag-Cu alloys by considering non-equilibrium effects and metastable thermodynamics [3].

Dendrite Growth and Spacing:

Dendrite growth is recognized as a combination of steady state tip growth and time dependent growth of side branches superimposed upon each other [42]. Complex mathematical analysis is required to derive relations between G, R, and observable features of dendrite growth, namely dendrite arm spacings. Hence, to obtain a useful form of the solution, approximations have been made for special cases of the problem. The case of rapid solidification in a positive thermal gradient was treated by Kurz et al. [3].

The marginal stability condition is assumed to hold at the dendrite tip and the tip radius is approximated to be the same as the wavelength λ_s of a planar solid-liquid interface at the limit of stability. By the Mullins-Sekerka analysis, the wavelength of a marginally stable perturbation at a plane interface is given by:

$$w^2 \Gamma = mG_c \xi_c - G \qquad (11)$$

where $w = 2\pi / \lambda_s$, and ξ_c is a dimensionless parameter which is a measure of instability due to solutal effects.

$$\xi_c = 1 - \frac{2k}{[1 + (2\pi/P)^2]^{1/2} - 1 + 2k} \qquad (12)$$

From (11) we have,

$$\rho = 2 \frac{\Gamma^{1/2}}{[mG_c \xi_c - G]^{1/2}} \qquad (13)$$

The temperature gradient in eq. (13) is determined by heat flow. The concentration gradient G_c depends upon the actual composition of the liquid at the interface, C_L^*:

$$G_c = RC_L^*(1-k)/kD_L \tag{14}$$

From the definition of supersaturation Ω and that of the Peclet number P, we have

$$C_L^* = C_0/[1-(1-k)\Omega]$$
$$= C_0/[1-(1-k)Iv(P)] \tag{15}$$

$\Omega = Iv(P)$ is the Ivantsov solution to the transport problem at the dendrite tip and $Iv(P) = Pexp(P)E_1(P)$, values of which are available as functional tables [43]. Combining (13) and (14), we have a quadratic in R :

$$R^2A + RB + C = 0 \tag{16}$$

where $A = \pi^2\Gamma/P^2D_L^2$, $B = mC_0(1-k)\xi_c/D_L[1-(1-k)Iv(P)]$, and $C = G$. Equation (16) can be solved by numerical techniques for a particular system to obtain a series of Peclet number-growth rate curves at different G values as shown in Fig.3.

The Peclet number-growth rate curve consists of a gradient dependent part at low velocities and becomes independent of gradient at velocities close to absolute stability. The cellular to dendritic transition was predicted [32] and shown [44] to be at $R = GD_L/k_0\Delta T_0$, which is the transition point in the above mentioned curve between the gradient dependent and gradient independent portions. At high velocities, a transition form dendritic to cellular mode has been observed [37], and is correlated with a sharp increase in ρ and P at velocities close to absolute stability [3]. Variation of tip radius ρ with

velocity was shown to be of the form $R\rho^2$ = constant for low and intermediate velocities. Dendrite tip radius increases at the dendritic-cellular transition, and at absolute stability tends to infinity, as capillary stabilization results in a planar interface.

Relating Solidification Parameters to Structure:

Interdendritic spacing has long been used to relate freezing conditions to structure. Linear relationships were found for steels and Al alloys with local solidification times spanning several orders of magnitude, versus primary and secondary dendrite spacings [21]. Relationships are also available for Al alloys and Pb-Sn and Zn alloys [45-51]. Coarsening kinetics and convection during the experiments were found to change the results appreciably [42,52], which was also evidenced by inconsistency between results from independent studies. The nature of the growth relationships was not qualitatively known in terms of system independent parameters, and it was found necessary to study tip temperature and undercooling with respect to growth velocity. Burden and Hunt [29] found the tip temperature to go through a maximum as growth rate is increased. As a result of further work, Hunt [53] and Kurz and Fisher [32] derived expressions relating solidification parameters to dendrite and cell spacings:

$$\lambda_1 \propto R^{-1/4}G^{-1/2} \tag{17}$$

Fair agreement with the above relation was reported for directionally solidified superalloys [51]. Data on succinonitrile also indicate that the slope of the variation in dendrite arm spacing agreed with Equation 17, eventhough the actual points did not correspond to

derived expressions by Hunt [53] and Kurz and Fisher [32]. The expression by Trivedi [54] does not correspond with experimental spacings at high growth rates, in spite of its considerable mathematical complexity. Trivedi and Somboonsuk [33] showed that primary arm spacing was much less subject to coarsening with time than secondary dendrite arm spacing. Secondary arm spacing was found to be sensitive to coarsening kinetics as well as variations in local G and R conditions beyond eight spacings from the tip. The initial secondary arm spacing λ_2 was found to be equal to 2ρ for a wide range of compositions and to be a function of alloy composition and solidification velocity only. Analysis due to Langer and Muller-Krumbhaar gave a relationship of the form $R\rho^2$ = constant. A more complete expression was derived by Kurz et al., [3] without the approximations used by the former.

$$R\rho^2 = \frac{4\pi^2 D_L \Gamma [1-(1-k)Iv(P)]}{C_0 m_L (k-1)\xi_c} \tag{18}$$

This function is nearly constant upto velocities close to absolute stability, whereupon it sharply rises to infinity as ρ rises to infinity. Thus, λ_2 can be directly related to R by the above relation in the high velocity regime where ρ and λ_2 are independent of G.

While considerable progress has been made for binary solidification and also for binary eutectics, multiphase solidification is still difficult to define, particularly when several components are involved. Approximation to binary solidification may be possible in the case of many single phase commercial alloys but limitations will be imposed by the accuracy of material constants k, m_L, and D_L. Empirical curves

must be used till the analytical solutions discussed are found capable of universal application.

B. Microstructure and Solidification:

Austenitic Stainless Steels:

Austenitic stainless steels are an important class of alloys in the Fe–Cr–Ni ternary system. Detailed phase diagram data is available for this system [55]. Most compositions of engineering interest occur approximately at the 70% Fe section of the ternary diagram (Fig. 34), which is of the two phase eutectic type [4,5,56]. Katayama et al. [5] have given extensive treatment of solidification modes and compositions in these stainless steels. Solidification paths for most commercial alloys fall around the eutectic trough, giving rise to fully austenitic, primary austenitic eutectic, eutectic, primary ferritic–eutectic and fully ferritic solidification modes. The solidification mode is very important in casting and welding of these alloys since it has been found to affect hot cracking and corrosion resistance.

A characteristic feature of eutectic and/or ferritic steels is the solid state transformation that the primary ferrite undergoes as it crosses the curved austenite solvus boundary. Depending on the composition and the time allowed in the austenite–ferrite two phase region, the ferrite present transforms to a fully austenitic equilibrium structure. This transformation has been studied and has been postulated as being diffusional as against a massive type reaction [6–8]. Its diffusional nature at cooling rates typical of conventional welding conditions has been established [9,56]. The interpretation of solidifi-

cation structures is complicated by the occurrence of the solid state reaction. Further, the presence of several alloying elements including the interstitial elements C and N has a profound effect on the phase diagram. The Schaeffler and DeLong calculations [10] of Cr/Ni equivalents are commonly used to account for the above, though alternatives have been suggested [12]. These empirical diagrams relate ferrite content to composition under typical welding conditions. It was found that ferrite content during solidification goes through a maximum as cooling rate is increased in slow cooling GTA welds and decreases again for higher cooling rates. Welds in 304 grade stainless steel showing 5% ferrite in GTA welds showed no ferrite under laser and capacitor discharge welding conditions with cooling rates exceeding 10^4 K/s [15].

Rapid solidification in stainless steels revealed several interesting effects. Vitek et al. [4] found that splat quenched and laser melted 308 steel showed completely austenitic solidification at cooling rates between 10^5 and 10^6 K/s. It was explained in terms of a partitionless transformation to austenite by extension of the T_0 curve. Studies were done on powder processing of 303 stainless steel [57] by Kelly et al. Their thermodynamic phase stability calculations for 303 steel showed that the free energy curves versus temperature for austenite and ferrite phases were close together in the temperature range of solidification. It was found that depending on the undercooling reached in the droplet, it solidified as either fcc or a metastable bcc structure.

Defect structures during splat quenching which could affect mechanical properties and nucleation of second phases, have also been

observed. Wood and Honeycombe [58] found cell boundaries in splat quenched austenitic steel decorated by vacancy dislocation loops. Nishi et al. [59] studied the effect of cooling rate on dislocation density in splat quenched 18-8 type stainless steel and found a linear increase in dislocation density with reciprocal cooling rate.

Empirical relationships exist between dendrite arm spacing and cooling rate for austenitic steels. The relationships by Grant [50] for secondary arm spacings and by Okamoto [60] for primary arm spacings are for cooling rates in the range 10^{-1} to 10^5 K/s. It is therefore seen that the relationship between solidification structure, solid state transformation and composition is not fully understood in stainless steels of engineering interest at high cooling rates.

Rapid Solidification in FeAl:

Equiatomic ordered aluminides are considered potentially useful materials for aerospace applications due to their excellent properties at high temperatures [61]. Extreme lack of room temperature ductility has been a problem which resists solution and the use of Fe, Co and Ni aluminides. Eventhough favorable slip systems exist in the B2 structure, intergranular brittleness is responsible for near zero ductility at room temperature. Attempts to rectify this problem have used microalloying and/or rapid solidification to effect improvements [62-64]. In NiAl a sharp increase in ductility was found when grain size was reduced below a critical value of 20 microns [65]. Though the grain size reduction in that study was obtained by thermomechanical treatment, rapid solidification was also found to produce the same

result. Addition of boron resulted in a slight improvement in ductility of FeAl, though not to the extent achieved in Ni$_3$Al [66]. Splat quenching of FeAl and NiAl revealed that FeAl showed greater bend ductility than NiAl in the 40-50 % Al range. The ductility was also found to improve dramatically with heat treatment [67]. David et al. [68] studied weldability of Ni$_3$Al type nickel-iron aluminides and found limited weldability by electron beam welding. Very little is known on weldability of FeAl and it is of interest to examine the effect of rapid solidification by the CD process on structure.

C. Process Considerations:

Capacitor discharge stud welding is a high production rate process for welding fasteners on to sheet, of particular importance to the transportation industry. Besides high speed, the advantages of CDW include welding to thinner plate than possible by other conventional processes, welding of dissimilar metals and different sized components [69-71]. The extremely intense arc and low heat input account for very small fusion and heat affected zones, producing a high efficiency joint.

A review of the literature on CDW has been done by Chvertko [72] and includes a good description of the sequence of events occurring during the process. The rapid melting and resolidification occurring is similar to that during laser melting. Heat flow analysis has been done for laser melting by a stationary pulse [23,73,74], based on a unidirectional heat flow model. Mehrabian [23] found that a laser melted spot of radius a subject to power density q in aluminum will solidify under

unidirectional heat flow if $qa \geq 1.9 \times 10^6$ W/m. The cooling rate was found to vary directly and the melt depth inversely as the absorbed power, on a logarithmic scale [73,74]. The heat flow calculations revealed a relationship between time t after application of power density q versus melt depth [73]:

$$L/L_{max} \propto qt^{1/2} \tag{19}$$

A similar parabolic dependence of interface position upon solidification time has been found in splat quenching for the case of ideal cooling [75,76]. In splat quenching, the inverse relationship between thickness and cooling rate is also well known [59,75,76]. Though a few scientific studies of microstructures produced by CDW exist [77,78], the potential advantages offered by rapid solidification joining were only recognized recently [15]. Thus, the CDW process offers an open field for investigation.

III. PROCEDURE

A. Material Preparation:

Materials used in this study included 304, 308 and 316 stainless steels and FeAl ordered alloy. The compositions of the stainless steels used are given in Table 1. The 316 alloy was available as 16 mm thick sheet and was turned down to required diameter so that the rolling direction was along the axis of the rods to be welded. Alloy 304 was obtained as 6.4 mm diameter rod and 308 alloy, which is a designated weld filler wire, was gas tungsten arc deposited on to 6.4 mm diameter stainless steel rod and machined to dimension. The GTA weld deposited 308 alloy was treated at 1100°C for 8 hrs to transform retained ferrite to austenite.

The FeAl intermetallic ordered alloy was obtained in the hot extruded form from atomised and consolidated powder. The nominal composition of the alloy was Fe-40at% Al. Wafers cut from hot extruded bar were welded on to 6.4 mm diameter steel rod and turned down to the required diameter. Again, the extrusion direction was along the axis of the rod to be welded.

B. Capacitor Discharge Welding:

The initial gap capacitor discharge process was used to produce the welds. Figure 4 shows the H. A. Jones PSW stud welder, the controls for which were:

Capacitance	:	8–320 mF
Voltage	:	45–175 V

Stud Drop Height   :   0-100 mm

Drop weight   :   22-284 N

A schematic diagram of the arrangement of the components before welding is shown in Figure 5. Welds can be made to join rod to rod, or to sheet. In the initial gap capacitor discharge process, the stud on which the ignition tip is machined, is dropped on to the component to be joined to, either by gravity or by pneumatic/spring force. A capacitor bank charged to a preset voltage is allowed to discharge through the ignition tip and strike an arc to cause melting between the components to be joined. When they come into contact, the arc is extinguished. Solidification occurs as excess liquid is spattered out upon impact of the mating components, to produce a joint. The weld typically occurs in a time of 1-2 ms.

All welds in the present study were made rod to rod. Conical ignition tips of the required length were machined on to the negative electrode. Table 2 gives the conditions used to produce different welds and their designations. Current and voltage profiles were recorded during welding by Sony-Tektronix Digital Storage Oscilloscope #336 and plotted out by an X-Y recorder. Current was measured by measuring the voltage across a shunt connected in series with the welding cable. The components were weighed correct to 10^{-5}g before and after joining. Alloys 316, 304 and 308, and FeAl were designated as A, B, C, and D respectively.

Gas tungsten arc welds were made in the three stainless steels and FeAl ordered alloy and examined by optical metallography. Ferrite contents in stainless steel GTAW were measured by Ferrite Scope.

C. Analysis:

Optical Metallography:

All welds were sectioned longitudinally across the diameter of the rod for optical microscopy. After fine grinding, jet electropolishing and etching of stainless steel were done using an electrolyte of 33% water, 55% phosphoric acid, and 12% sulfuric acid. Polishing occurred at 20 to 25 V for 10 to 20 seconds and etching was done at 1.5 to 2 V for 60 seconds. Both dendrite and grain structures of stainless steel were observable by this method.

After conventional polishing, FeAl was etched with the solution used by David et al [68]: 20% water, 20% phosphoric acid, 20% nitric acid, and 10% hydrofluoric acid. Again, the dendrite and grain structures were revealed for examination.

Optical metallography was done using Nomarsky interference contrast and standard equipment. Dendrite arm spacings were measured using a calibrated scale eyepiece graduated to $0.29\mu m$ at 1810X.

TEM Specimen Preparation:

Cross sectional wafers were cut from 304 stainless steel weld B2 and mechanically thinned to 100 μm thickness. Discs 3 mm in diameter were punched out and twin jet electropolished to electron transparency with 30% nitric acid in methanol, at 15 V and 0°C. The section was observed in a Hitachi HU-200 electron microscope.

IV. RESULTS

The effects of process parameters on solidification structure during CDW were identified in a preliminary study. Welds were made on stainless steel and FeAl ordered alloy using conditions derived from the preliminary study. The following sections show microstructures produced in stainless steel and FeAl ordered alloy. Subsequently, heat flow in relation to dendrite growth, and effects of crystallographic orientation on dendrite growth and spacing are presented. Lastly, arc characteristics observed during welding of stainless steel and FeAl are shown.

A. Parametric Study of the Capacitor Discharge Process:

Weld thickness was identified as a significant factor in producing rapid solidification during welding, since reduced dimensions along heat flow directions are known to be critical in rapid solidification processing [50]. Accordingly, an experiment was conducted to find the effect of weld parameters on thickness in order to minimize weld thickness and maximize cooling rate. Discharge voltage, ignition tip length, drop height and drop weight were varied in a factorial experiment at two levels. In all cases welds were made on 6.3 mm diameter stainless steel rod using straight polarity and 80 mF capacitance. The baseline settings for the initial study were as given below:

Capacitance (mF)	Voltage (v)	Ignition Tip Length (mm)	Drop Height (mm)	Drop Weight (N)
80	90	1.02	51	60

All experimental settings other than control variables were baseline values. A complete table of experimental settings and data obtained is included in the Appendix. An increase in drop height and reduction in ignition tip length resulted in a decrease in weld thickness, as shown in Fig. 6. As shown in Fig. 7, it was seen that weld thickness increased with discharge voltage. Drop weight had the least influence on weld thickness, as seen in Fig. 8. Voltage and drop height interacted positively in reducing weld thickness. Ignition tip length and drop height did not show appreciable interaction as observed in Figure 6, but had strong independent effects on weld thickness. Significant higher order interactions were not found.

In order to investigate the effects of different rapid solidification cooling rates on weld metal behavior, different sets of parameters were chosen to produce (1) "slow", (2) "intermediate" and (3) "fast" weld cooling rates. For convenience, this terminology will be used in referring to particular welds hereafter. The corresponding arc times were 1 ms, 0.5 ms and 0.3 ms, respectively. A potential of 90V produced the highest strength for mild steel CD welds in a study by Danks [79]. Hence 90V was used in all three cases. Heat inputs were the same for welds in 6.4 mm diameter and were half that value in 3.2 mm diameter. Designations were chosen combining the material (A, B, C, and D) and welding condition (1, 2, and 3) as described above and are shown in Table 2(a).

In order to explore solidification behavior and process characteristics beyond the above range, additional welds were made with arc times < 0.3 ms and > 1 ms in 304 and 316. Heat input, stud diameter and

arc time were varied to produce different cooling rates. The weld conditions used and their designations are shown in Table 2(b).

B. Microstructure Development in Stainless Steels:

In this section, optical and transmission electron micrographs used to reveal microstructures produced by capacitor discharge welding of 316, 304 and 308 stainless steels are shown.

Optical Metallography:

Optical microscopy of all three stainless steel welds showed a cellular/dendritic structure meeting in a characteristic line at the weld center from the base metal on either side. Growth was found to be fully epitaxial. All the welds produced were observed carefully under different etching conditions and found to be fully austenitic in the fusion zone. Gas tungsten arc welds were made in all three stainless steels (for comparison with CDW) and observed for solidification mode and ferrite contents measured are shown in Table 3. Figure 9 shows microstructures of CD welds A1 to A3 in 316 stainless steel produced under a) slow, b) intermediate and c) fast cooling conditions. The solidification structure of gas tungsten arc deposited 316 weld metal showed about 2-3% ferrite, as in Fig. 10. Close to the base metal, primary austenitic or AF solidification mode was observed, followed by primary ferritic or FA mode growing into the weld. The interdendritic nature of ferrite in AF regions as compared with FA regions was noted, as in Fig. 10. CD welds B1 to B3 in 304 stainless steel showed structures similar to those in 316, as in Figure 11.

The base metal in the 308 alloy contained some residual ferrite as a result of incomplete transformation to austenite after gas tungsten arc deposition and subsequent annealing before CD welding. However, the weld fusion zones in welds C1 to C3 were fully austenitic as seen in Fig. 12(a) to 12(c). In alloy 308, two types of dendrite morphology were observed, namely, primary austenite similar to that in 304 and 316 welds, and a diffuse dendrite structure. In most cases, the diffuse dendritic structure was weaker in etching response than primary austenite and was found to diverge from the ferrite islands touching the fusion zone, as in Fig. 12(b) and (c). These diffuse regions were therefore identified as primary ferrite grown epitaxially from the base metal ferrite regions, subsequently transformed to austenite in the solid state.

Epitaxial growth of primary austenitic regions into primary ferrite in the solid state was obseved in 308 alloy. Slip lines were observed to cross the weld center line from primary austenitic to primary ferritic regions, as seen in Fig. 12(b) and (c). Since slip lines are specific to certain crystallographic directions, it followed that such extended slip lines were only possible by epitaxial growth of primary austenitic grains into the primary ferrite on the other side of the weld center line. No such extensions of slip lines were found in 304 and 316 welds, while slip lines were observed.

Apart from the grain boundary movement as illustrated above, extensive recrystallization was also found in the primary ferrite regions of 308 alloy welds, but not in 316 or 304, which only showed primary austenitic solidification. The grain structure in the fusion zone

in alloy 316 was the same as the as-solidified epitaxial grains, as shown in Fig. 13(a). In 13(b), recrystallization across dendrites and the weld center line is apparent. Thus, it was concluded that the occurrence of recrystallization and atomic rearrangement in alloy 308 was due to a solid state transformation from primary ferrite to austenite.

Transmission Electron Microscopy:

Transmission electron microscopy was done on CD welds in 304 stainless steel and Fig. 14 shows electron micrographs of cells in the weld metal. Figure 14(b) shows that the cells in 14(a) followed a [001] growth direction. Dislocation loops are seen in 14(a), and are seen to be partially aligned along dendrite boundaries in 14(c).

C. Microstructures of FeAl Ordered Alloy:

Welds in FeAl ordered alloy were produced using slow, intermediate and fast cooling conditions D1 to D3. As shown in Fig. 15, CD welds in FeAl also solidified as cells or cellular dendrites. However, the dendrite structure was ill defined and more difficult to reveal by etching than in stainless steel. The GTA weld microstructure in FeAl showed a single phase grain structure but no solidification structure could be revealed eventhough the same metallographic technique as for the CD welds was used. The FeAl base metal was obtained in the powder processed and hot extruded condition, and contained a high inclusion content, which was also observed in the CD weld fusion zone, primarily as intercellular inclusions as shown in Figure 15. FeAl also

exhibited intergranular brittleness and intergranular cracks perpendicular to the weld were found to cross the fusion zone.

Unusual forms of equiaxed dendrite morphology were observed at the weld center in all three welds, as illustrated in Fig. 16(a). To ascertain the nature of these structures, this weld was heat treated at 780°C for 1 hour. The dendrite structure, as seen in 16(b), was unchanged apart from a weaker etching response due to homogenization. A greater number of equiaxed dendrites were found under slower cooling conditions as compared with faster cooling welds. Equiaxed dendrites were also observed in CD welds of centrifugally atomized and hot extruded 304 stainless steel from a previous study and in Figure 17, the equiaxed dendrites are marked by arrows. A high base metal inclusion content was evident in this case also, as revealed by the action of the electrolyte during electropolishing.

D. Heat Flow and Dendrite Growth:

Typical current and voltage profiles obtained during welding are shown in Figure 18, for (a) slow, (b) intermediate, and (c) fast cooling welds. From an examination of these profiles, the sequence of events during welding could be interpreted and this was used in calculating energy distribution during arcing. Arc initiation was marked by a very sharp rise in current flow to reach a peak current of several thousand amperes. The voltage across the capacitors dropped steeply, simultaneously with the current spike at arc initiation. End of arcing was again seen to be marked by a second current peak and voltage drop. Also, in all three sets of curves, the drop in curr-

ent and voltage to zero could be distinguished as different from the end of arcing. Energy discharged after arc extinction was dissipated through a resistor connected into the circuit, after the short circuit due to arc extinction was detected by the welding controls.

The cooling rate during welding increased with shorter arc times and higher heat inputs per unit area. Multiplication of current-voltage curves gave a triangular energy profile from which arc energy was taken as the fraction of the area under the energy curve during arcing. Energy discharged during welding was taken to be equally distributed between the joining surfaces and averaged over the arc time to calculate the arc power density q:

$$q = fCV^2/4at \qquad (20)$$

where C is the capacitance, V the voltage, a the cross sectional area of the weld, t the arc time and f is the fraction of energy discharged through the arc out of the total energy discharged by the capacitor. Primary dendrite arm or cell spacings decreased with increasing power density for stainless steels and FeAl, as shown in Fig. 19. As Figure 20 shows, weld thickness increased parabolically with arc time.
Increase in thickness with time for FeAl was lower than for stainless steels, indicating a lower growth rate under the same welding conditions.

Dendrite arm spacings were measured to estimate cooling rates and also to study dendrite growth during CD welding. Orientation of dendrites with respect to the heat flow direction significantly affected dendrite arm spacings and dendrite or cell morphology. The heat flow direction was taken to be perpendicular to the weld fusion line. Hence,

dendrite arm spacing measurements were made on primary dendrites or cells most nearly parallel to the heat flow direction, and at the weld center line, for estimating cooling rates. Dendrite arm spacings did not show significant variation across the weld section and standard deviations were within 10% of the mean. Dendrite spacings showed a small increase with distance fraction from the weld fusion line towards the weld center line as in Fig. 21, which shows the relationship for 316 stainless steel. The increase in spacing was observed to be greater in the slowest cooling welds. This indicated that average centerline primary dendrite arm or cell spacings were representative of cooling conditions over the entire weld.

Cooling rates calculated from the relationship by N. J. Grant [50], for measured average secondary dendrite arm spacings in all stainless steel CD welds were between 10^6 and 5×10^7 K/s, as shown in Fig. 22. It was also observed that dendrite arm spacings were greater and cooling rates lower in 304 stainless steel than the other two alloys. Secondary dendrite arm spacings were related to primary arm spacings in austenitic stainless steels by a power relation as in Fig. 23. Primary dendrite arm spacings in FeAl were very similar to those in stainless steel, and average values are shown for different arc times in Fig. 24. Average equiaxed dendrite radius increased with arc time and is also shown in Fig. 24.

Dendrite spacings increased with inclination angle to heat flow direction as in Fig. 25. Normalized primary dendrite spacing λ_1/λ_0 was plotted against θ, the orientation angle, where λ_0 is the average primary arm spacing for $\theta = 0$. Side arms could be observed optically

in all but the fastest cooling welds, and tendency for side arm growth increased with angle of inclination to heat flow direction. In some dendrites oriented at $\theta = 45°$, secondary arms grew into primary dendrites as in Fig. 26(a) and (b). No dendrites were found to be inclined at more than 45° to the heat flow direction. Growth parallel to heat flow tended to be cellular while growth at angles close to 45° tended to be fully dendritic.

E. Arc Behavior During CDW:

In this section, data generated during welding of stainless steel and FeAl were combined to examine arc characteristics during the CD process. By weighing the components before and after joining, the amount of material lost as 'spattered' melt and to vaporization was calculated. The amount of metal present in the weld was found from the average weld thickness. The total amount of metal melted was 4 to 5 times that in the weld, as shown in Fig. 27. Additional data for arc times beyond the range in Fig. 27 were included in Figure 28, and a sharp decrease in the amount of metal melted was seen with decreasing arc time. FeAl showed melting characteristics similar to stainless steel. Assuming that most of the transferred energy from the arc was used for melting, and neglecting vaporization, arc efficiency was calculated :

$$\text{Arc Efficiency} = \frac{\text{Energy used for melting}}{\text{Available arc energy}} \qquad (21)$$

To calculate energy used for melting, the melt was assumed to be super-heated linearly to the vaporization temperature from the melting point.

Arc efficiency decreased with increasing power density, as in Fig. 29. The welding arc was initiated at the center of the stud by the ignition tip and propagated to occupy the entire stud area. High speed video-graphs of CDW were available from a study by Danks [79], from which lateral arc expansion could be studied. Radial arc propagation occurred faster with increased voltage as shown in Fig. 30. Average arc velocity was calculated from Fig. 30 and was seen to increase with voltage in Fig. 31. Drop head velocity shown for comparison, was several times less than lateral arc velocity.

Although energy output during arcing should decrease exponentially, at least 90% of the energy in the capacitors is found to be discharged when the current first reaches zero, due to inductance and resistance in the circuit. The time from the start of arcing to this point was taken as the discharge time. Discharge time increased with capacitance and decreased with voltage as in Fig. 32. Measured arc times were plotted against calculated values assuming the velocity of the drop head to be affected by gravity alone:

$$\text{Arc time} = \frac{\text{Ignition Tip Length}}{(\ 2 \times g \times \text{Drop Height})^{1/2}} \tag{22}$$

Good agreement as in Fig. 33 showed arc time to be a simple kinematic function of stud drop height and ignition tip length and can be accurately controlled during CDW.

V. DISCUSSION

A. Solidification in Austenitic Stainless Steels:

In order to determine solidification modes occurring in stainless steels, it is necessary to correct for the presence of elements other than Cr and Ni in Fe, so that the positions of specific alloys are fixed in the Fe-Cr-Ni phase diagram. Good correlation in recent studies between predicted and observed microstructures has been found [11,80] for stainless steels using the Cr and Ni equivalents first proposed by Hammar and Svensson [12]. Using the above equivalents, we find that in Fig.34, 316, 304 and 308 alloys lie on the AF, FA and FA-F regimes of the phase diagram respectively. Table 3 gives the Cr and Ni equivalents by the DeLong and Hammar-Svensson methods, and predicted ferrite contents in GTAW. The DeLong diagram predicted retained ferrite content closely, while the Hammar-Svensson method showed better agreement with solidification mode. It can be seen that alloy 316 is very close to the eutectic point, estimated to be at a Cr Eq./Ni Eq. ratio of 1.5 by the latter method.

Figures 9 and 11 show that 316 and 304 alloy CD welds solidified as fully austenite at cooling rates in excess of 10^6 K/s. The following table gives the stable equilibrium and observed solidification sequences seen in the three alloys:

Alloy	Equilibrium Sequence	Observed During CD
316	L -> L + γ + δ -> γ + δ -> γ	L -> L + γ -> γ
304	L -> L + δ -> L + δ + γ -> δ + γ -> γ	L -> L + γ -> γ
308	L -> L + δ -> L + δ + γ -> δ + γ -> γ	L -> L + δ + γ -> δ + γ -> γ

For the GTAW in alloy 316, primary austenite solidified close to the base metal, whereas primary ferrite formed subsequently. Ferrite content close to the base metal was significantly lower than that in the primary ferritic portion of the microstructure. It was also observed that some austenite had transformed to ferrite at the heat affected zone grain boundaries in the GTAW during heating and was retained as ferrite after cooling. Hence it appears that the formation of primary austenite at the expense of ferrite in both CD and GTA welds was due to difficulty in nucleating ferrite, resulting in a metastable extension of the austenite field. This would also be favored by epitaxial growth on the austenitic base metal. Suppression of primary ferrite nucleation has also been reported earlier in laser and CD welding of 304 stainless steel [4,15]. The diffusional transformation between austenite and ferrite during heating and cooling is slow under high heating and cooling rates. Consequently, increasing solidification velocity would decrease primary ferrite, and residual ferrite at room temperature.

Thermal phase stability curves are available for the formation of either bcc or fcc phase from the liquid, for an austenitic stainless steel with alloy content of 30% and Cr_{eq}/Ni_{eq} ratio of 1.68 [57]. Since this composition range was very close to those used in this study, these curves were applied to alloys 316 and 304 to estimate the conditions of formation of fcc austenite from the liquid. Formation of austenite from the melt is possible at or below 1365°C, as shown in Fig. 35. The melting points of the 316 and 304 alloys were calculated to be 1410 and 1425°C from relationships available in literature [81].

Although ternary eutectic or peritectic solidification involves three phase interaction, the high values of partition coefficient for Cr (0.83) and Ni (0.95) allowed a reasonable estimate of undercooling required to form austenite as > 50°C. This value is 8 to 10 times greater than that for stable equilibrium solidification for which T is 4-6°C [60].

In the case of 308 alloy, primary ferrite was nucleated by ferrite in the base metal in contact with the fusion zone, as in Fig. 12(b). It is interesting to note that under CD welding conditions, primary ferrite and austenite have grown together seemingly independent of each other. Spreading out of the primary ferritic regions and selective growth of austenite grains with growth directions most nearly parallel to heat flow suggest that primary ferrite grows at a faster rate than austenite. In Fig. 13(b), triangular regions of primary austenite can be seen to be pinched off by faster growing primary ferrite. Faster growth of ferrite is consistent with the lower packing fraction and density of the bcc lattice as compared with fcc, if interface kinetic effects are considered to be the same.

B. Solid State Transformations:

Diffusion in the solid state will be considered in discussing solid state transformations in stainless steel. Rates of diffusion of Cr and Ni in the bcc lattice are found to be two orders of magnitude greater than in fcc. Table 4 gives diffusion coefficients along the significant temperature interval during cooling of welds in austenitic stainless steels under study. Average diffusion distances have also

been shown for times characteristic of CD welding. Figure 36 gives cooling curves from a unidirectional finite element heat flow model for CD welding of stainless steel calculated by Einerson et al. [82]. The weld in this case was made under similar conditions to those used in the present study. From Fig.36, available diffusion times for transformations during the weld cycle can be determined.

Primary ferritic regions as in Figs.12 and 13(b) appeared to have a diffuse dendritic structure when compared with primary austenite. The weaker etching response is likely to result from greater diffusional homogenization in the solid state for primary ferrite, due to higher diffusion rates (Table 4).

The most striking feature of the welds in 308 alloy is the recrystallization across as solidified grain boundaries in primary ferrite, as in Fig.12(b). Since such recrystallization was not observed in 316 and 304 alloys, it must be concluded that it is the result of transformation of the primary ferrite to austenite in 308. Also, epitaxial grain growth of primary austenite into primary ferritic regions is seen in Fig.12(b). Such movement of the transformation interface across the parent phase grain boundaries is believed to be unique to the 'massive' type transformation [83]. The occurrence of this transformation has been a much debated aspect of stainless steel metallurgy since Lippold and Savage [84] first proposed the massive type reaction to account for primary ferrite transformation to austenite. We shall now examine the conditions favorable for the massive reaction to occur during CD welding.

The expanding austenite solvus region in Figure 34 extends below the primary ferrite side of the eutectic trough in the phase diagram, requiring that such ferrite can transform to austenite upon cooling by either:

(i) a full diffusional transformation in the austenite-
ferrite region, or,

(ii) a composition invariant transformation in the austenite
region if the reaction is not allowed to proceed as in (i).

It is recognized that most reaction products during continuous cooling result from competing reaction mechanisms and that kinetics determine the preponderance of any of them [83,85]. Well known examples of such situations occur in various steels, Fe-Ni, and Cu-Zn systems. These situations are also regarded as solid state analogs of transformations occurring during solidification. The massive transformation is analogous to partitionless solidification which has even been referred to as 'massive' [83]. Nucleation of the product phase is the rate controlling step in the massive transformation, and growth rates can be as high as several cm/s [83]. In the present case, massive growth could take place epitaxially at a high rate.

A full diffusional transformation from primary ferrite to austenite would occur at high cooling rates by growth of acicular or Widmanstatten type austenite platelets into the ferrite and may not go to completion. Such growth has been found in 308 alloy solidified at 10^3 K/s by Lippold and Savage [Figure 10 in ref. 84]. Cooling rates during CD welding exceeded 10^6 K/s and no retained ferrite was found in any of the CD welds in the present study. Hence it is clear that the transformation

of primary ferrite to austenite in 308 stainless steel during capacitor discharge welding is due to a massive transformation.

On the basis of the discussions in sections (i) and (ii), and considering the work of Devletian and Wood [15], it can be seen that the presence of retained primary ferrite in stainless steel welds is a composite of reactions controlled by kinetics during solidification as well as solid state transformation. The following statements can be made with respect to compositions in the austenite field at room temperature and solidifying with ferrite as one of the primary phases:

(1) At very slow cooling rates, primary ferrite transforms completely to austenite upon cooling.

(2) At cooling rates typical of gas tungsten arc welding (10 to 10^2 K/s), the amount of retained ferrite increases with cooling rate due to incomplete diffusional transformation from primary ferrite to austenite.

(3) At higher cooling rates (10^2 to 10^7 K/s), retained ferrite decreases rapidly due to suppression of primary ferrite nucleation and increasing driving force for massive transformation of the ferrite.

(4) Above 10^6 K/s, primary ferrite formed during welding transforms to austenite predominantly by a massive reaction.

The fully austenitic structure produced by CD welding in place of the duplex austenitic-ferritic structure after conventional welding can result in superior corrosion resistance and reliability of welds in service. At high cooling rates, the fine scale of segregation avoids hot cracking even under fully austenitic solidification conditions.

The occurrence of microstructural modification in austenitic steel is therefore of engineering interest in view of applications in joining rapidly solidified stainless steel and other RSP materials.

C. Transmission Electron Microscopy:

Transmission electron microscopy reveals several interesting features in capacitor discharge welds in stainless steel. Figures 14(a) and (b) show that dendrites in austenitic steel followed a [001] growth direction. Defect structures produced by rapid solidification are shown in Figures 14(a) and (c). Vacancy dislocation loops were seen decorating the dendrite boundaries which also contained a high density of free dislocations. No second phase was visible in the TEM, confirming optical microscopy. Dislocation loops were previously observed by Wood and Honeycombe [58] in splat quenched asutenitic steel, and were attributed to rapid growth rates of several cm/s observed during splat quenching. The density of dislocations and vacancy dislocation loops have been shown to be proportional to reciprocal cooling rate in liquid quenched stainless steel [59]. Excess vacancy concentrations are formed by trapping of vacancies at fast crystal growth rates and high temperatures. These excess vacancies are believed to nucleate and condense to form vacancy dislocation loops and raise the bulk dislocation density. The annihilation of excess vacancies depends on the relaxation time allowed during cooling and is therefore responsible for the reciprocal relationship between dislocation density and cooling rate [59].

D. Solidification in FeAl Ordered Alloy:

The composition of the Fe - 40 at% Al ordered alloy used in the present study falls on the single phase solidification region in the iron rich side of the Fe-Al phase diagram in Fig.37. The composition is seen to be within the B2 field in the solid state. It was observed that FeAl solidified during CDW as a single phase material as in Fig. 15. No recrystallization in the weld was found in the fusion zone. From Fig.37, it can be seen that the solidification range of about 33°C is relatively small and the measured value of k is 0.88, which results in reduced segregation. The weak etching response observed in FeAl (Fig.15) CDW is consistent with these effects. The absence of a dendritic structure in the GTA weld metal is possible either by planar solidification or by diffusional homogenization in the solid state. The solidification range of 33°C for FeAl is significant enough to cause dendritic growth under GTAW conditions and solid state diffusion may be more likely to eliminate segregation.

The CD welds in FeAl contained equiaxed dendrites at the weld center (Fig.16(a)). These dendrites exhibited an unusual shape in that the maltese cross of the conventional equiaxed dendrite was rarely observed. Instead, irregular branching from the center of the dendrites seeemed to occur. The heat treatment of 1 hour at 780°C was done in order to distinguish the equiaxed dendrite growth from solid state transformations structures or metastable phases. No qualitative change in the microstructure was seen as in Figure 16(b), except that segregation was reduced. Equiaxed dendrites were not observed in any

of the welds in stainless steel in the present study. The base metal in FeAl contained a large concentration of inclusions decorating prior particle boundaries as a result of hot extrusion. Such high inclusion concentrations were not present in the stainless steels. While studying the origin of the equiaxed dendrites as shown in 16(a), it was observed that similar dendrites were also present in CD welds made in centrifugally atomized and hot extruded 304 stainless steel under similar conditions as those used in the present study. Figure 17 shows that a high concentration of inclusions exists in the base metal in this case also. Hence the high inclusion concentration can be correlated with formation of equiaxed dendrites both in FeAl and powder processed stainless steel. Since the materials were centrifugally atomised to form powder, oxidation of the surfaces during cooling is likely to have resulted in oxide inclusions in the wrought material. While the probable role of inclusions is that of nucleating sites for equiaxed dendrites, the exact nature of the nucleating agents must be revealed by future work, using, for example analytical electron microscopy. The heat flow and solidification conditions favoring equiaxed dendrite growth will be discussed in a subsequent section.

E. Melting and Solidification Behavior:

Comparison With Laser Melting:

Several similarities were observed between laser and capacitor discharge processes in terms of melting and solidification phenomena. An examination of Figure 18 shows that for arc times 0.5 ms and 0.29 ms, arc current was still high at the end of arcing, whereas for 1

ms, current is nearly zero. Multiplication of the current and voltage curves gave a trapezoidal energy pulse. The current and voltage profiles were compared with those obtained by Von Botisk et al. [88] for capacitor discharge welding of 5 mm diameter stainless steel, using 75 mF at 75 V. The curves obtained in the present study were very similar in shape and magnitude to those in ref. 88 and were therefore used in further analysis. In laser melting by a rectangular pulse, melting continues for a short time after the energy input has stopped [73,74]. A similar sequence of melting and resolidification was expected for CD welding, though the approximation becomes less accurate for triangular pulses when arc times are comparable to or greater than the discharge time.

Interdendritic spacing, as a measure of cooling rate, decreased with power density (Figure 19), indicating that increasing arc power density increased cooling rate in stainless steels and FeAl. A similar relation has been shown for absorbed power density by numerical modelling of laser melting [73,74]. However, cooling rates in the CD process asymptotically approached a constant value for arc power densities greater than $10^6 W/cm^2$. This indicated that average arc power density differed appreciably from the actual absorbed value. Its significance will be discussed in a later section.

In the CD process, resolidification was stopped midway when the components touched each other and the remaining liquid was expelled. Figure 21 shows that primary dendrite spacing, and therefore cooling rate, remained fairly constant with fractional distance from the fusion line to the weld center. Growth rates and cooling rates calculated

by Hsu, Chakravorty, and Meharabian [73] for unidirectional heat flow conditions in laser surface melting showed a similar trend for resolidified distances upto half the melt depth in pure Fe and Ni. However, in order to use their calculations, it was essential that absorbed power density and fractional distances solidified be accurately known. Since dendrite arm spacings were accurately measurable, they were considered more reliable for cooling rate measurements.

Secondary dendritic spacing values in the present study gave cooling rates between 10^6 and 5×10^7 K/s (Fig.22) by extrapolation of N. J. Grant's relationship [50]. Secondary dendritic spacings in 304 were larger than those of 308 and 316. From the table of alloy compositions it is seen that alloys 308 and 316 contained about 5% more alloying additions than 304. This variation could result in greater thermal diffusivity in 304 and hence lower cooling rates than the other two alloys under the same welding conditions.

Primary dendritic spacings have also been related to cooling rates in stainless steels. The relationship between primary arm spacings and cooling rate by Okamoto [60] is of the form:

$$\lambda_1 \propto (\Delta T_0)^{1/6}(GR)^{-1/2} \qquad (23)$$

where λ_1 is in μm and ΔT_0 is the solidification range. This relation has been found to fit primary dendrite arm spacing data at cooling rates close to 1 K/s in ingots and castings. Extrapolating this relation, we find that cooling rates predicted for CDW are two orders of magnitude lower than that by Grant. However, as shown in Fig.38, the exponent of $-1/2$ on GR was seen to fit actual dendrite spacings when calculated cooling rates from Fig.22 were used. This relation has a

more negative dependence on R than those of Hunt [53] and Kurz and Fisher [32], which is of the form $\lambda_1 \propto G^{-1/2}R^{-1/4}$. This is consistent with the relative insensitivity of primary dendritic spacings to growth rate changes than secondary dendritic spacings [54]. Thus, it is concluded that the cooling rate dependencies of primary and secondary dendrite arm spacings are consistent with each other using empirical relationships from the literature for stainless steel. No such relationships are yet reported for FeAl.

Primary versus Secondary Dendritic Spacing:

Since primary as well as secondary dendrite arm spacings were related to cooling rate, it was expected that they be related to each other. Figure 23 shows that the relationship in austenitic stainless steel was of the form $\lambda_2 \propto \lambda_1^{0.39}$ under rapid solidification conditions. Eventhough secondary dendrite arm spacings have previously been shown to be affected by coarsening, measurements in CD welds indicated that there was no appreciable change in spacing at different distances along primary dendrite arms. However, the scatter in the spacing data could be partly attributed to coarsening of secondary dendrite arms.

Primary and secondary arm spacings approached each other in value close to $0.27 \mu m$ upon extrapolation of the line in Fig. 23. The relative magnitudes of primary and secondary dendritic spacings indicate that the solidification regime would be close to the dendritic-cellular transition, where a sharp increase in dendrite tip radius would occur, along with the disappearance of side arms. This situation is analogus to the cellular to dendritic transition at low velocities.

Growth Rate and Stability:

Average weld thickness data related linearly to square root of arc time in stainless steels and FeAl (Fig. 20). In observing the weight of molten metal versus arc time in Fig. 27, and power density versus spacing data in Fig. 19, melting conditions in FeAl were very similar to that in stainless steel. The lower thickness of FeAl for similar arc times as stainless steel could therefore be ascribed to a lower growth rate though actual melting and solidification times were not known.

The ordering temperature of the B2 lattice in FeAl is reported to be above the melting point [61]. However, the composition in the present case was Fe-40 at% Al, and the phase diagram has not been determined with certainty in that region. If the ordering reaction occured during solidification, ordering kinetics at the liquid-solid interface could account for the lower growth rate as compared to stainless steel.

Estimates of average growth rates for stainless steel were done using laser melting data for pure Fe and Ni, and values obtained for welds in 316 stainless steel corresponding to conditions A1, A3 and A5 are shown in Table 5. Since secondary dendrite arm spacings were known, dendrite tip radii were also known by Trivedi's relationship $\rho = \lambda_2/2$ [33]. The Peclet number, which is the ratio of tip radius to solute diffusion distance was then calculated, and is also shown in Table 5. Average growth rates were between 9.3 and 33.4 cm/s for welds in 316 and were expected to be close to those values in the other stainless steels also. Peclet numbers were between 16.4 and 46, and these high values indicate that solidification was close to absolute

stability. The relative increase in secondary dendrite spacing and hence tip radius with respect to primary spacing should also occur close to the dendritic-cellular transition prior to absolute stability, as discussed in the previous section.

Direct calculation of the Peclet number versus growth rate curve in the case of stainless steel was difficult due to uncertainty in determining the undercooling during solidification, and to account for the partitioning of Cr and Ni during growth. In the case of FeAl, no metastable phase relationship was expected and the solidification range was calculated from the equilibrium phase diagram. The Peclet number versus growth rate curve could then be calculated, and is shown in Fig.39. The values of materials constants used for stainless steels and FeAl are shown in Table 6. The liquid-solid interfacial energy for FeAl was assumed to be that of iron [89] and density was measured to be 6.13 g/cm^3. An approximate diffusion coefficient was assumed for diffusion of Al in liquid iron as 3×10^{-5} cm^2/s. The Gibbs-Thompson parameter was calculated from these values. Absolute stability occurs at a growth rate of 64.4 cm/s. Average growth rates for FeAl were estimated from those of stainless steel, applying a growth rate ratio estimated from thickness and arc time data, and were between 4.8 and 11 cm/s in welds D1 to D3. From growth rates the Peclet numbers were estimated to be between 1 and 2, as seen in Fig.39.

Crystallographic Orientation and Growth:

At high growth rates, dendrites in cubic materials have been shown to grow preferentially along <100> directions due to the low packing density along that direction compared with other crystallographic direc-

tions [85,86]. In the present work, transmission electron microscopy (Fig.14) showed that dendrites in stainless steel followed a <100> direction. Increasing the welding speed in GTAW has been shown to increase the <100> texture in similar alloys, at the expense of other orientations like <110>. Under rapid solidification conditions as in CDW, it can be expected that dendrite orientations other than <100> are competively eliminated. This is supported by the observation that dendrites were not found inclined at more than 45° to the weld axis, and also that development of side arms took place at 90° to the primary dendrites. As in Fig. 25 it was seen that primary dendrite spacing increased with dendrite inclination angle to the weld fusion line. Considering the directionality of the heat flow vector in unidirectional solidification, dendrites growing at an angle to heat flow solidified under different thermal gradient and cooling rate conditions compared with those parallel to heat flow. Since primary dendrite spacings have been shown to be highly gradient dependent [33,54], it was expected that inclination angle bears a power relation with dendrite arm spacing. Inclination angle versus spacing data are shown against $\cos\theta$ on a logarithmic scale in Fig. 40 and the linearity of the relation is evident. However the slope of -1.66 showed that the dependence is not explainable by the effect of inclination angle on thermal gradient alone, and it is concluded that both gradient and growth rate were affected by changes in orientation angle.

An interesting example of side arm growth into dendrites occurred in Fig. 26 in which three to four branchings at 90° to each other have grown from a single dendrite at 45° to the heat flow. Similar 90°

changes in growth direction have been previously reported in stainless steel GTAW [86].

Variation of G/R During CD Welding:

During CD welding, growth rate increased from zero at the weld fusion line to very high values. The low R region close to the fusion line was therefore planar due to high G/R and was seen in all the weld microstructures. As solidification proceeds towards the surface of the melt, G should decrease while R remains high. Since G/R then decreases, a more dendritic structure should result. For melt depth fractions found in CD welding, G/R conditions remained fairly constant [73]. However, the Slow cooling condition 1 produced more dendritic structures than the faster cooling conditions 2 and 3, indicating progressively higher G/R for the latter.

As discussed in the previous section, greater tendency for side arm development was shown by dendrites inclined at an angle to heat flow direction, as seen in Fig.26. A lower component of G along the direction of inclination would lower G/R under similar growth conditions with respect to dendrites parallel to heat flow, causing a more dendritic structure. However, it was also observed that side arm growth on dendrites parallel to heat flow would be affected by:

(a) absence of thermal supercooling along the secondary arm growth direction, i.e., perpendicular to heat flow, and

(b) the kinetic limitation imposed by closely spaced primary dendrite arms.

Secondary dendrite arms on dendrites parallel to heat flow are initiated due to instability at the dendrite tip. Subsequent growth

perpendicular to heat flow would be due undercooling provided by solute rejection, under negligible thermal undercooling. Close spacing of rapidly growing primary dendrites would also tend to suppress side arm growth. On the other hand, a substantial component of thermal undercooling along with free liquid ahead of the growth front may be present for growth of side arms from inclined dendrites as shown in Fig. 26.

As the liquid pools contact during CD welding, rapid heat extraction should take place to both sides of the weld after arc extinction. At this point, the thermal gradient could have very low values at the center plane of the liquid pool, and the high heat extraction rates can lower G/R appreciably. In conventional casting processes, equiaxed dendrites form under such conditions when nuclei are present [21]. Equiaxed dendrites are known to occur by heterogeneous nucleation, dendrite arm remelting due to convection, due to constitutional supercooling and due to thermal supercooling, as some possible mechanisms [90,91]. None of the conventionally processed materials showed equiaxed dendrites in CD welds. During growth of tight packets of cellular dendrites, dendrite arm remelting mechanisms are unlikely. Hence it is concluded that equiaxed dendrites in FeAl and powder processed stainless steel were heterogeneously nucleated by oxide inclusions present in the base metal.

The coarseness of the dendrite spacing inside the equiaxed dendritic structures in Figure 16(a) showed that cooling rates were much lower than in the cellular dendritic zone. Nucleation of equiaxed dendrites could occur early at the start of weld pool solidification

allowing them to grow 3 to 6 μm in size (Fig. 24) eventhough the equi-
axed growth rates may be lower than the average.

F. Arc Efficiency and Behavior:

Arc Efficiency:

It was evident from Figures 27 and 28 that 4 to 5 times as much
melting took place during capacitor discharge welding as was retained
in the weld. Also, the amount of melt decreased with time for the
same heat input. Amount of molten metal was calculated from the weld
volume and spatter was measured as weight loss of the components during
welding. From this mass balance, the energy absorbed by the melt was
calculated using the following three assumptions:

(i) Melting efficiency was assumed to be close to 100%, since
it is known that efficiencies during laser melting for comparable power
densities are very high [71].

(ii) Under similar power densities, the surface of the melt
reaches the vaporization temperature in pure Fe, Ni and Al in 10^{-5}
to 10^{-7} seconds. Also, numerical calculations show a nearly linear
temperature profile between melting and vaporization fronts. Therefore,
an average superheat of one half the value between the melting and
vaporization temperatures was assumed.

(iii) The amount of energy absorbed by latent heat of vaporization
was neglected.

The calculated value of absorbed energy was expressed as a percentage
of the arc energy calculated from current-voltage profiles. Figure

29 shows arc efficiency to asymptotically approach a constant value for power densities above 10^7 W/cm^2.

Arc efficiencies have been found to decrease linearly with power input during GTAW [92]. For comparison, values obtained for CD welding are shown together with data from ref. 92 in Fig. 41. The GTAW efficiencies were calculated as the percentage of the total power absorbed in heating the work, or the anode. In Figure 41, the downward trends are consistent between the two sets of data for increasing power. However, extrapolations of either set of points do not match. Arc efficiencies for 6.4 mm diameter welds were not consistent with each other with power input. On the other hand, the dependency of efficiency on power density in Fig. 29 is clear. Hence, it is postulated that power density has a more fundamental effect on arc efficiency than power alone and is therefore a more appropriate factor in relating to efficiency of a high power arc.

Radiated energy from GTAW arcs has been shown to increase with arc current [92]. Since arc temperature increases with current, the fourth power dependency of radiation losses with temperature should account for decreased efficiency with increasing current, and therefore, power density.

Arc Propagation and Discharge Time:

Lateral arc propagation occurred rapidly with higher voltages during CDW as seen in Figures 30 and 31. Faster arc spread could occur at higher voltages because of greater radial arc force due to increased arc current density. Lateral arc expansion time became comparable with arc time for large diameter welds and relatively lower voltages and

would therefore be a consideration in extending the capabilities of CDW in applicability to diameters larger than 13 mm.

Arc times measured from current-voltage profiles showed that it is easily controlled during CDW. Arc time was varied by changing the stud drop height and ignition tip length, as discussed in the parametric study. Discharge current from a capacitor decreases exponentially by the relation:

$$i = i_0 e^{-t/RC} \tag{24}$$

where i is the current at time t, i_0 the initial current, R the resistance of the circuit and C is the capacitance. Discharge time is therefore increased when either the circuit resistance and inductance are increased, or if the capacitance is increased. From Fig.33, it is also evident that increasing voltage decreases discharge time. Therefore, if shorter discharge and arc times are required, lower capacitances are to be used. Decrease in discharge time will result in higher power density for the same heat input and becomes important for attaining higher cooling rates.

G. Future Work:

From a study of arc characteristics, two potential areas for future work are identified, namely, joining larger diameters and achievement of higher cooling rates in CDW.

1. Higher cooling rates during CDW could be achieved by decreasing arc times using smaller ignition tips and capacitances, along with smaller stud diameters.

2. In joining large diameters while still maintaining rapid solidification conditions, lateral arc propagation is likely to be a limiting factor. To solve this problem, it might be necessary to use multiple ignition tips, and different ignition tip geometries.

In increasing power density to attain high cooling rates, heat transfer efficiency from the arc to the work might be a limitation, as revealed from the present study. It is known from surface melting work that the price of higher cooling rates during laser processing is increasingly smaller melt depths and other dimensions [23].

Despite the few limitations foreseen, the capacitor discharge process remains the only welding process capable of rapid solidification joining. It is also the only arc process that has so far been used for RSP applications. Therefore, it claims the distinction of being the potentially most useful process for joining RSP materials, composites, and other materials traditionally difficult to join. Since a relatively large joint can be produced under unidirectional cooling, it is ideally suited for the study of rapid solidification phenomena.

VI. CONCLUSIONS

Rapid solidification by capacitor discharge welding of stainless steels and FeAl ordered alloy was investigated and the following can concluded:

1. Under capacitor discharge welding conditions, for cooling rates exceeding 10^6K/s, 316 and 304 grade stainless steels solidified completely as austenite by rapid epitaxial growth of the austenitic substrate and suppression of ferrite nucleation.

2. At cooling rates exceeding 10^6K/s, 308 stainless steel solidified partly as austenite and as ferrite. The primary ferrite transformed completely to austenite in the solid state during cooling by a massive transformation.

3. Solidification during capcitor discharge welding exhibited unidirectional heat flow under rapid solidification conditions.

4. Dendrite arm spacings increased with angle of inclination to heat flow direction and the tendency to form more dendritic structures increased as the angle of inclination approached 45°. No dendrites were ever observed to grow at more than 45° to the heat flow direction.

5. Capacitor discharge welds in stainless steel exhibited cellular dendritic growth. Growth rates at cooling rates between 10^6K/s and 5×10^7 K/s were between 9.3 and 33.4 cm/s.

6. Primary and secondary dendrite arm spacings approached each other in value at a cooling rate close to 6×10^7 K/s and growth rate above 33.4 cm/s. This point was found to be close to the dendritic to cellular transition.

7. FeAl ordered alloy showed single phase solidification. No metastable phases were observed at estimated cooling rates of 10^5 to 10^6 K/s.

8. Equiaxed dendrites were found in FeAl capacitor discharge welds apart from cellular dendritic solidification. They were found to be nucleated by oxide inclusions present in the material due to prior powder processing.

9. Heat transfer efficiency from the welding arc decreased as arc power density was increased during capacitor discharge welding. For a high power arc, arc efficiency was better related to power density than total power input.

10. Decreasing capacitance, arc time and weld diameter and increasing the arc voltage were found to promote high cooling rates by increasing the arc power density.

VII. BIBLIOGRAPHY

1. P. Duwez, Trans. ASM, 1967, vol.60, p607.

2. J. S. Langer, Metall. Trans. A, 1984, vol 15, pp. 977-82.

3. W. Kurz, B. Giovanola, R. Trivedi, Acta metall., 1986, vol. 34, pp. 823-830.

4. J. M. Vitek, A. Dasgupta, S. A. David, Metall. Trans. A, vol. 14, pp. 1833-41.

5. S. Katayama, T. Fujimoto, A. Matsunawa, Trans. JWRI, 1985, vol. 14, pp. 123-38.

6. D. B. Moharil, I. Jin, G. R. Purdy, Metall. Trans. A, 1974, vol. 5, pp. 59-63.

7. C. Lyman, Weld. J., vol. 60, pp. 189s-94s.

8. O. J. Periera, J. Beech, in "Solidification Technology in the Foundry and Cast House", Metals Society, London, 1983, p315.

9. N. Suutala, T. Takalo, T. Moisio, Metall. Trans. A, 1980, vol. 11, pp. 717-25.

10. W. T. DeLong, Weld. J., 1974, vol. 53, pp. 273s-86s.

11. N. Suutala, Metall. Trans. A, 1983, vol. 14, pp. 191-97.

12. O. Hammar, U. Svensson, in "Solidification and Casting of Metals"- The Metals Society, London, 1979, p401.

13. N. S. Stoloff, Int. Met. Rev., 1984, vol. 29, p123.

14. D. Hardwick, G. Wallwork, Rev. High Temp. Mater., 1978, vol. 4, pp. 47-74.

15. J. H. Devletian, W. E. Wood, paper presented at the 66th Annual AWS Convention, Las Vegas, 1985.

16. J. W. Rutter, B. Chalmers, Can. J. Physics, 1953, vol. 31, pp. 15.

17. W. A. Tiller, K. A. Jackson, J. W. Rutter, B. Chalmers, Acta metall., 1953, vol.1, 428-37.

18. W. W. Mullins, R. F. Sekerka, J. Appl. Physics, 1964, vol. 35, pp. 444-51.

19. R. Trivedi, Acta metall., 1970, vol. 18, pp. 287-96.

20. J. S. Langer, H. Muller-Krumbhaar, Acta metall., 1978, vol. 26, pp. 1681-87.

21. M. C. Flemings, "Solidification Processing", McGraw-Hill, New York, 1974.

22. M. Cohen, R. Mehrabian, in "Rapid Solidification Processing, Principles and Technologies III", edited by R. Mehrabian, National Bureau of Standards, Washington DC, 1983, p1.

23. R. Mehrabian, Int. Met. Rev., 1982, vol. 27, pp. 185-208.

24. J. H. Devletian, S. Venkataraman, S. Chen, paper presented at the 67th Annual AWS Convention, Atlanta, 1986.

25. J. C. Baker, J. W. Cahn, in "Solidification", ASM, Metals Park, 1971, p23.

26. R. Trivedi, J. Crystal Growth, 1980, vol. 49, pp. 219-32.

27. G. P. Ivantsov, Akad. Nauk. SSSR. Doklady, 1947, vol. 58, pp. 567-9.

28. G. Horway, J. W. Cahn, Acta metall., 1961, vol. 9, pp. 695-705.

29. M. H. Burden, J. D. Hunt, J. Crystal Growth, 1974, vol. 22, Part I: pp. 99-108, Part II: pp. 109-116.

30. I. Jin, G. R. Purdy, J. Crystal Growth, 1974, vol. 23, pp. 37-44.

31. M. E. Glicksman, R. J. Schaefer, J. D. Ayers, Metall. Trans. A, vol. 7, pp. 1747-59.

32. W. Kurz, D. J. Fisher, Acta metall., 1981, vol. 29, pp. 11-20.

33. R. Trivedi, K. Somboomsuk, Mat. Sci. Eng., 1984, vol. 65, pp. 65-74.

34. S. R. Coriell, R. F. Sekerka, in Proc. II Int. Conf. on Rapid Solidification Processing, edited by R. Mehrabian, B. H. Kear, M. Cohen, Claitor's Pub. Div., Baton Rouge, 1980, pp. 35-49.

35. W. J. Boettinger, S. R. Coriell, R. F. Sekerka, ref. 22, pp. 45-55.

36. J. H. Perepezko, W. J. Boettinger, ref. 22, pp. 223-40.

37. W. J. Boettinger, D. Shechtman, R. J. Schaefer, F. S. Biancaniello, Metall. Trans. A, 1984, vol. 15, pp. 55-66.

38. J. W. Cahn, S. R. Coriell, W. J. Boettinger, in "Laser and Electron Beam Processing of Materials", Academic Press, New York, 1980, pp. 89-103.

39. M. J. Aziz, J. Appl. Phys., vol. 53, pp. 1158-68.

40. K. A. Jackson, G. H. Gilmer, H. J. Leamy, in "Laser and Electron Beam Processing of Materials", Academic Press, New York, 1980, p104.

41. S. R. Coriell, R. F. Sekerka, J. Crystal Growth, 1983, vol. 61, pp. 499-508.

42. S. C. Huang, M. E. Glicksman, Acta metall., 1981, vol. 29, Part I: pp. 701-15, Part II: pp. 717-34.

43. M. Abramowitz, I. A. Stegun, editors, "Handbook of Mathematical Functions", Dover, New York, 1968.

44. K. Somboonsuk, J. T. Mason, R. Trivedi, Metall. Trans. A, 1984, vol. 15, p967.

45. H. Matyja, B. C. Giessen, N. J. Grant, J. Inst. Met., 1968, vol. 96, pp. 30-32.

46. T. Okamoto, K. Kishitake, J. Crystal Growth, 1975, vol. 29, pp. 137-46.

47. M. A. Taha, Metal Science, 1979, vol. 13, pp. 9-12.

48. C. M. Claren, J. D. Verhoeven, R. Trivedi, Metall. Trans. A, 1980, vol. 11, pp. 1853-61.

49. J. T. Mason, J. D. Verhoeven, R. Trivedi, J. Crystal Growth, 1982, vol. 59, pp. 516-24.

50. N. J. Grant, in "Industrial Materials Science and Engineering", edited by L. E. Murr, Marcel Dekker, 1984, p243.

51. P. N. Quested, M. McLean, Mat. Sci. Eng., 1984, vol. 65, pp. 171-80.

52. R. M. Sharp, A. Hellawell, J. Crystal Growth, 1971, vol. 11, p77.

53. J. D. Hunt, in "Solidification and Casting of Metals", Metals Society, London, 1979, p1.

54. R. Trivedi, Metall. Trans. A, 1984, vol. 15, pp. 977-82.

55. V. G. Rivlin, G. V. Raynor, Int. Met. Rev., 1980, vol. 26, pp. 21-38.

56. R. M. Boothby, Mat. Sci. Tech., 1986, vol. 2, pp. 78-87.

57. T. F. Kelly, M. Cohen, J. B. Vandersande, Metall. Trans. A, vol. 15, pp. 819-33.

58. J. V. Wood, R. W. K. Honeycombe, Mat. Sci. Eng., 1976, vol. 23, pp. 107-112.

59. Y. Nishi, M. Tachi, E. Yajima, Scripta Metall., 1985, vol. 19, pp. 865-66.

60. T. Okamoto, K. Kishitake, K. Murakami, Trans. Iron and Steel Institute of Japan, 1981, vol. 21, pp. 641-648.

61. "Structural Uses for Ductile Ordered Alloys", National Materials Advisory Board, NRC Report, 1984.

62. C. C. Koch, in "High Temperature Ordered Intermetallic Alloys", Materials Research Society Symposium Proceedings, vol. 39, MRS, 1985, p397.

63. R. H. Titran, K. M. Vedula, G. G. Anderson, ref. 62, p309.

64. D. J. Gaydosh, R. W. Jech, R. H. Titran, J. Mat. Sci. Letters, 1985, vol. 4, pp. 138-40.

65. E. M. Schulson, P. R. Barker, Scripta Metall., 1983, vol. 17, p519.

66. K. M. Vedula, private communication to J. H. Devletian, 1985.

67. D. J. Gaydosh, M. Crimp, ref. 62, pp. 429-36.

68. S. A. David, W. A. Jemian, C. T. Liu, J. A. Horton, Weld. J., 1985, vol. 64, pp. 22s-28s.

69. L. S. Durrell, Welding and Metal Fabrication, 1961, vol. 29, pp. 216-18.

70. Metals Handbook, 9th Edition, vol. 6, ASM, Metals Park, 1985, p739.

71. P. T. Houldcroft, "Welding Process Technology", Cambridge University Press, 1977, p126.

72. N. A. Chvertko, Auto. Weld., 1973, vol. 26, pp. 50-53.

73. S. C. Hsu, S. Chakravorty, R. Mehrabian, Met. Trans. B, 1978, vol. 9, p221.

74. L. E. Greenwald, E. M. Breinan, B. H. Kear, "Laser-Solid Interactions and Laser Processing - 1978", S. D. Ferris

et. al., editors, American Institute of Physics, 1979, p189.

75. P. H. Shingu, R. Ozaki, Metall. Trans. A, 1975, vol. 6, pp.33-37.

76. R. C. Ruhl, Mat. Sci. Eng., 1967, vol. 1, pp. 313-20.

77. V. E. Movarskii, D. M. Kaleko, N. A. Chvertko, Autom. Weld., 1975, vol. 28, pp. 38-40.

78. N. A. Chvertko, D. M. Kaleko, Autom. Weld., 1976, vol. 29, pp. 41-42.

79. D. Danks, MS Thesis, Oregon Graduate Center, 1986.

80. V. P. Kujanpaa, S. A. David, and C. L. White, Weld. J., 1986, vol.65, pp. 203s-212s.

81. T. Fujimura, J. K. Brimacombe, Trans. Iron and Steel Institute of Japan, 1986, vol. 26, pp. 532-539.

82. Einerson et al., EG & G, Idaho, 1986.

83. J. H. Perepezko, Metall. Trans. A, 1984, vol. 15, pp. 437-447.

84. J. C. Lippold, W. F. Savage, Weld. J., 1979, vol. 60, pp. 362s-374s.

85. M. Hillert, Metall. Trans. A, 1984, vol. 15, pp. 411-419.

86. L. R. Morris, W. C. Winegard, J. Crystal Growth, 1969, vol. 5, p 361.

87. T. Takalo, N. Suutala, T. Moisio, Met. Trans. A, 1979, vol. 10, pp. 1173-1181.

88. R. A. Von Botisk, L. N. Centurioni, G. P. Peloso, Elektrotechnik und Machinenbau, 1980, vol. 97, pp. 565-569.

89. J. H. Hollomon, D. Turnbull, Prog. Met. Phys., 1953, vol. 4, p333.

90. J. D. Hunt, Mat. Sci. Eng., 1984, vol. 65, pp. 75-83.

91. S. E. Kisakurek, J. Mat. Sci., 1984, vol. 19, pp. 2289-2305.

92. H. W. Ghent, D. W. Roberts, C. E. Hermance, H. W. Kerr, A. B. Strong, in "Arc Physics and Weld Pool Behaviour", International Conference Proceedings, The Welding Institute, Cambridge, 1980.

TABLE 1.   Chemical Compositions of Stainless Steels

ELEMENT	ASTM GRADE		
	316 (A)	304 (B)	308 (C)
C	0.03	0.04	0.014
Mn	1.61	1.15	1.75
Si	0.52	0.38	0.75
Cr	17.86	17.48	19.67
Ni	12.55	9.36	10.21
Mo	2.85	0.19	0.17
Cu	0.10	0.24	0.067
S	0.010	0.022	0.006
P	0.023	0.030	0.022
N	0.094	0.04	0.052

TABLE 2(a) Designations and Welding Conditions used for Microstructural Study of CD Welds in Stainless Steels and FeAl Ordered Alloy.

WELD DESIGNATION AND NO.	DIAMETER (mm)	CAPACITANCE (mF)	VOLTAGE (V)	DROP HEIGHT (mm)	DROP WEIGHT (N)	IGNITION TIP LENGTH(mm)
1 "SLOW" A1 to D1	6.4	80	90	51	60	1.01
2 "INTERMEDIATE" A2 to D2	6.4	80	90	76	78	0.64
3 "FAST" A3 to D3	3.2	40	90	76	41	0.32

A: 316 Stainless Steel   B: 304 Stainless Steel
C: 308   "   D: FeAl Ordered Alloy

TABLE 2(b)   Designations and Welding Conditions used for CD Welds in
            Solidification Study of CD Welding.

WELD DESIGNATION AND NO.		DIAMETER (mm)	CAPACITANCE (mF)	VOLTAGE (V)	DROP HEIGHT (mm)	DROP WEIGHT (N)	IGNITION TIP LENGTH(mm)
4	A4	3.2	40	90	76	22	0.09
5	A5	2	8	150	76	22	0.075
6	B6	6.4	80	90	51	60	2.03
7	B7	6.4	80	90	51	60	1.52

A : 316 Stainless Steel   B : 304 Stainless Steel
C : 308   "   D : FeAl Ordered Alloy

Table 3.   Chromium and Nickel Equivalents and Predicted Solidification
Modes for Stainless Steels.

Stainless Steel Grade	316	304	308
DeLong Equivalents:			
Cr Eq.	21.49	18.24	21.00
Ni Eq.	17.08	12.48	13.22
Cr Eq./Ni Eq.	1.26	1.46	1.59
Predicted FN	2	2	10
Actual FN	2-3	2-4	9-10
Hammar-Svensson Equivalents:			
Cr Eq.	22.54	18.31	21.06
Ni Eq.	15.14	11.48	11.94
Cr Eq./Ni Eq.	1.49	1.59	1.76
Predicted Solidification Mode:	AF	FA	FA-F

TABLE 4 . Diffusion Behaviour of Cr and Ni in bcc and fcc Iron at
High Temperature (data from ref. 56)

Temp C	$^{fcc}D_{Cr}$ cm^2/s	$^{bcc}D_{Cr}$ cm^2/s	$*2(Dt)^{1/2}$ in μm for Diffusion times in bcc(ms)		
			1	10	100
1350	2.34EE(−10)	5.17EE(−8)	0.144	0.454	1.44
1250	6.56EE(−11)	1.62EE(−8)	0.08	0.25	0.8

* Average diffusion distances in bcc iron for various diffusion times.

TABLE 5. Material Constants Used and Estimated Absolute Stability Velocities for Stainless Steels and FeAl.

Alloy	C_0	m_L	k	D_L	T_m	Γ
	wt%	K/wt%		cm^2/s	K	K cm
Stainless	18–20 Cr		0.83	5 EE(−6)	1683–	1.579 EE(−5)
Steels	9–12.5 Ni		0.95		1698	
FeAl	24	11.47	0.88	3 EE(−5)	1643	1.986 EE(−5)

Stainless Steel data from ref. 60, Al diffusion data from ref. 93.

$$R_{abs} = \frac{C_0 m_L (1-k) D_L}{k^2 \Gamma}$$

Estimated R_{abs} :

Stainless Steels   –   50–60 cm/s

FeAl   –   64.4 cm/s

TABLE 6. Growth Rates and Solute Peclet Numbers Calculated for
Solidification During CD Welding of 316 Stainless Steel
and FeAl Ordered Alloy.

WELD		GR K/s	R cm/s	P
316 Stainless	A1	6.517 EE(6)	9.3	16.4
Steel	A3	2.045 EE(7)	21.4	31.2
	A5	5.540 EE(7)	33.4	46.3
FeAl	D1		4.8	
	D2	10^5–10^6	5.4	1–2
	D3		11.0	
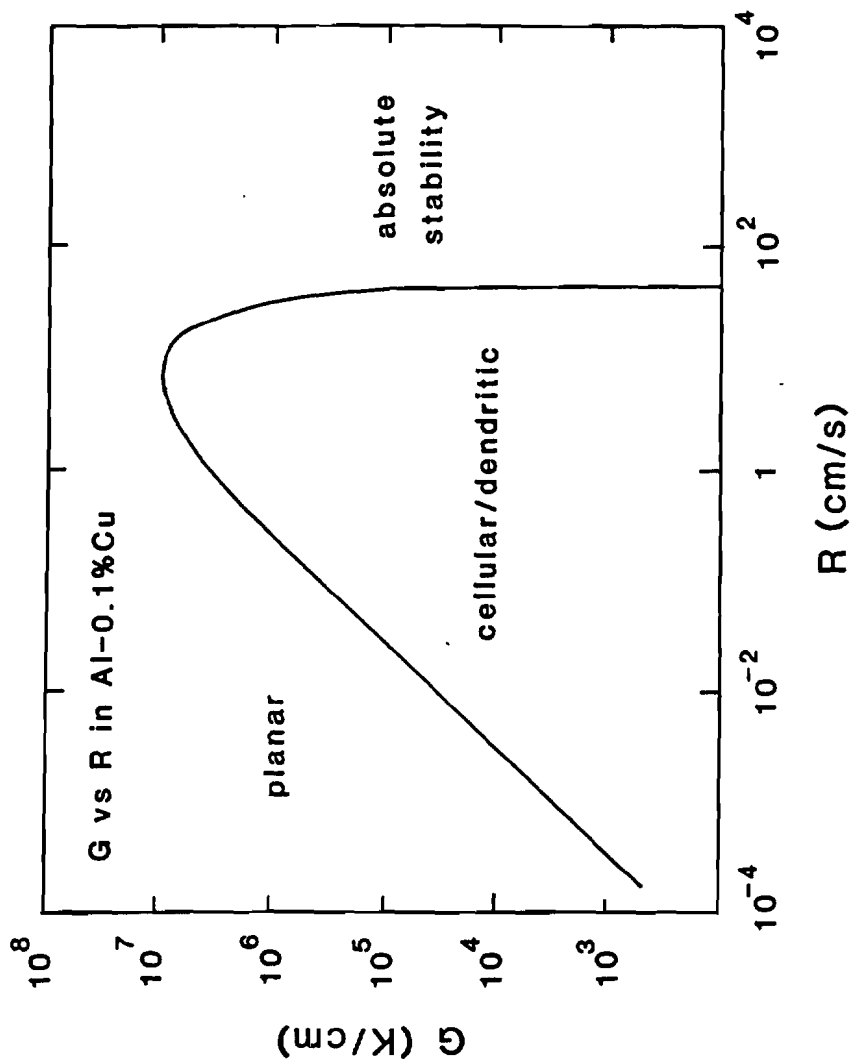
Figure 1. Interface stability as a function of G and R at constant composition for Al-0.1% Cu alloy. The curve represents boundary between stable planar growth and unstable dendritic growth [from ref. 23].
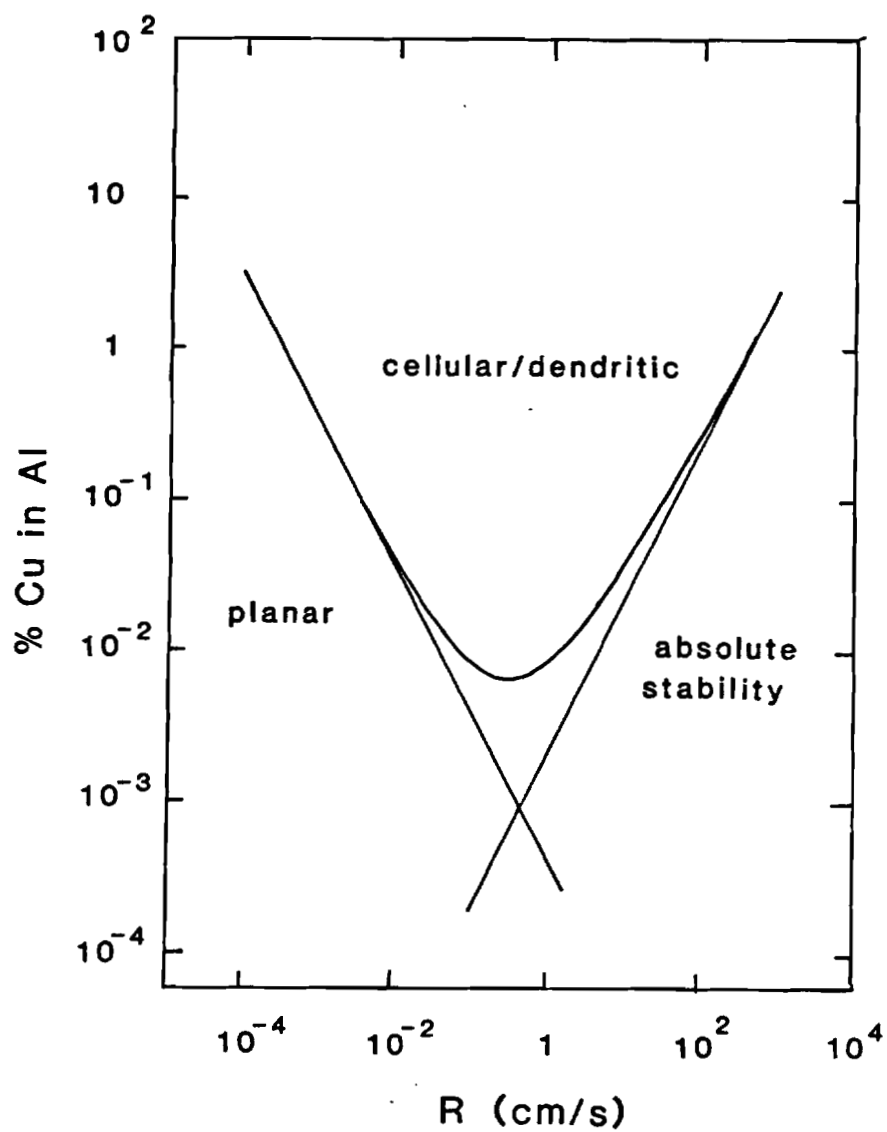
Figure 2. Interface stability as a function of composition and growth rate at $G = 2 \times 10^6$ K/cm for Al–Cu alloys [from ref. 34].
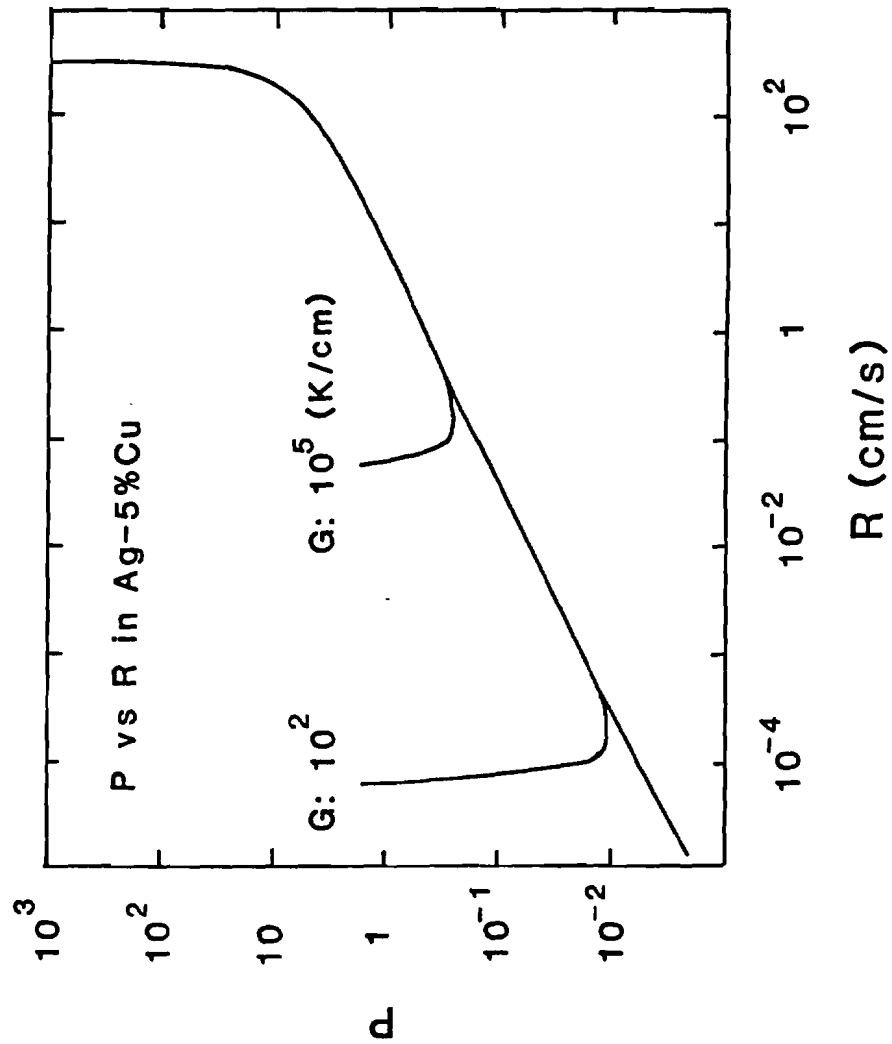
Figure 3.   Solutal Peclet number P as a function of growth rate R and gradient G for Ag-5 wt.% Cu alloy [from ref. 3].

Figure 4. The H. A. Jones PSW 100 Capacitor Discharge Welder. Recording instruments for current and voltage profiles are also shown.
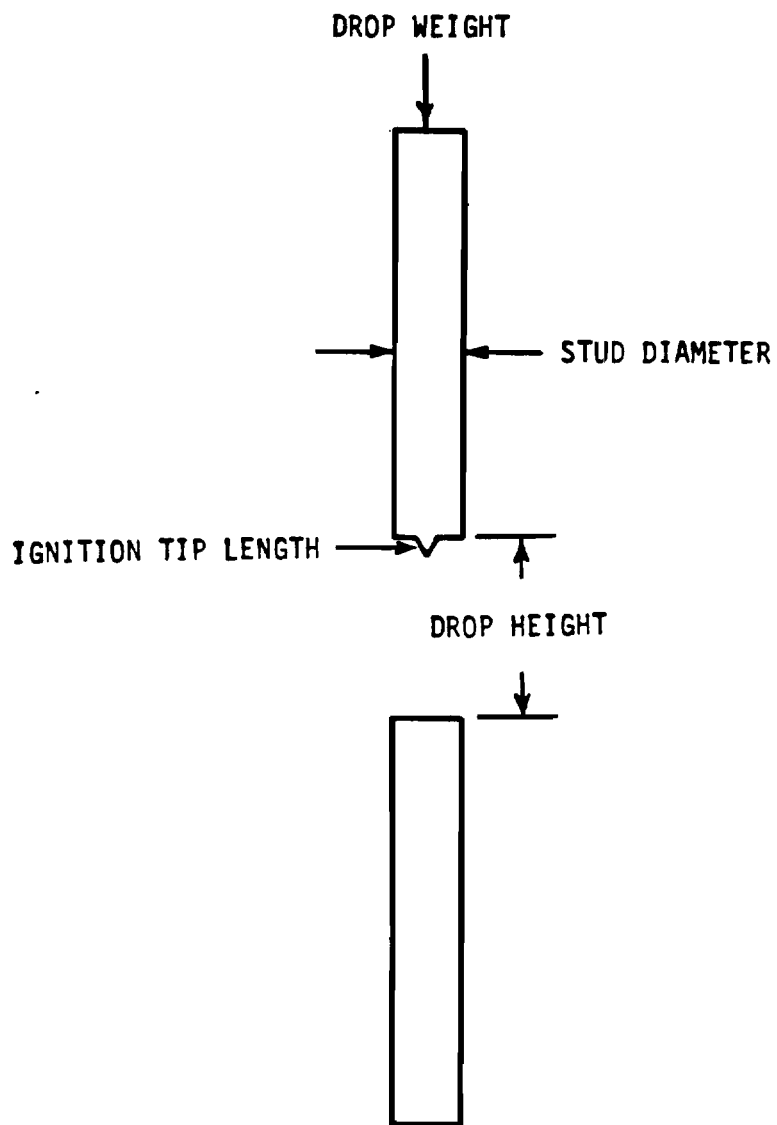
Figure 5. Setup of components to be welded by the Capacitor Discharge process showing process variables.
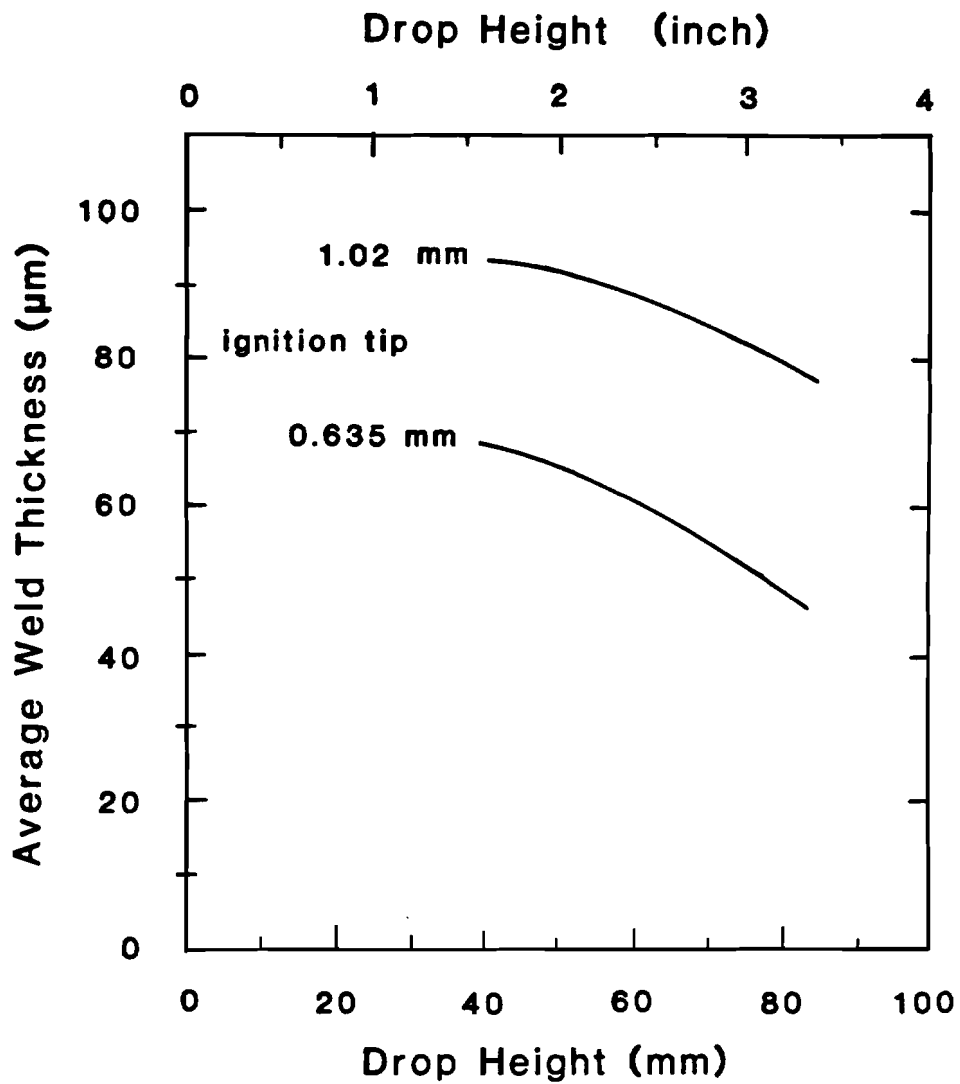
Figure 6. Average weld thickness as a function of drop height and ignition tip length during CD welding.
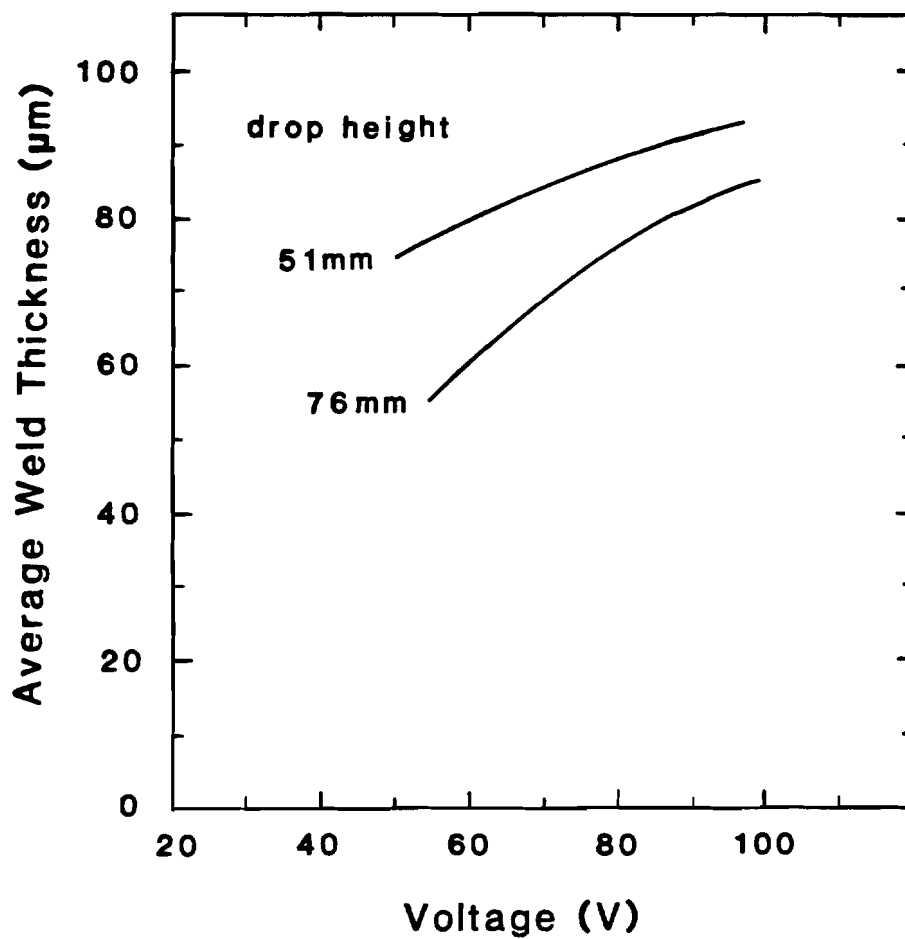
Figure 7. Average weld thickness as a function of voltage for different drop heights during CD welding.
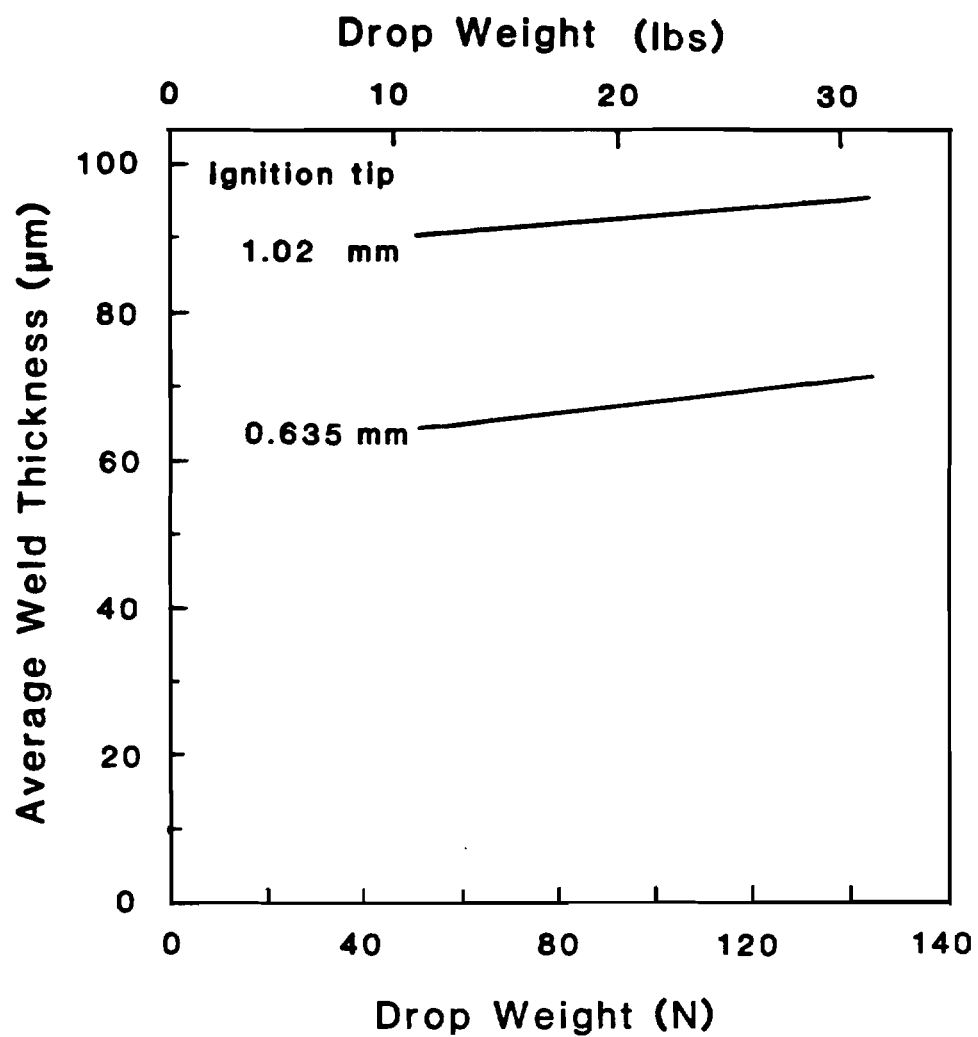
Figure 8. Average weld thickness as a function of drop weight during
CD welding for different ignition tip lengths.
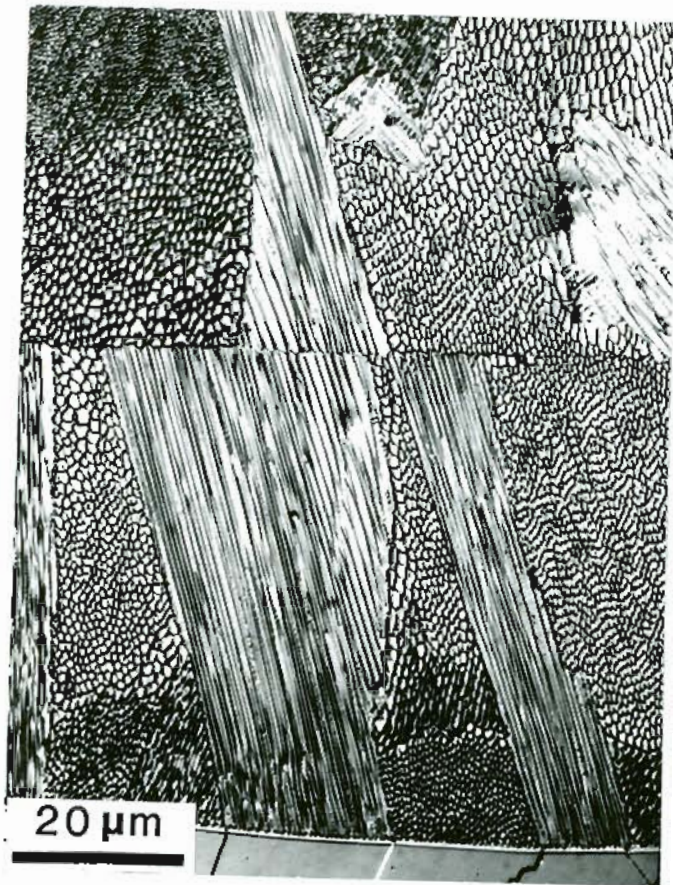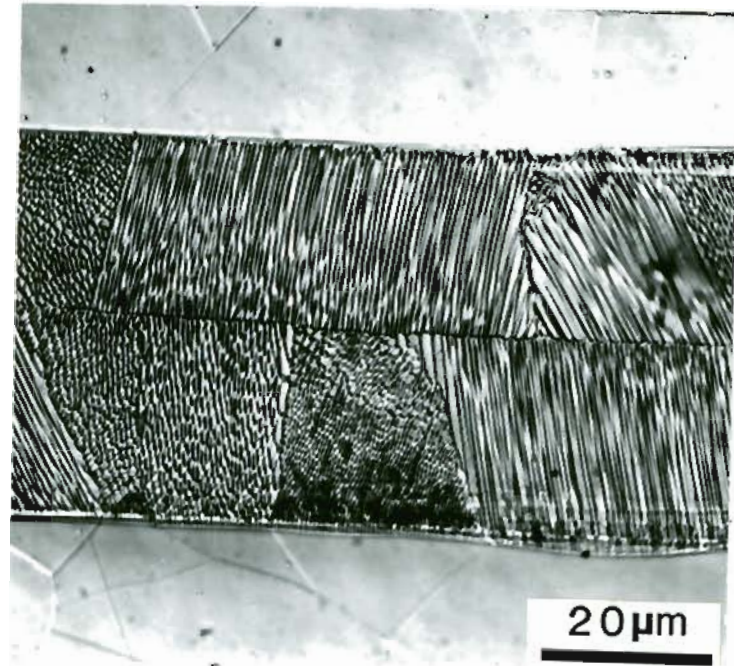
Figure 9. Dendritic structures of CD welds in 316 stainless steel under cooling conditions: (a) "Slow", (b) "Intermediate"
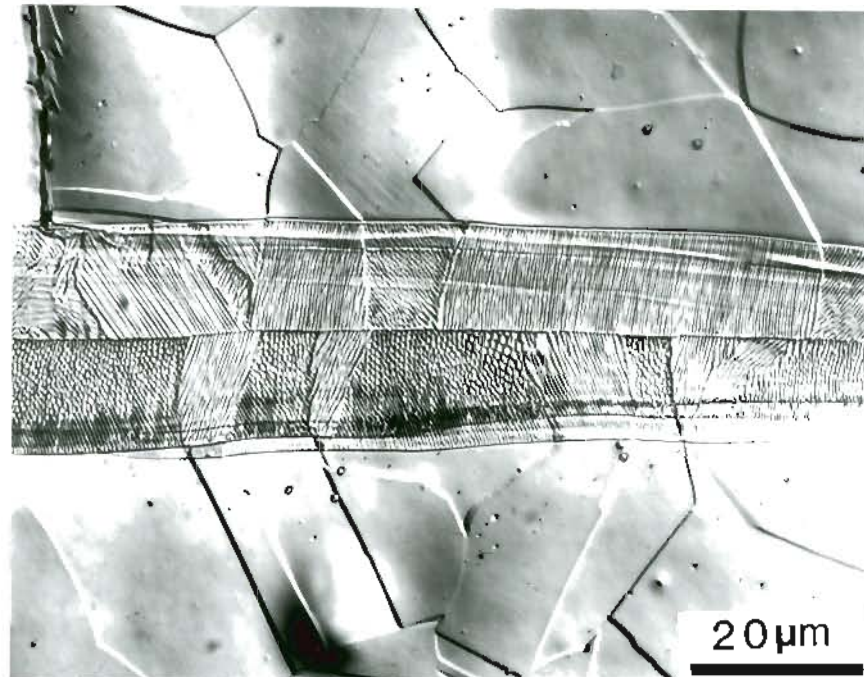
c)

Figure 9. (contd.) Dendritic structure of CD weld in 316 stainless steel under cooling condition: (c) "Fast".
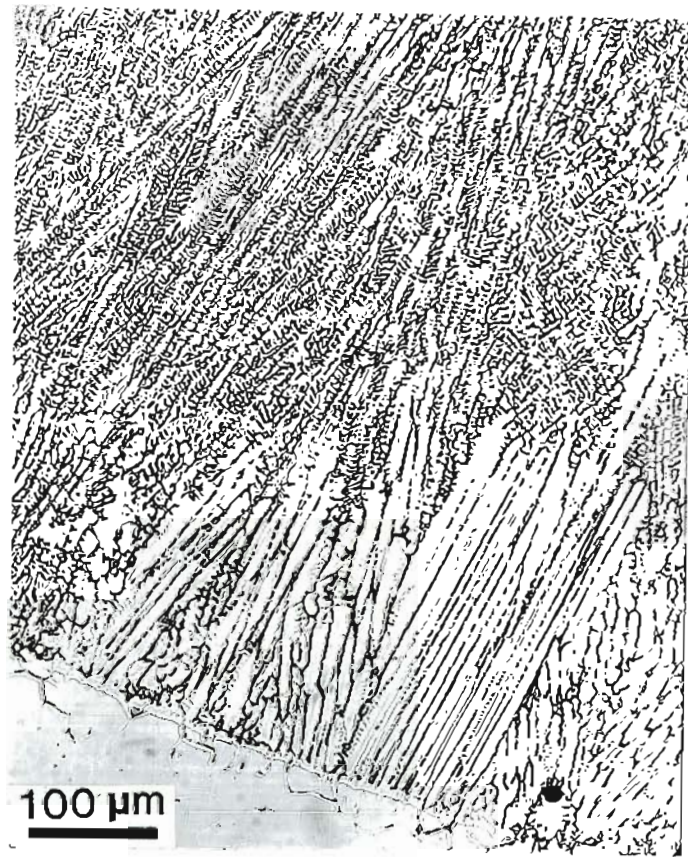
Figure 10. Dendritic structure of gas tungsten arc weld in 316
showing solidification in the primary austenitic mode
close to the base metal changing to primary ferritic
mode further into the weld.
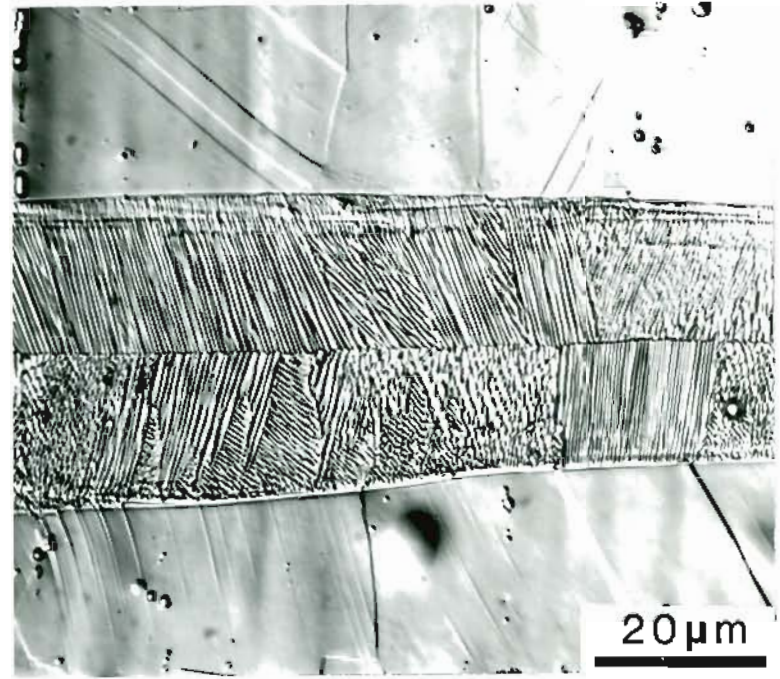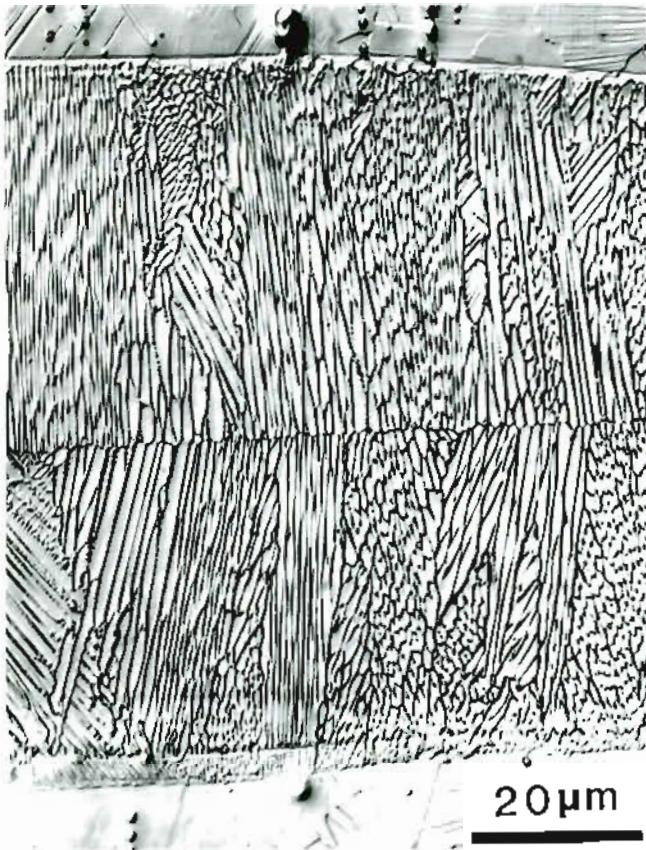
Figure 11. Dendritic structures of CD welds in 304 stainless steel under (a) "Slow" and (b) "Fast" cooling conditions.
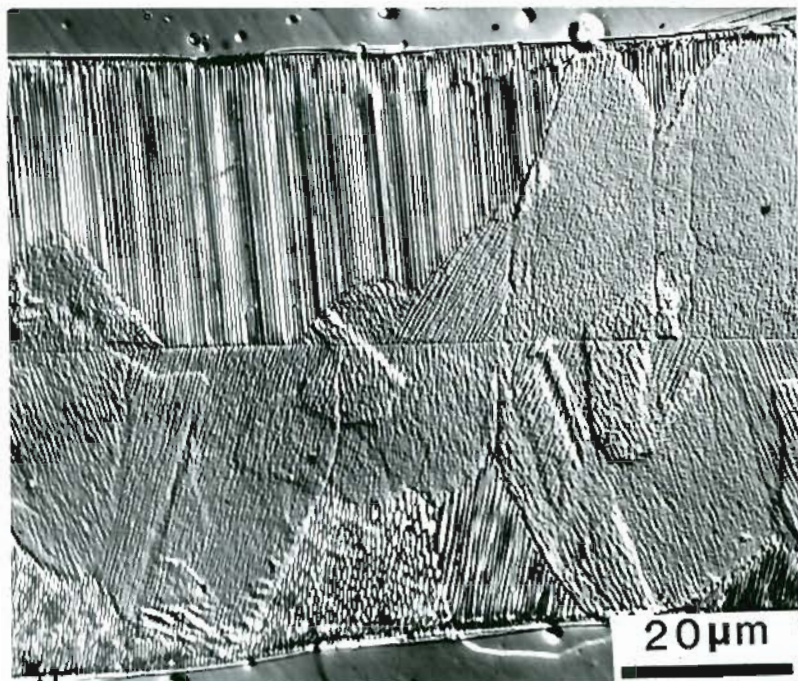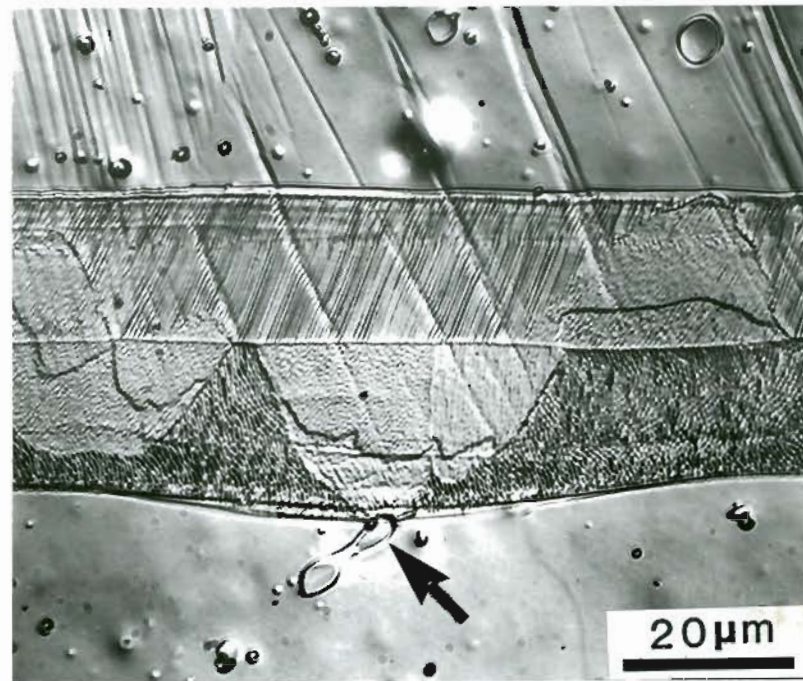
Figure 12. Dendritic structures of CD welds in 308 stainless steel under cooling conditions: (a) "Slow" and (b) "Fast". Arrow points to ferrite in contact with the fusion zone.
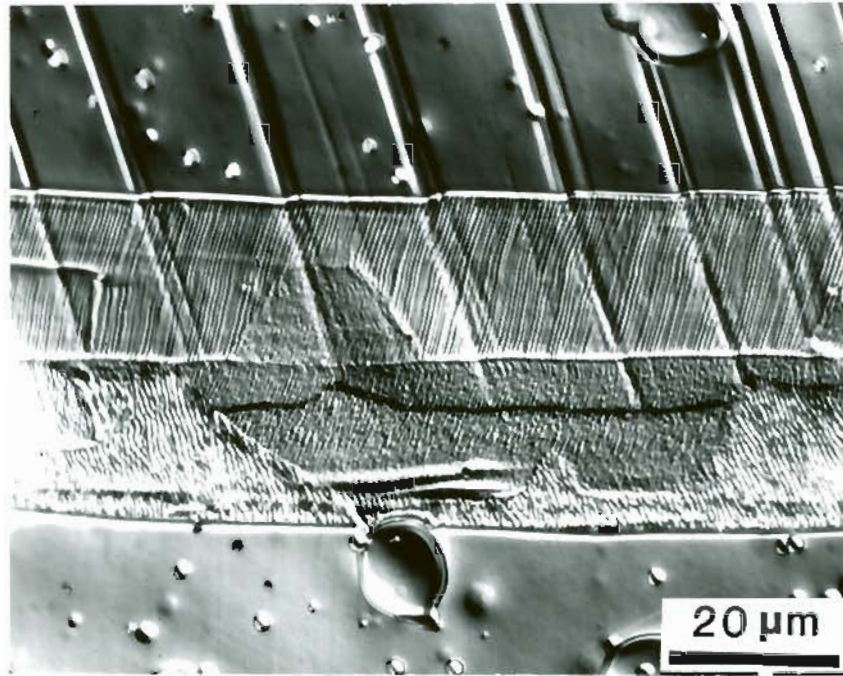
Figure 12. (contd.) Dendritic structure of "Fast" cooling CD weld
in 308 stainless steel showing: (c) slip lines across
the weld center line going from primary austenitic to
primary ferritic regions.
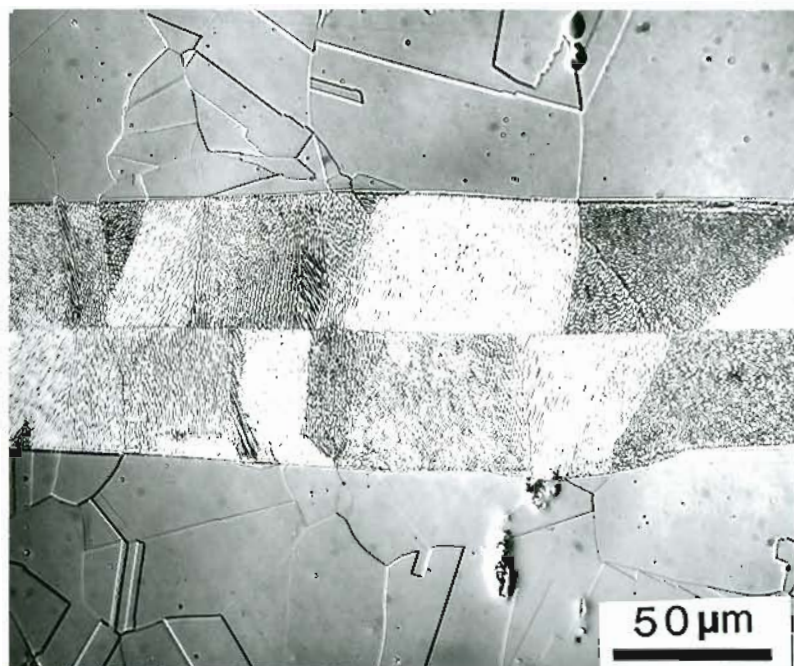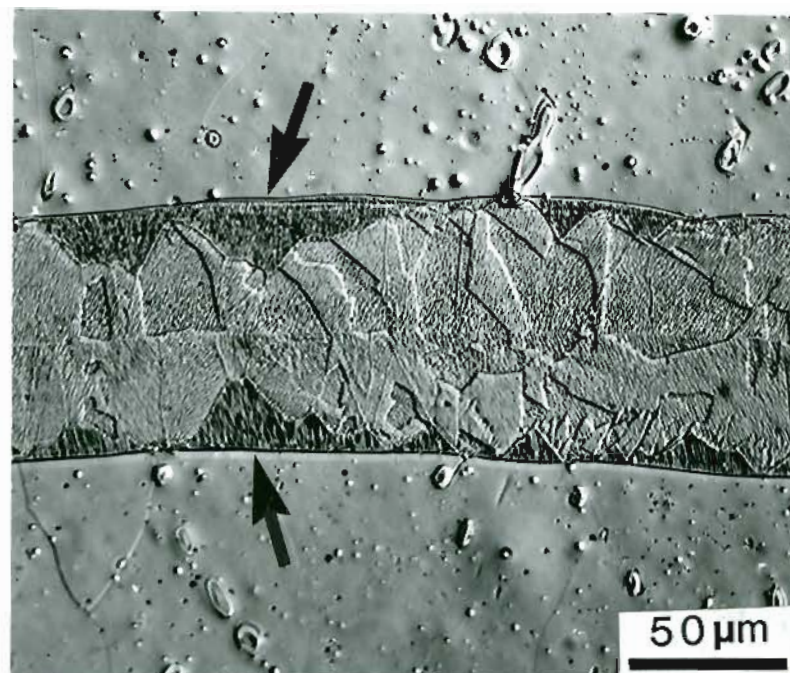
Figure 13. Microstructures of "Slow" cooling CD welds:
(a) Weld in 316 stainless steel showing fully
    epitaxial grains growing to the weld center.

(b) Weld in 308 stainless steel showing recrystallisa-
    tion across dendrites. Arrows point to primary
    austenitic regions.
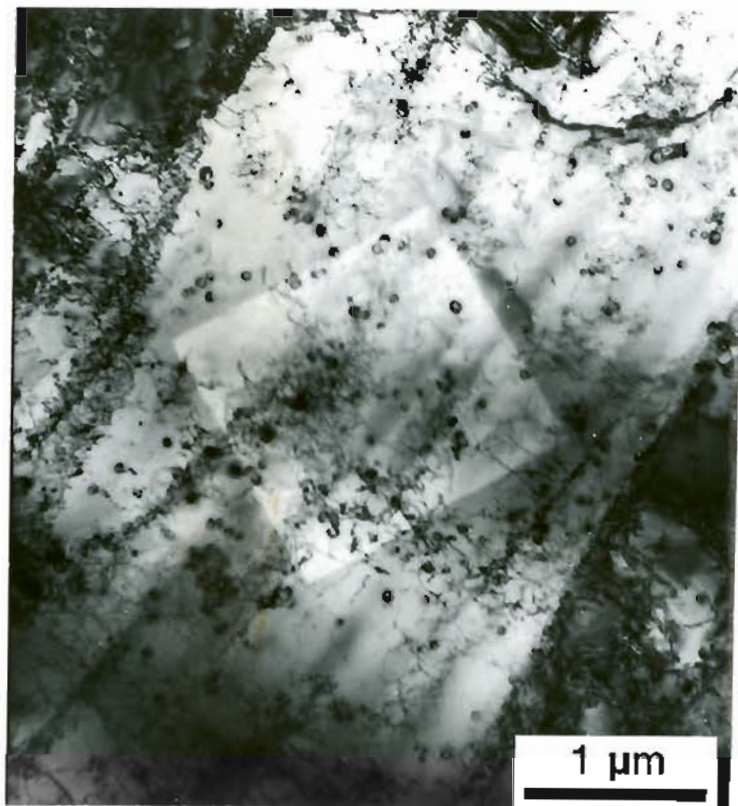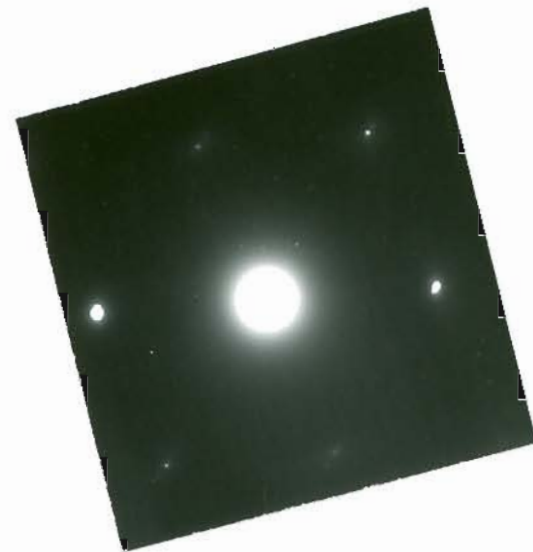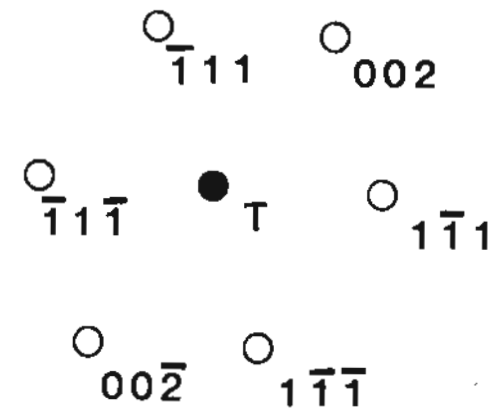
Figure 14. Transmission electron micrograph of CD weld in 304
stainless steel: (a) bright field image, and
(b) SAD pattern.
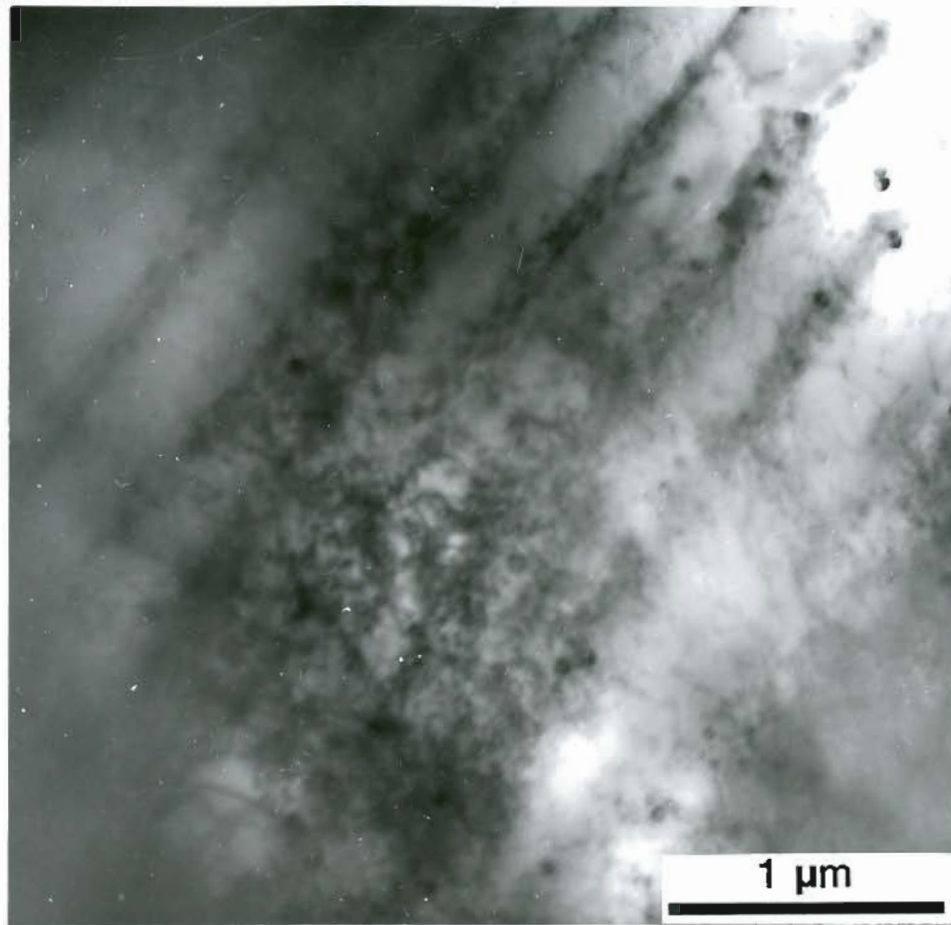
Figure 14. (contd.) Transmission electron micrograph of CD weld in 304 stainless steel: (c) bright field image.
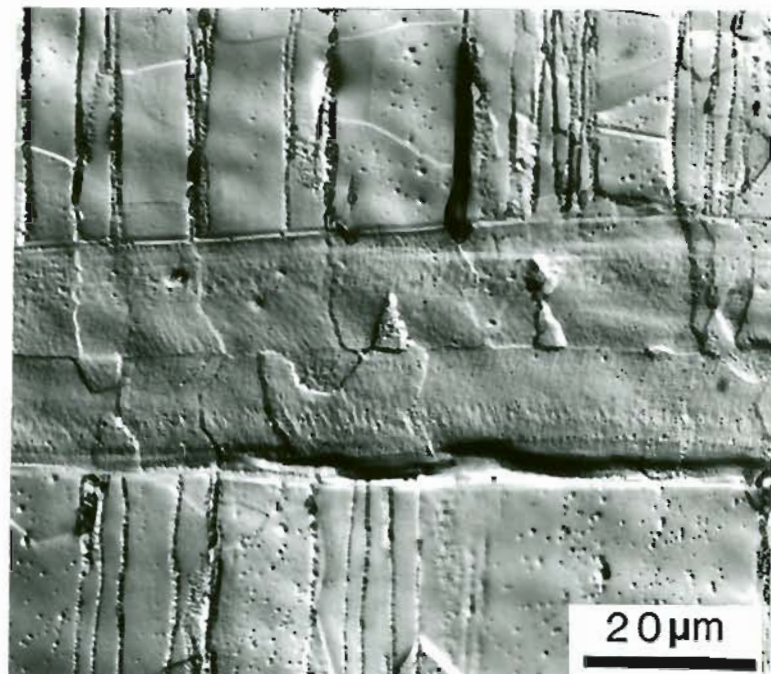
Figure 15. Dendritic structures of CD welds in FeAl ordered alloy
under cooling conditions: (a) "Slow" and
(b) "Intermediate"
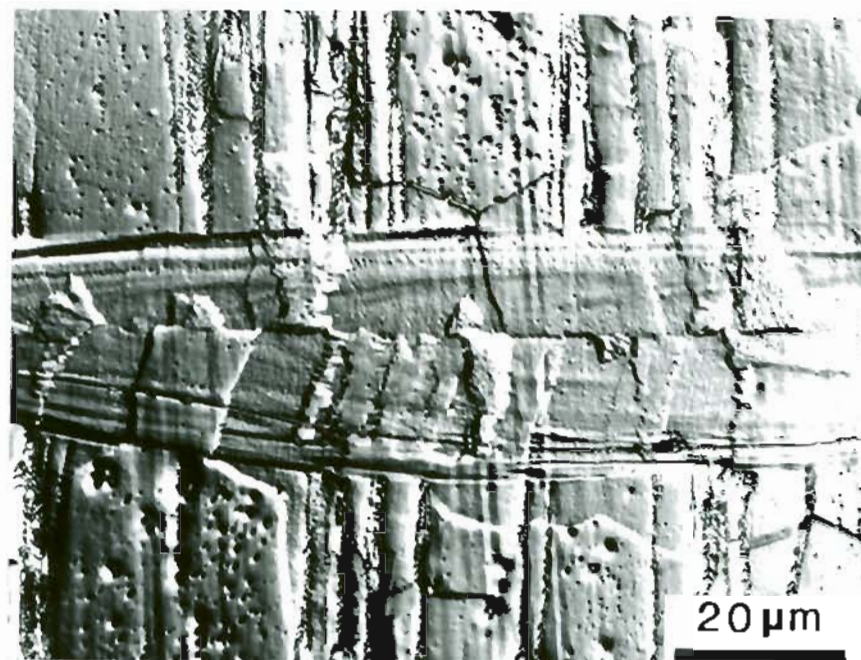
c)

Figure 15. (contd.) Dendritic structures of CD welds in FeAl Ordered
Alloy under cooling condition: (c) "Fast"
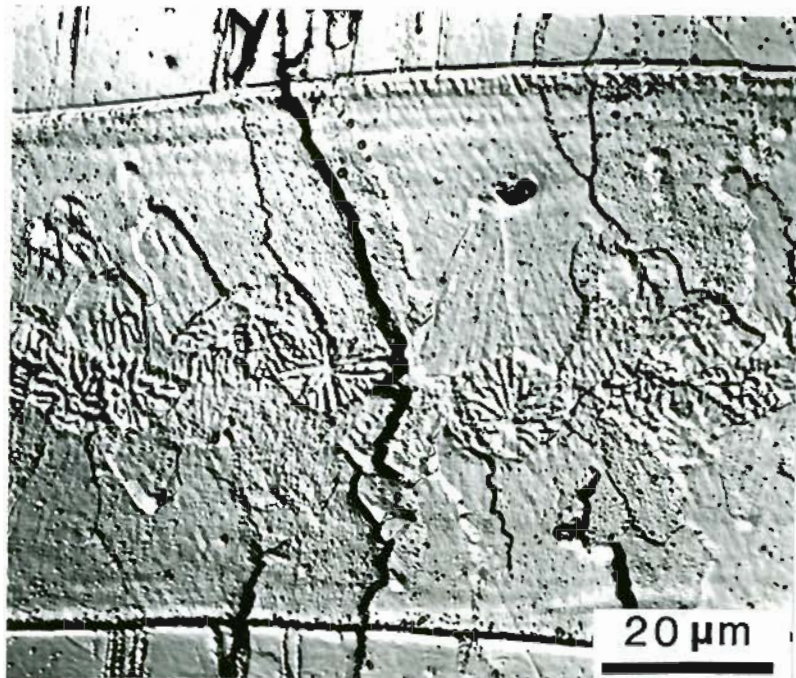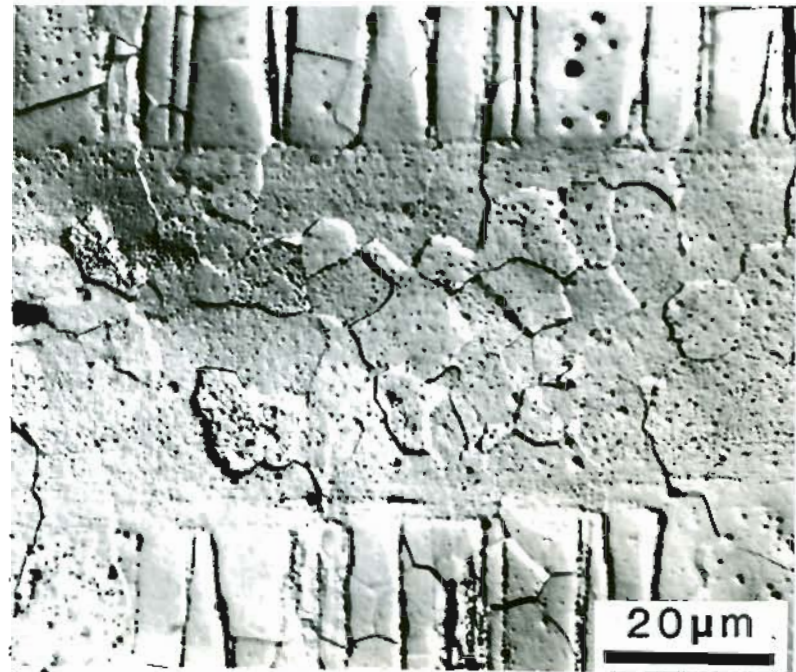
Figure 16. Dendritic structure of CD weld in FeAl Ordered Alloy
showing (a) equiaxed dendrites in "Slow" cooling weld,
and (b) after 1hr at 780°C (1400°F).
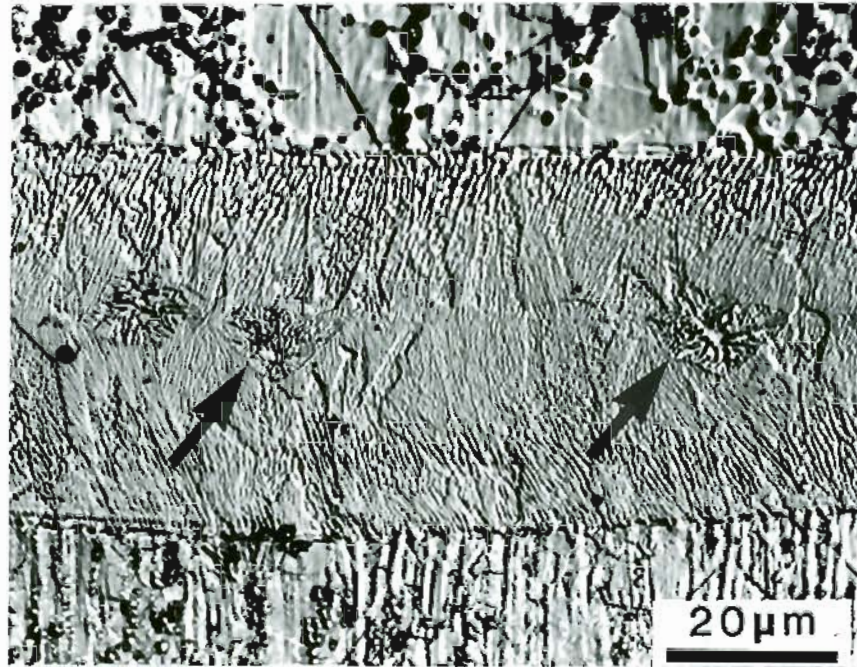
Figure 17. Equiaxed dendritic structures in CD weld in
centrifugally atomised and hot extruded 304 stainless
steel.
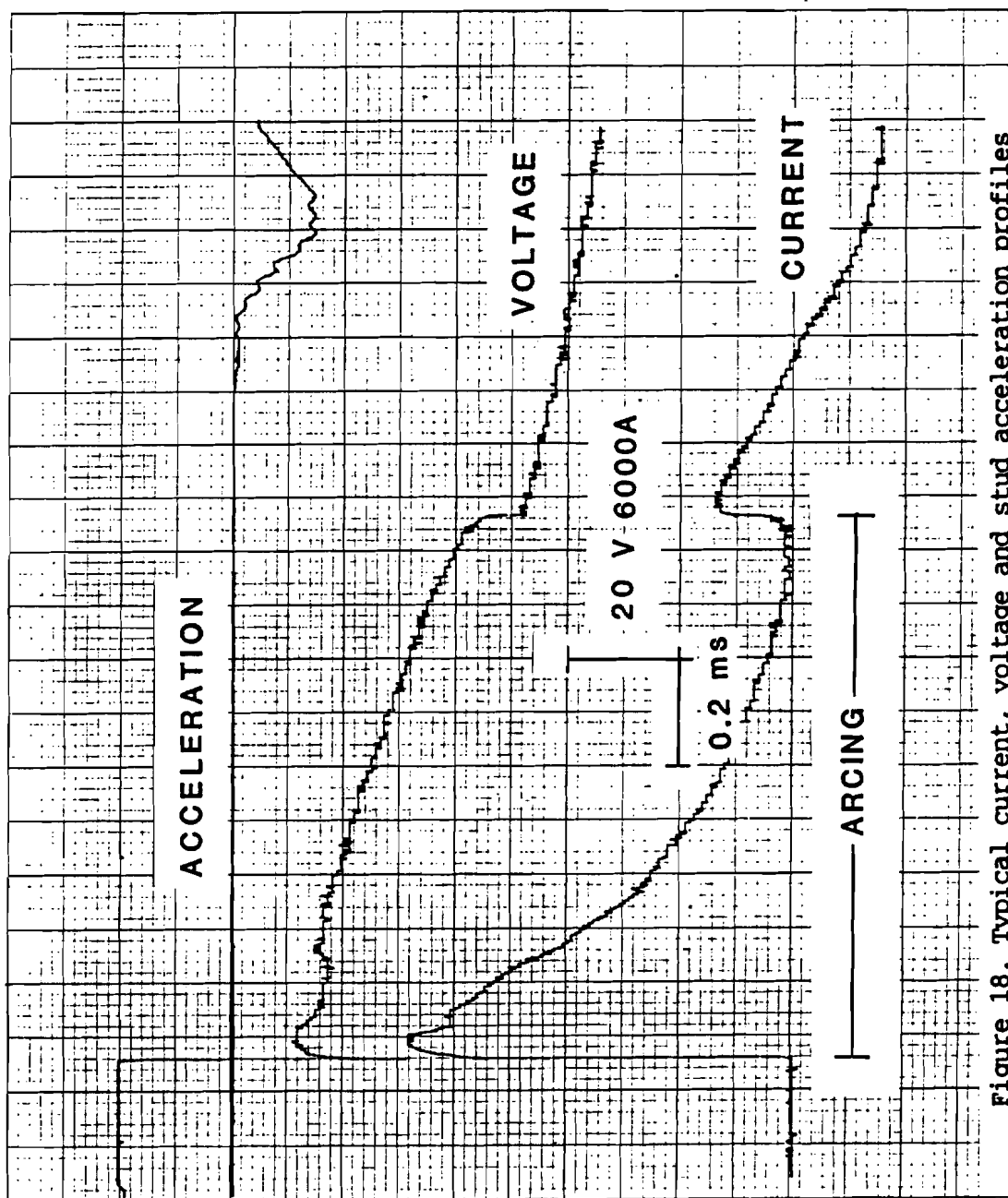
Figure 18. Typical current, voltage and stud acceleration profiles of CD welds made under: (a) "Slow" cooling condition.
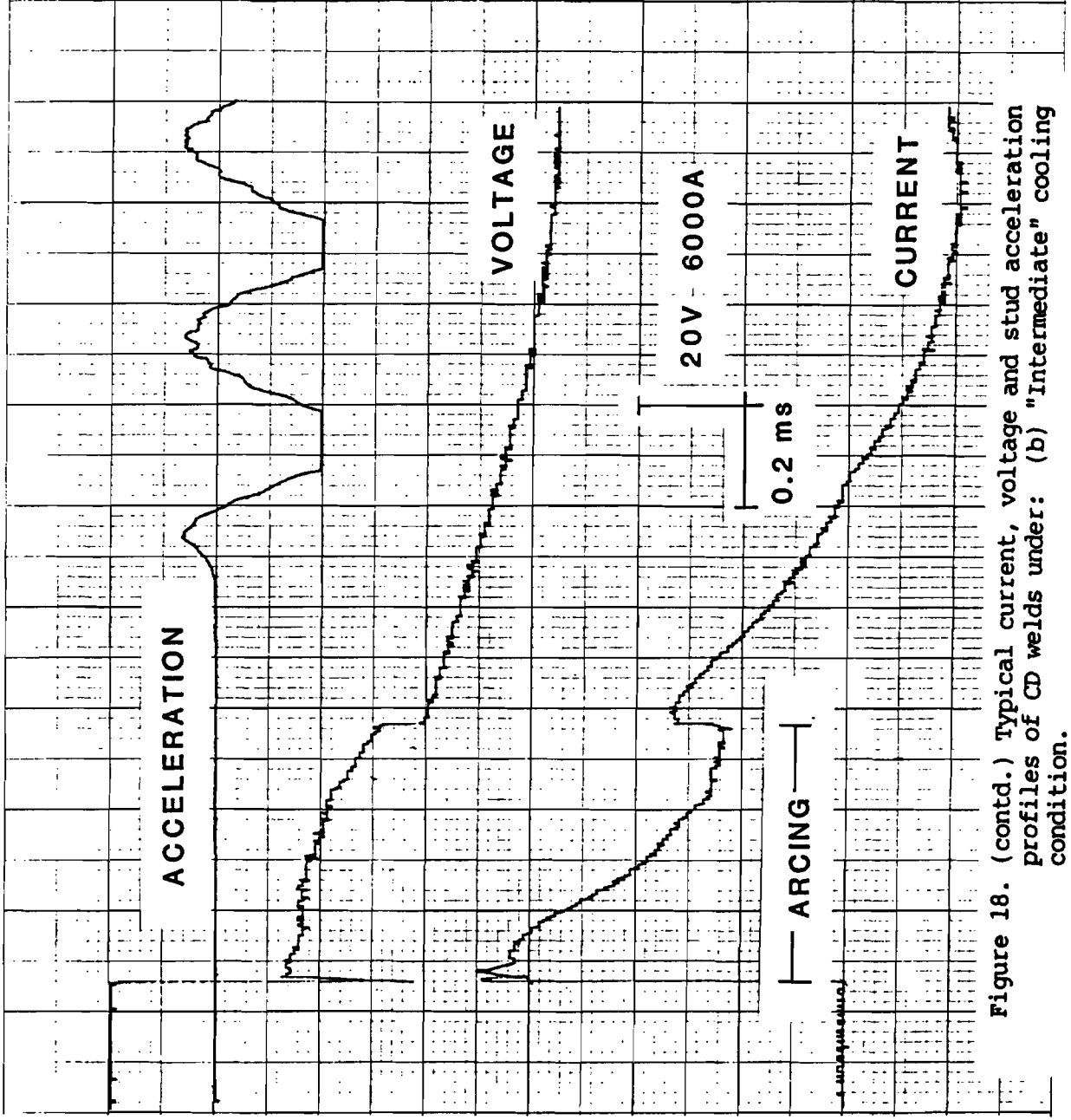
Figure 18. (contd.) Typical current, voltage and stud acceleration profiles of CD welds under: (b) "Intermediate" cooling condition.
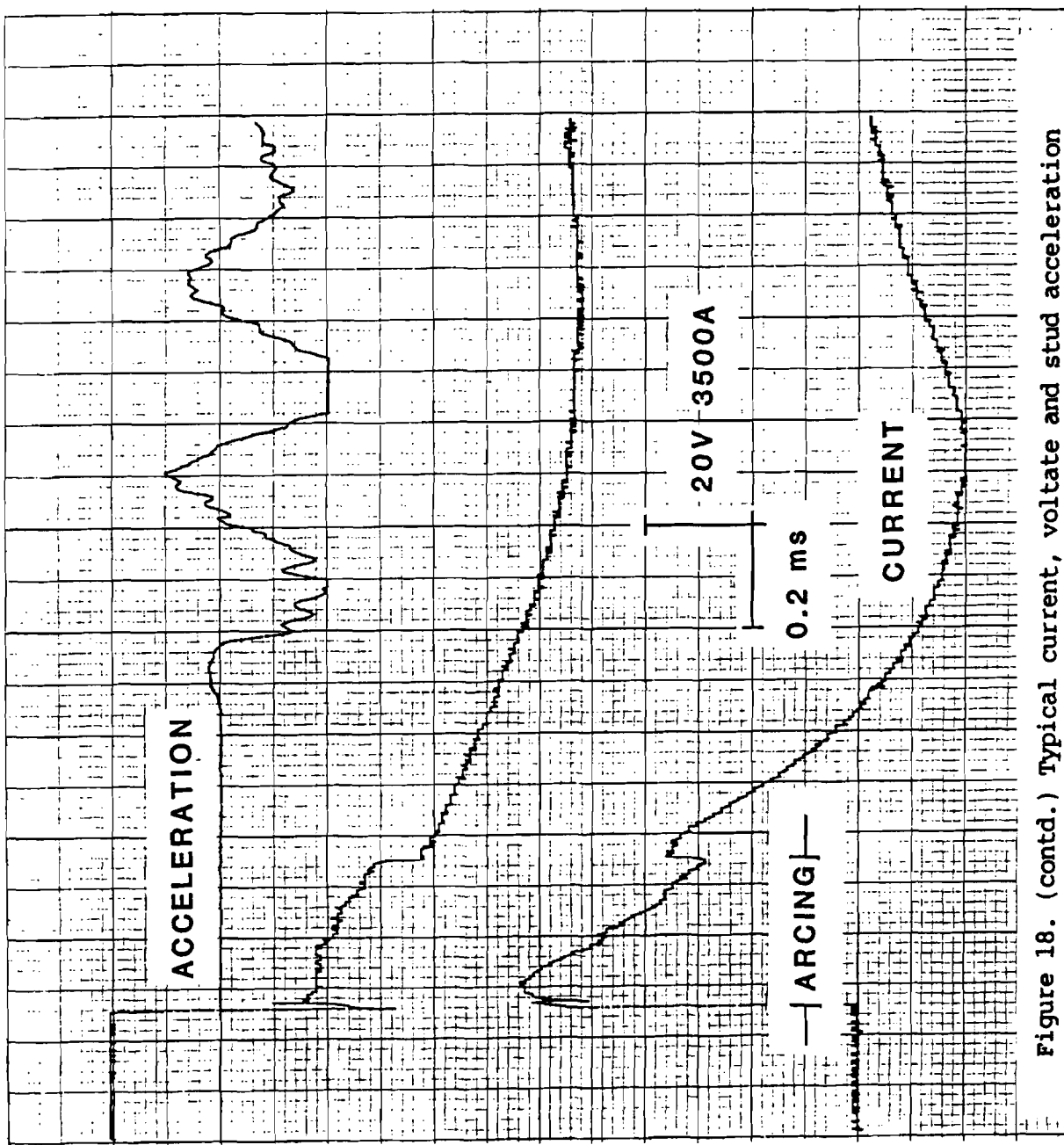
Figure 18. (contd.) Typical current, voltate and stud acceleration profiles of CD welds under: (c) "Fast" cooling condition.
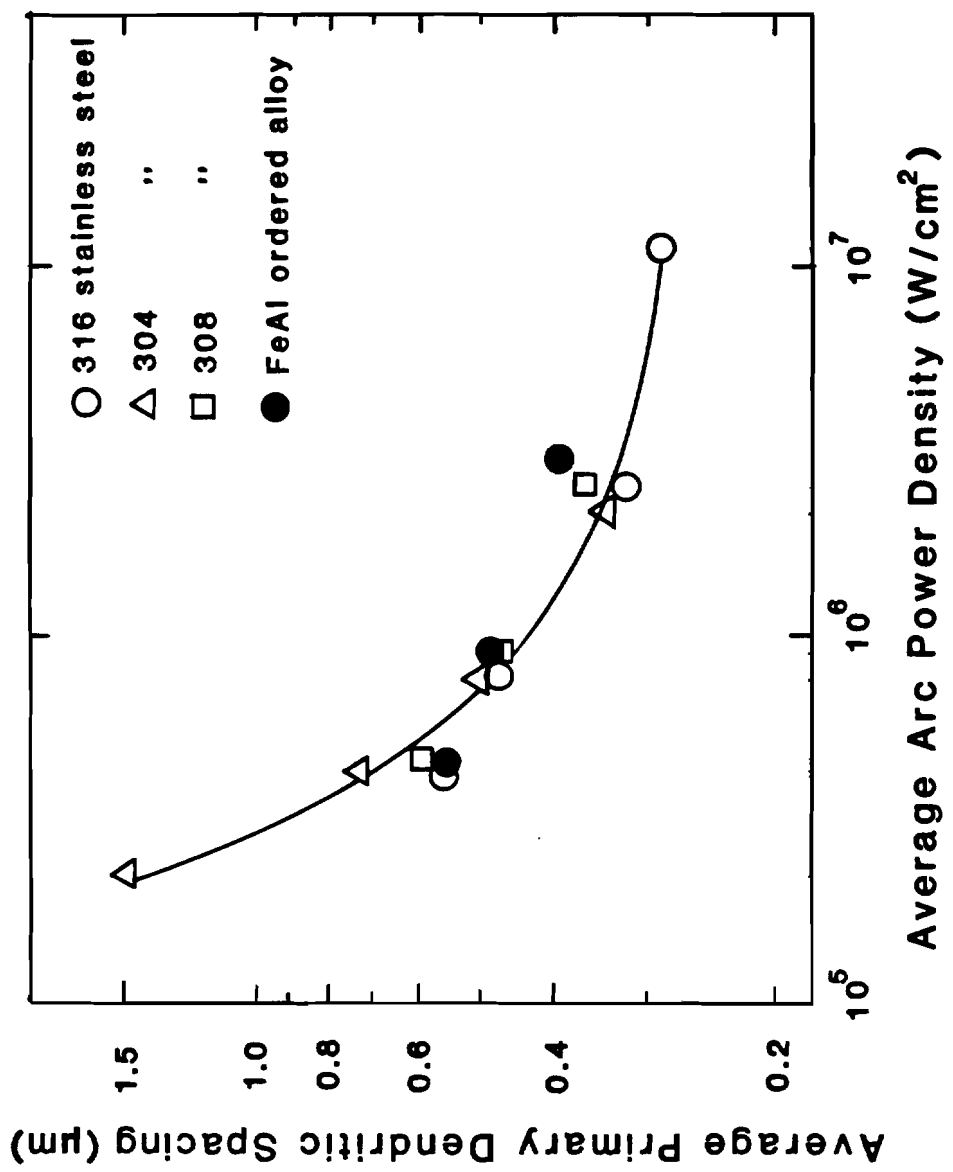
Figure 19. Primary dendritic spacings in Stainless Steels and FeAl Ordered Alloy for different arc power densities during CD welding.
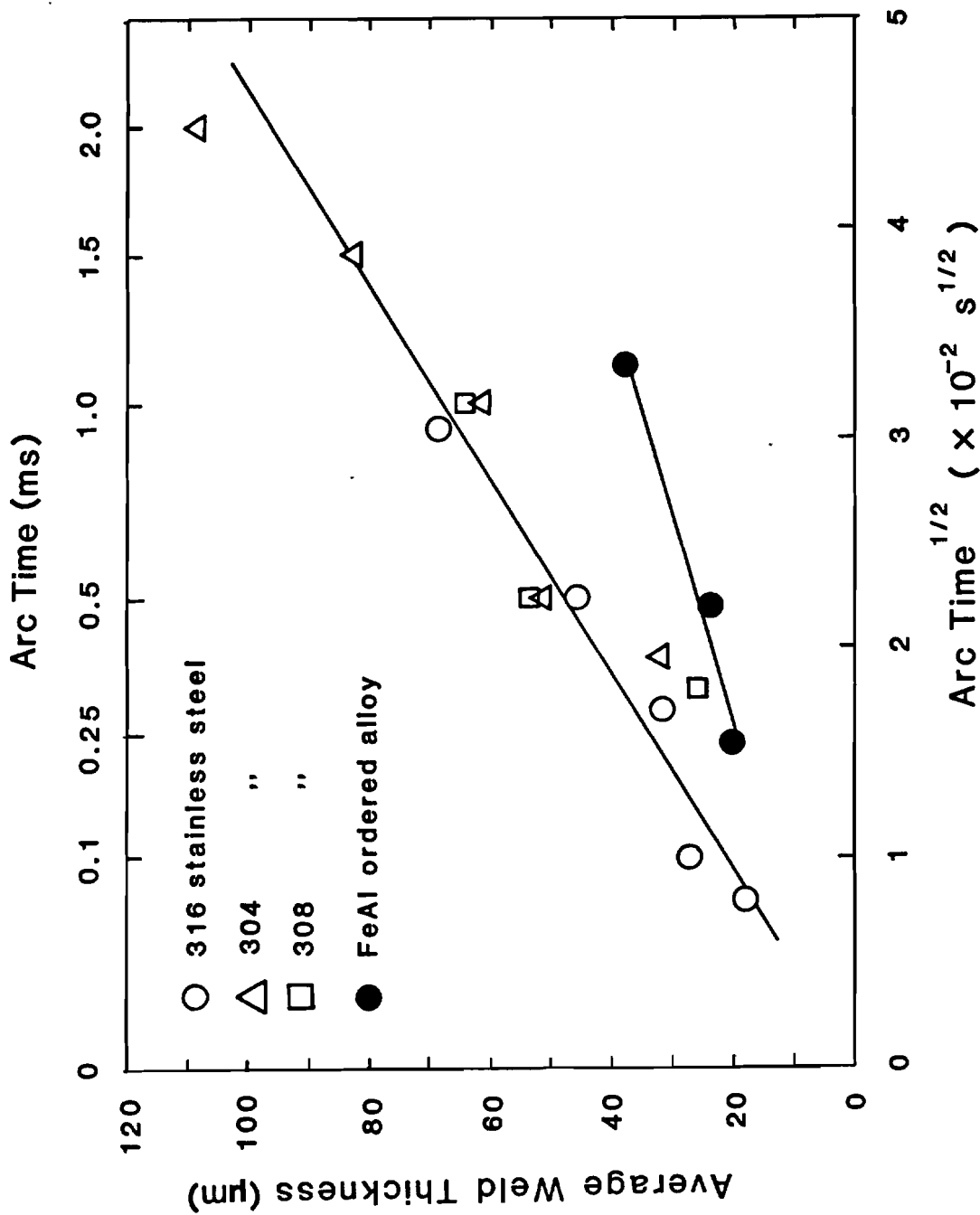
Figure 20. Average weld thickness as a function of arc time in CD welding of Stainless Steels and FeAl Ordered Alloy.
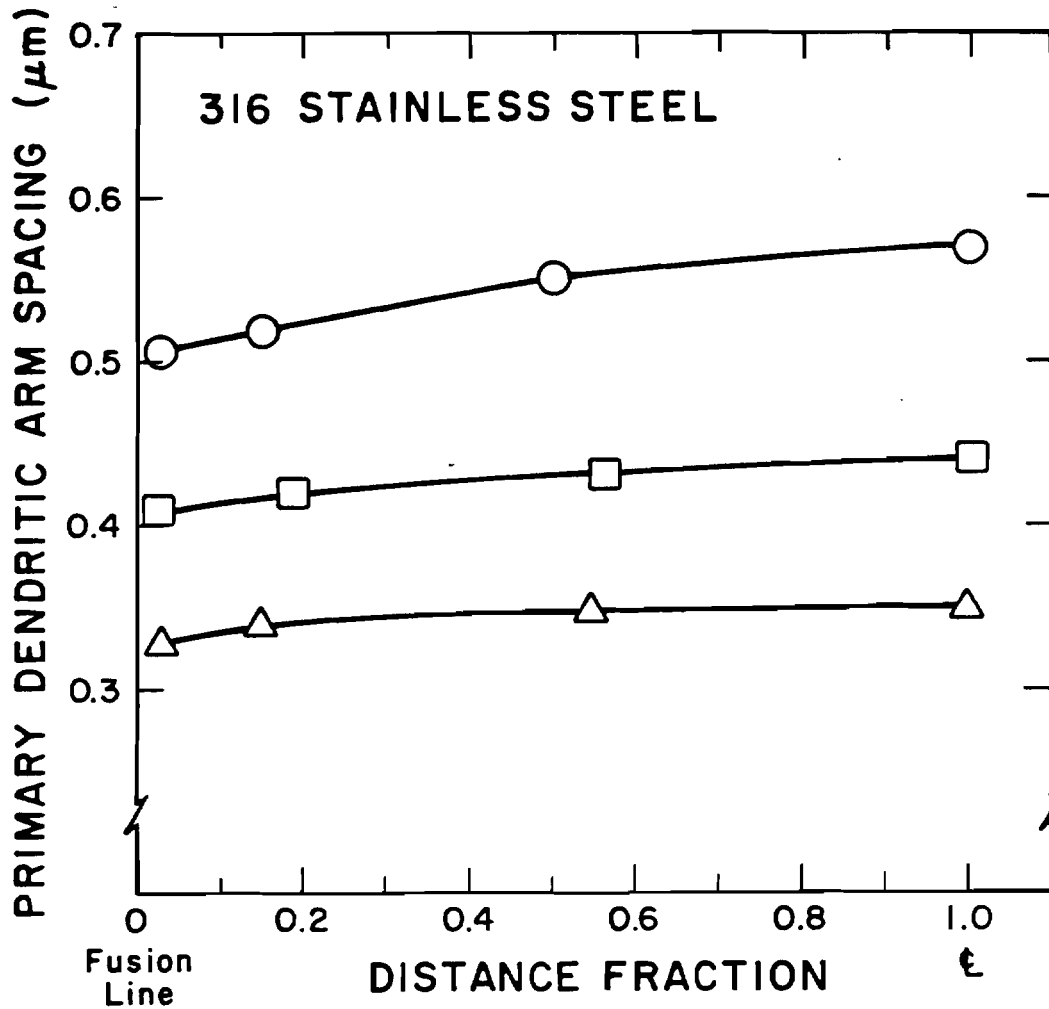
Figure 21. Variation of primary dendritic spacing in 316 Stainless
Steel CD welds as a function of fractional distance from
the fusion line to the weld center line.
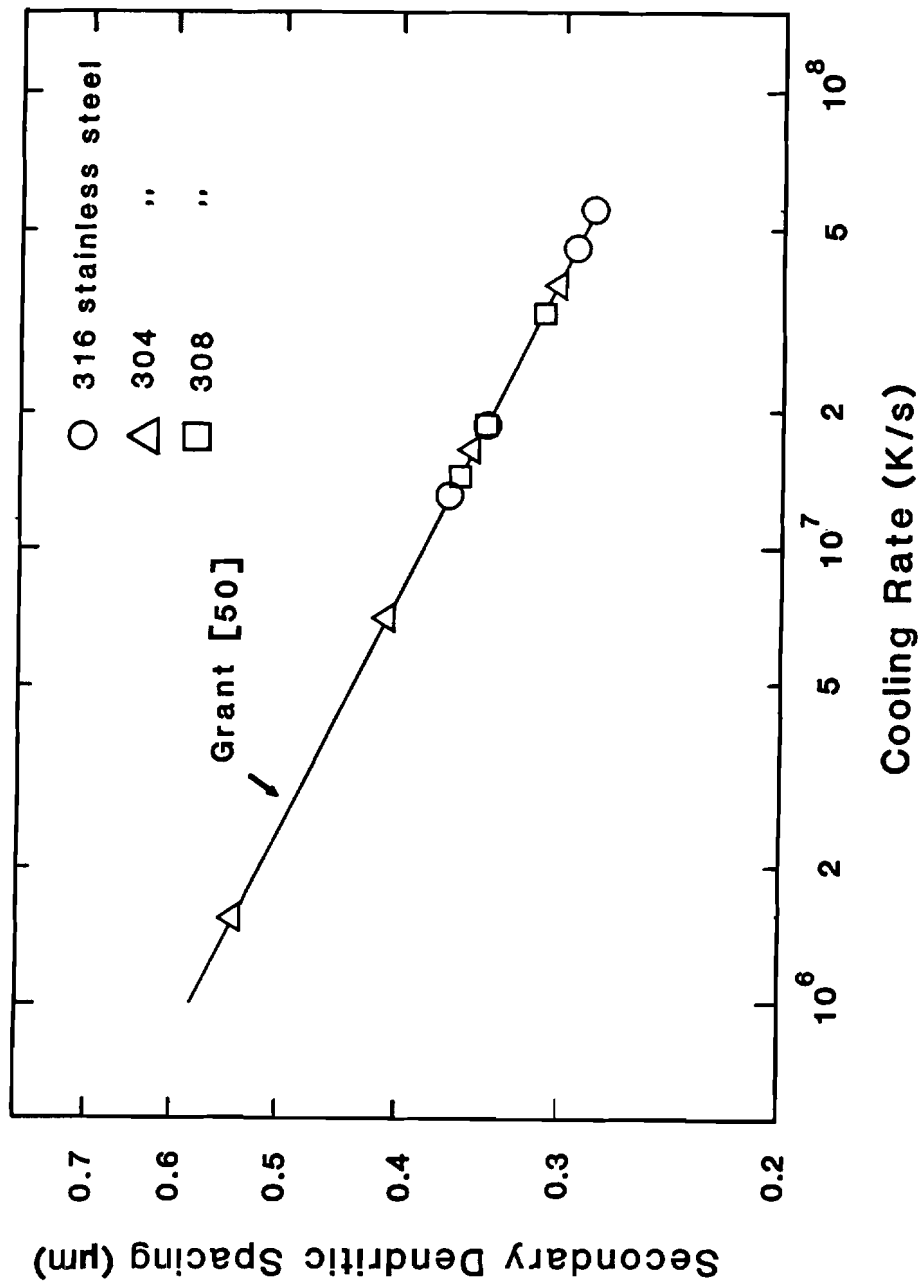
Figure 22. Cooling rates calculated from N. J. Grant's relationship using secondary dendrite arm spacings measured in stainless steel CD welds.
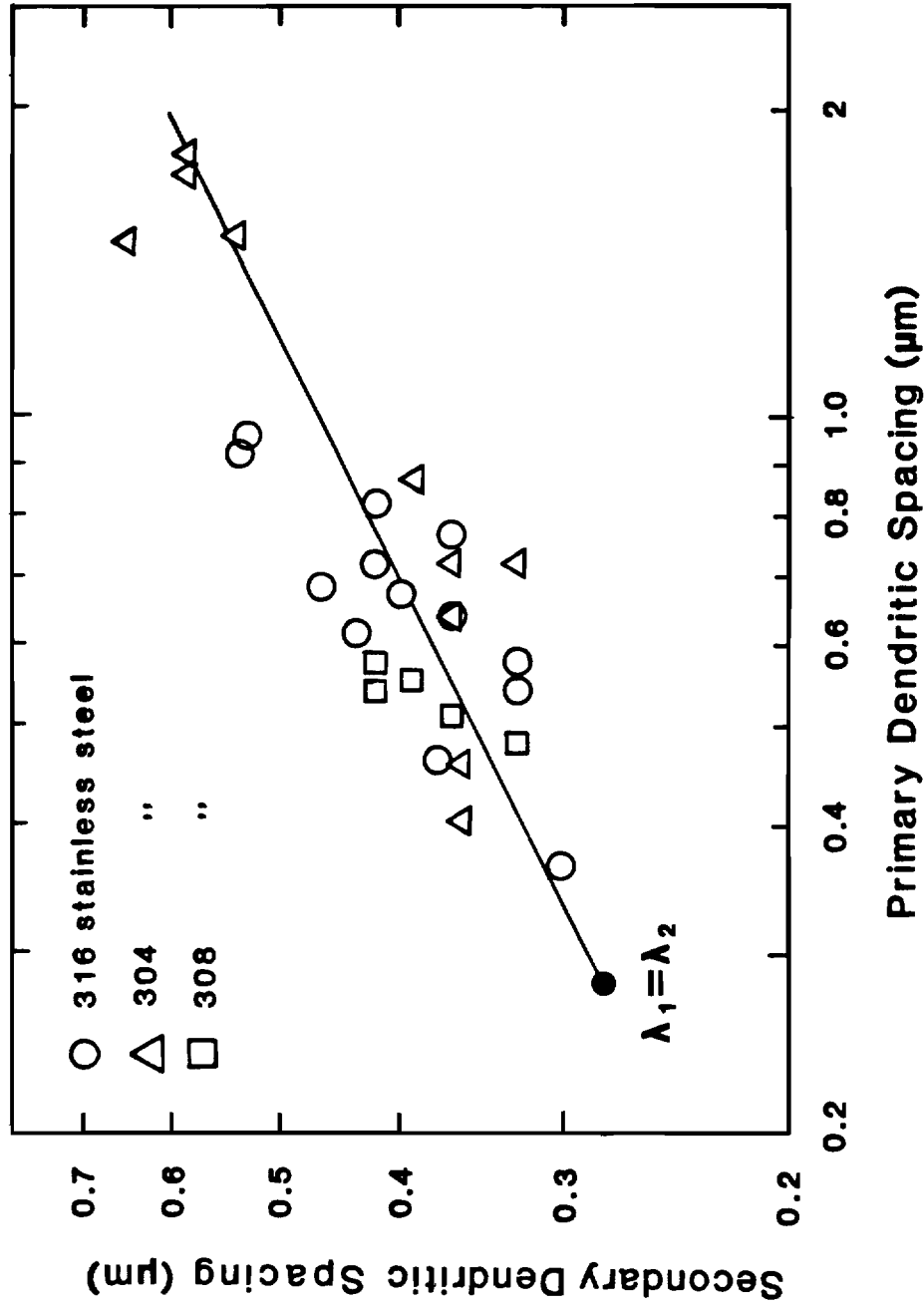
Figure 23. Relation between primary and secondary dendritic spacings in austenitic stainless steel. The point where primary and secondary dendritic spacings are equal is indicated.
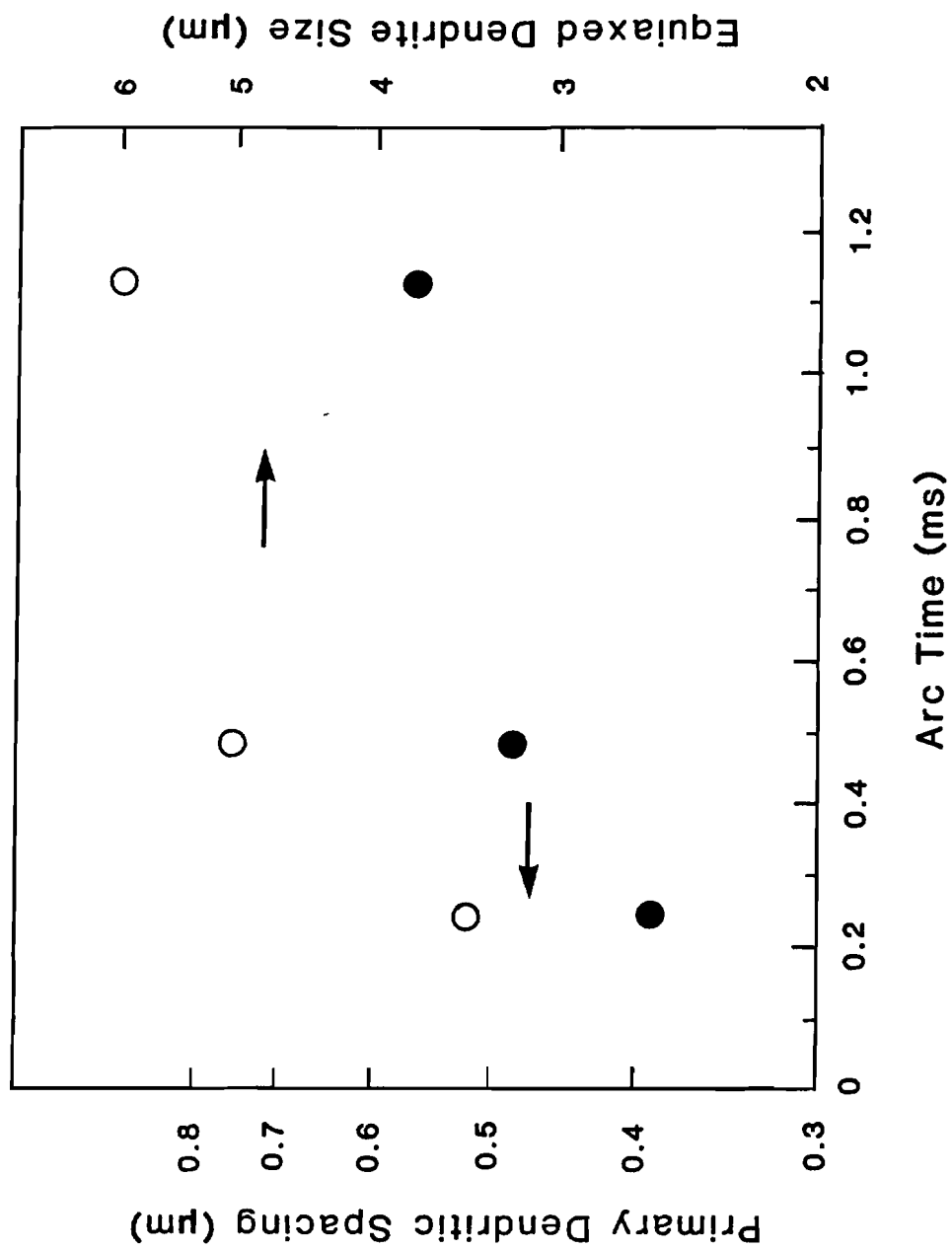
Figure 24. Average primary dendritic spacing and equiaxed dendrite diameter as functions of arc time in FeAl CD welds.
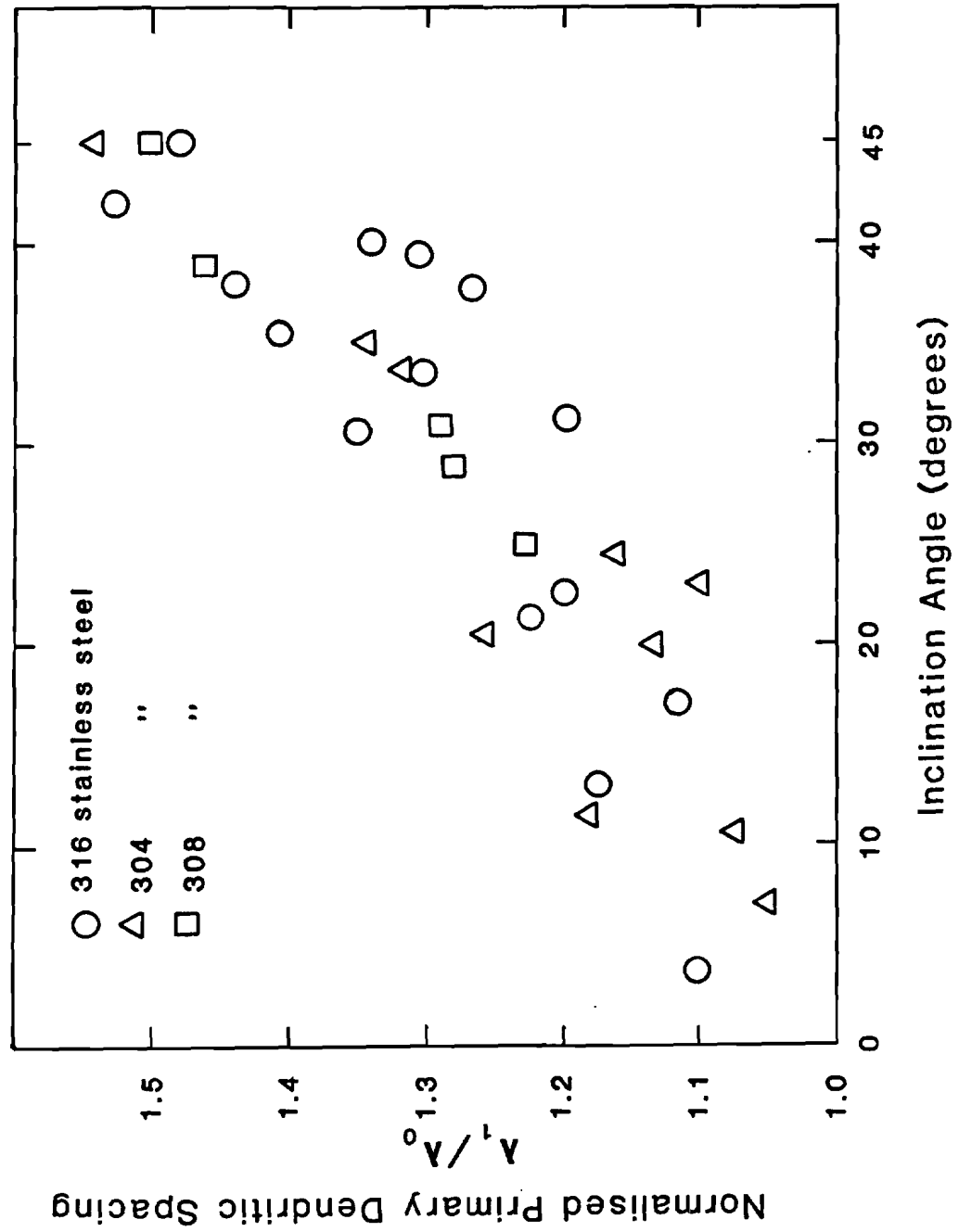
Figure 25. Normalised primary dendritic spacing as a function of inclination angle to heat flow direction.
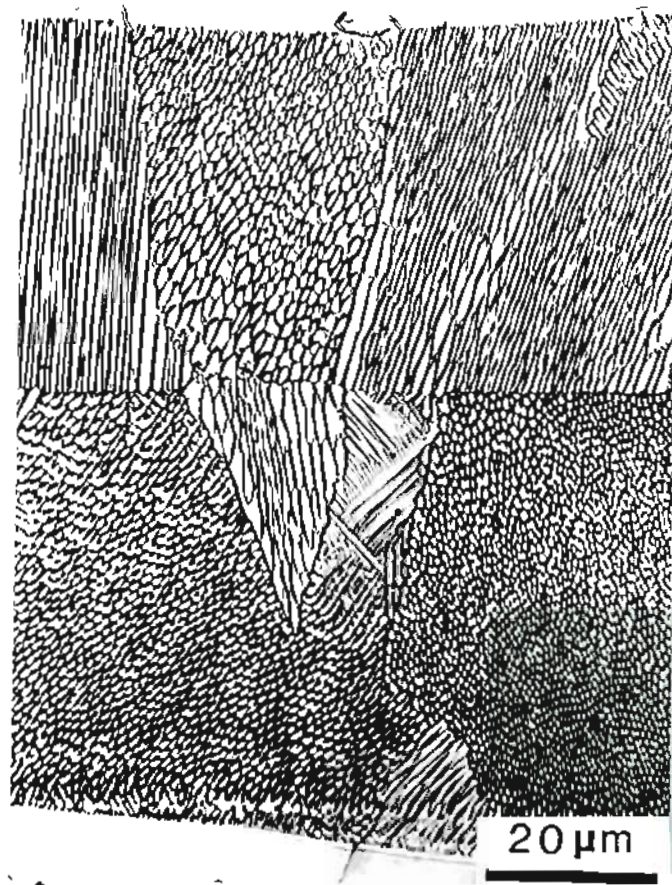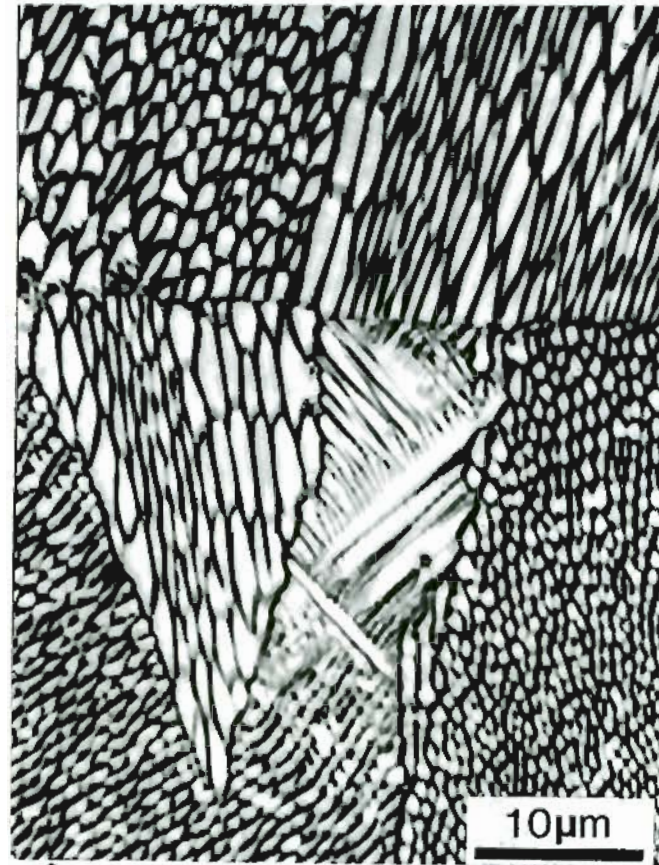
Figure 26. Dendritic structure of CD weld metal in 316 stainless steel showing: (a) side arm growth for dendrites oriented at 45 to the heat flow direction. (b) detail at higher magnification.
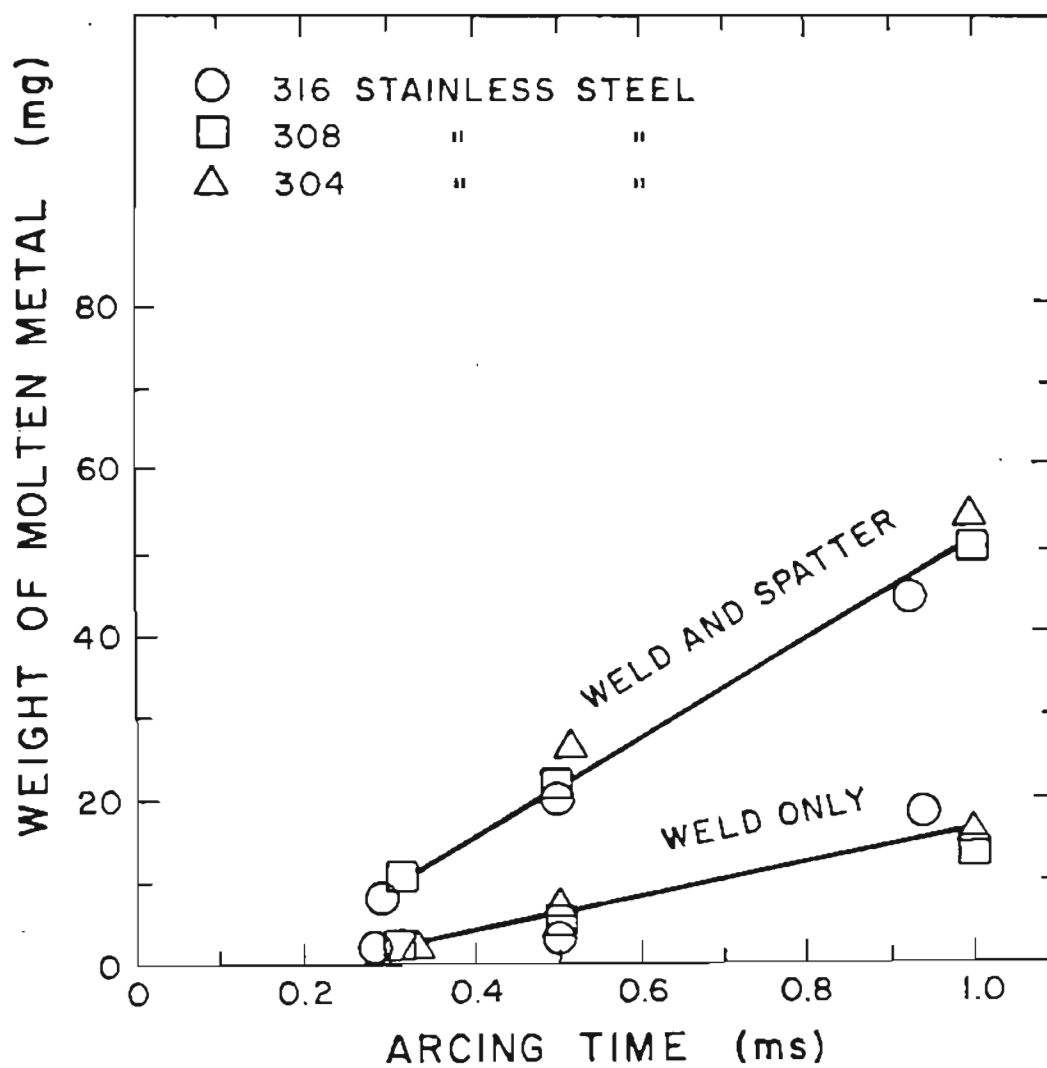
Figure 27. Weight of molten metal in weld only and including spatter as a function of arc time during CD welding of stainless steel.
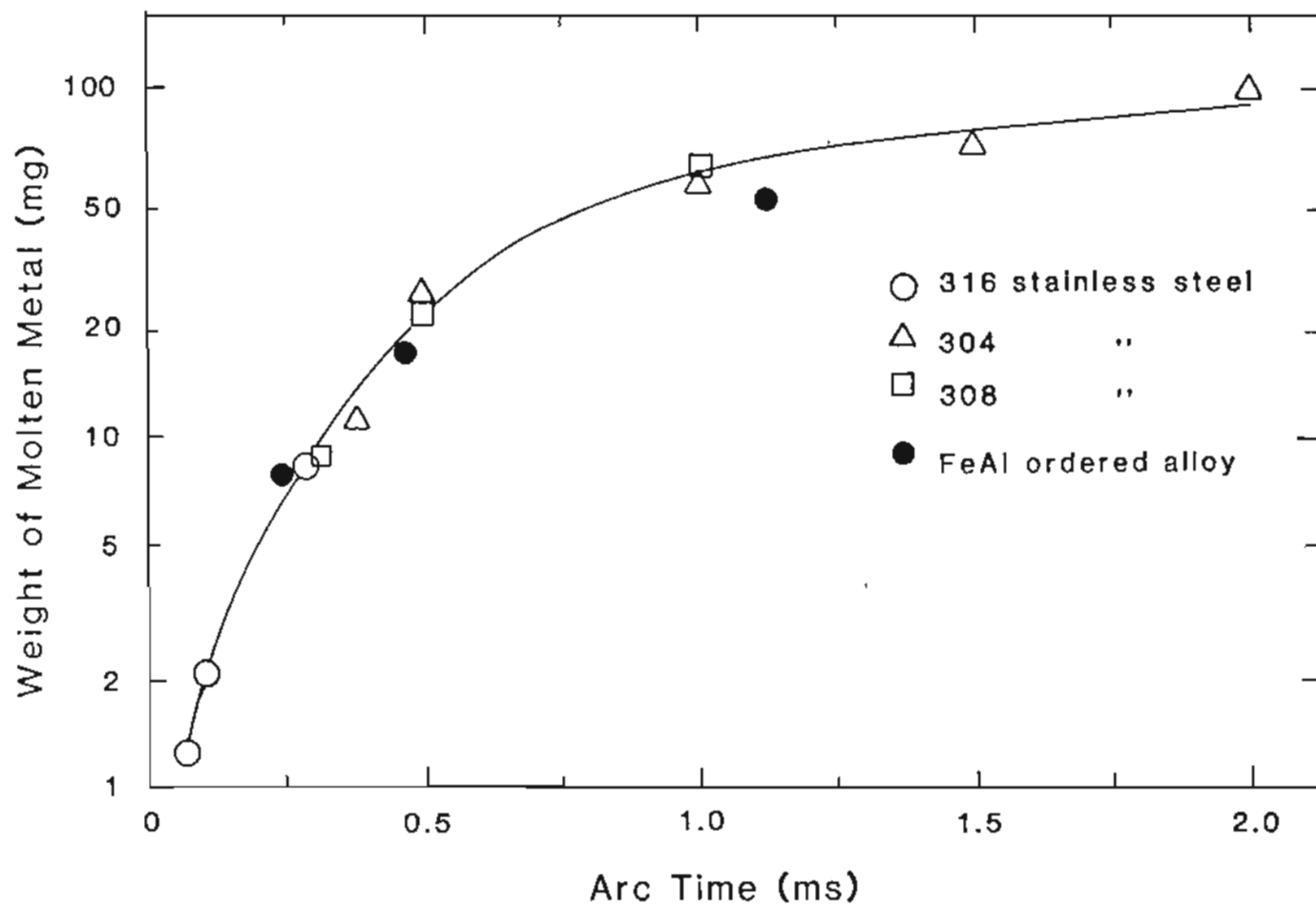
Figure 28. Weight of molten metal as a function of arc duration in
CD welding of stainless steels and FeAl ordered alloy.
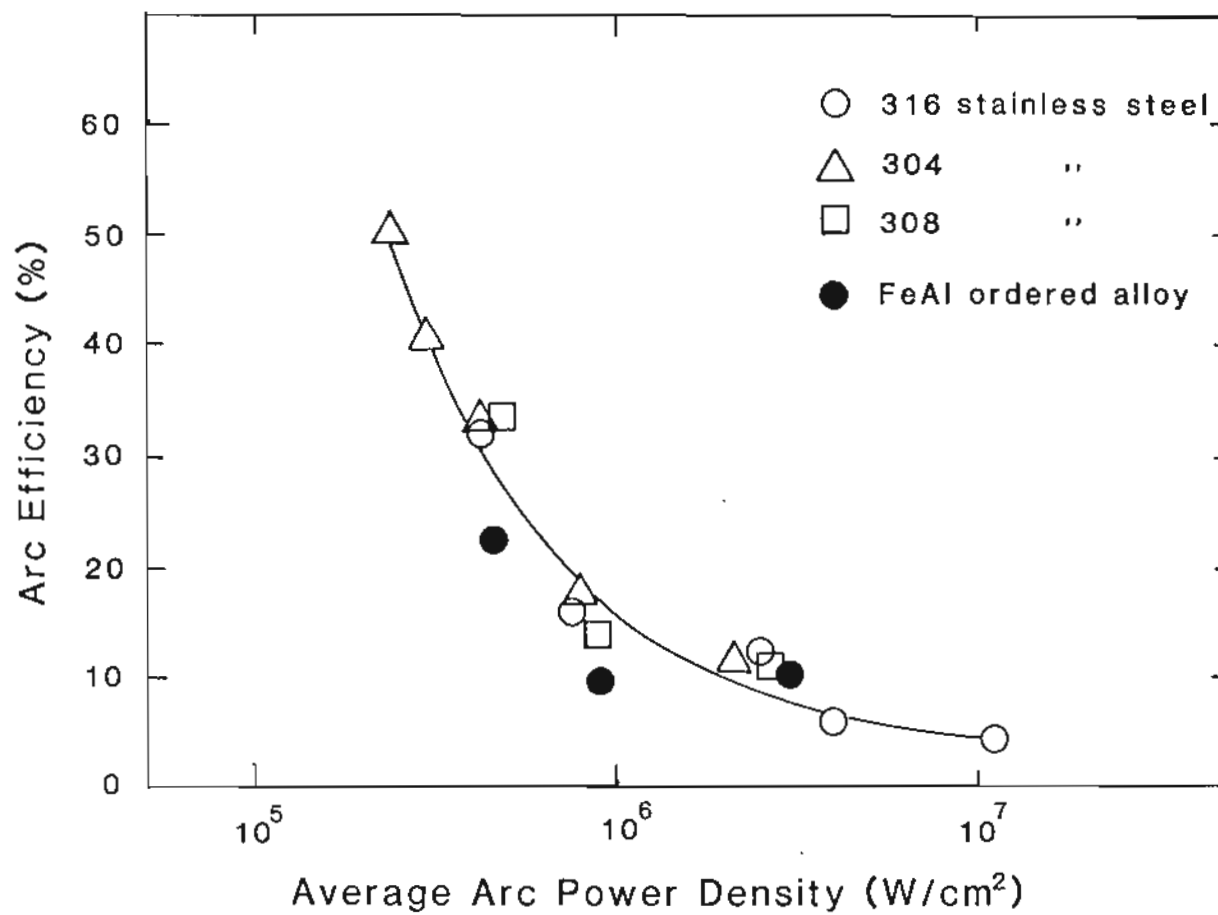
Figure 29. Variation of arc efficiency as a function of arc power density during CD welding of stainless steels and FeAl ordered alloy.
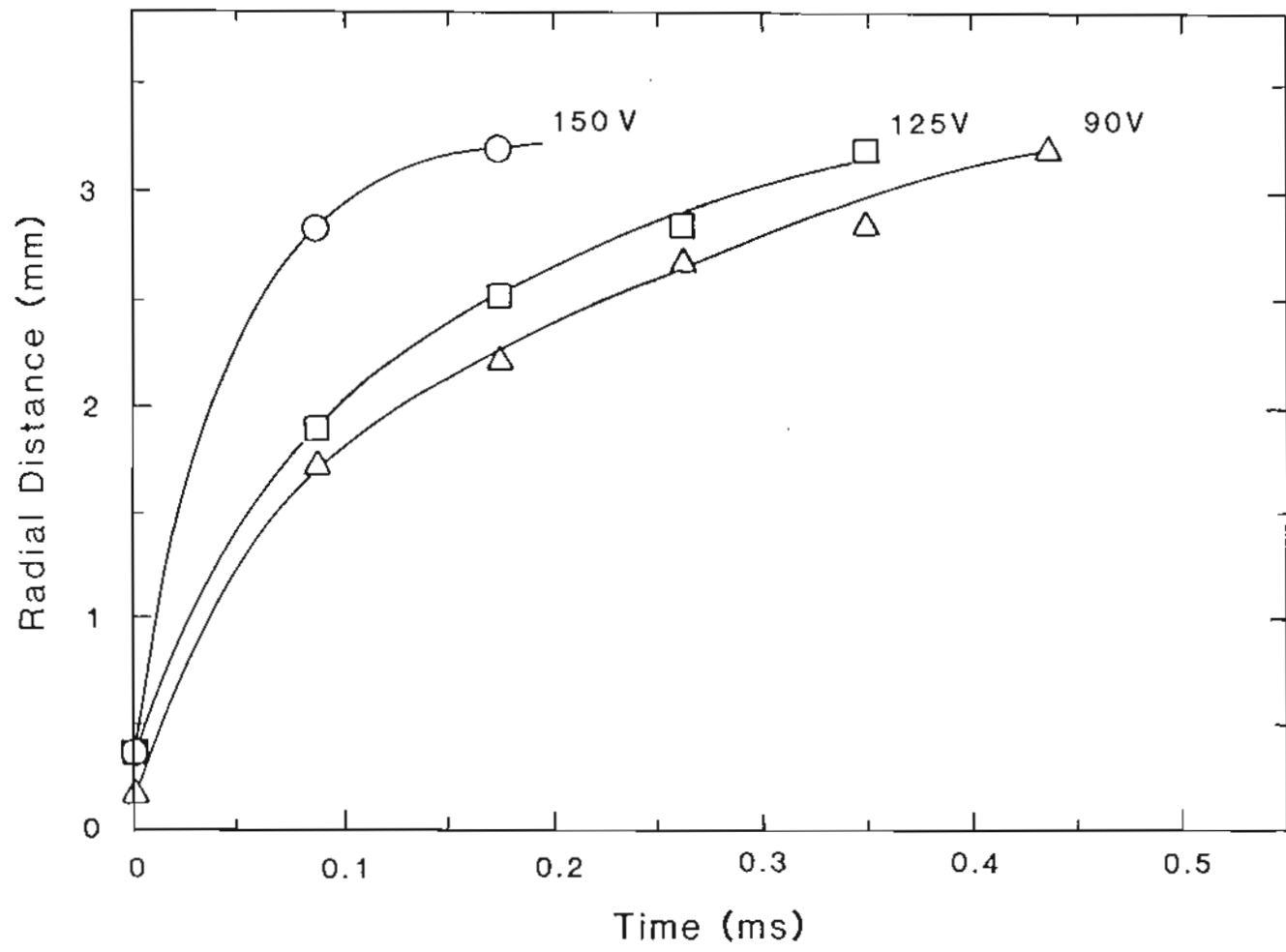
Figure 30. Radial spread of the CD welding arc as a function of time for different voltages.
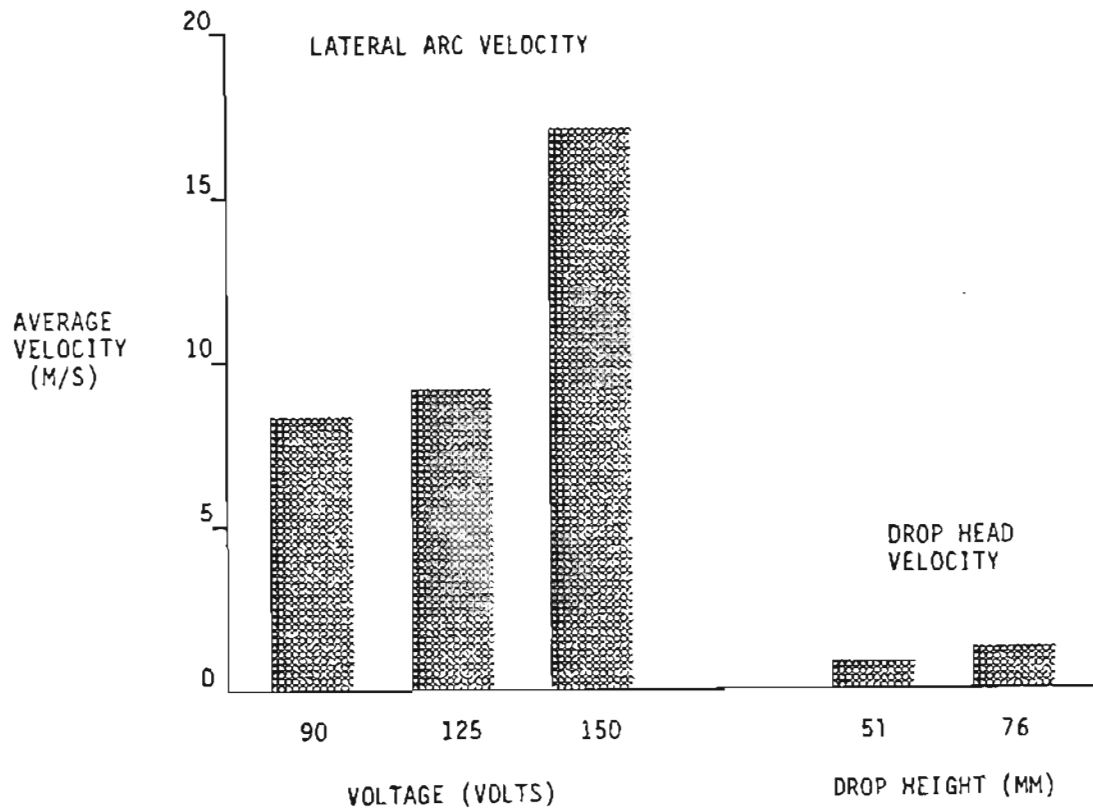
Figure 31. Average lateral arc velocity for different voltages during CD welding. Drop head velocity is also shown for comparison.
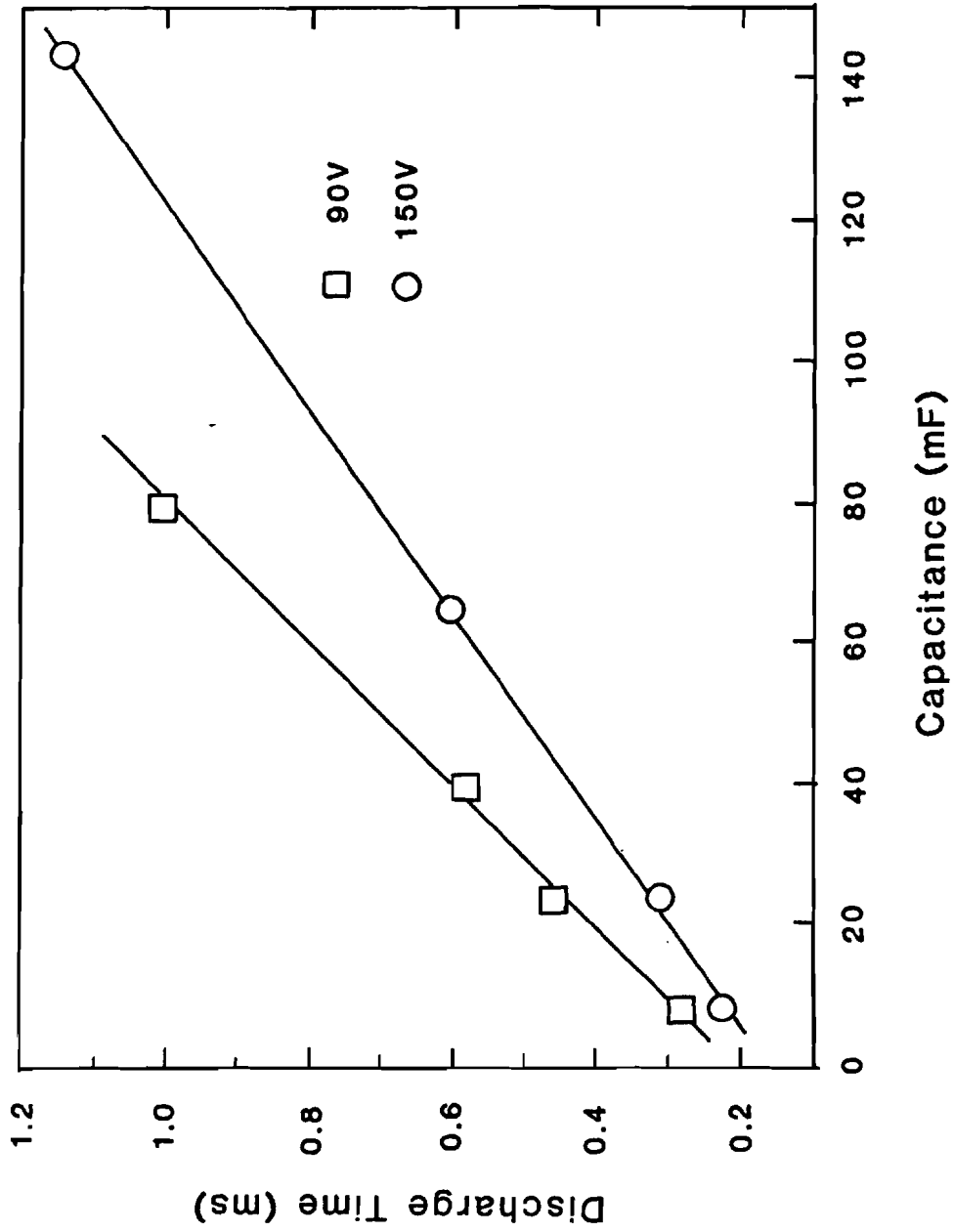
Figure 32. Discharge time to zero current as function of capacitance and voltage during CD welding.
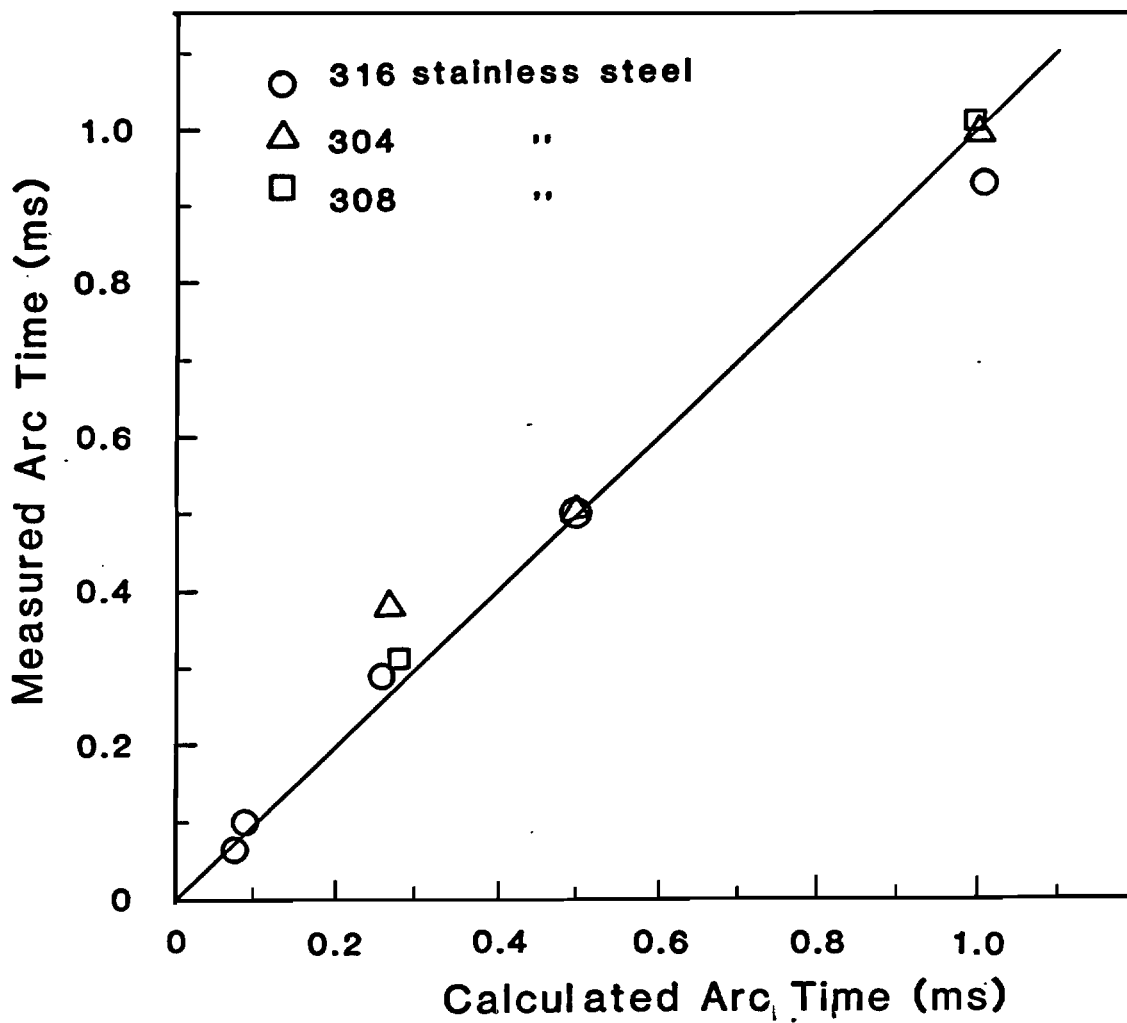
Figure 33. Arc times measured during CD welding compared with calculated times using ignition tip length and velocity of drop head under gravity.
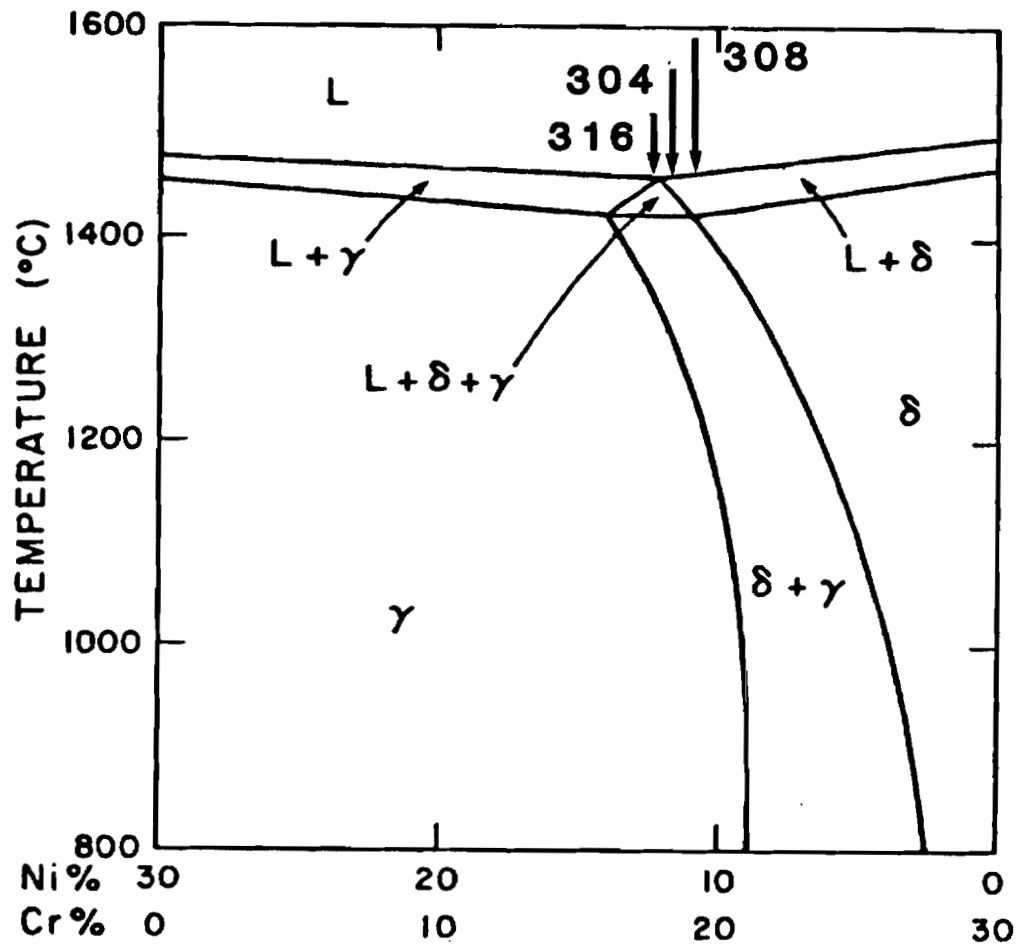
Vertical section of the Fe-Cr-Ni phase diagram at 70% Fe.

Figure 34. Position of stainless steel compositions used in the present study on the Fe-Cr-Ni phase diagram.
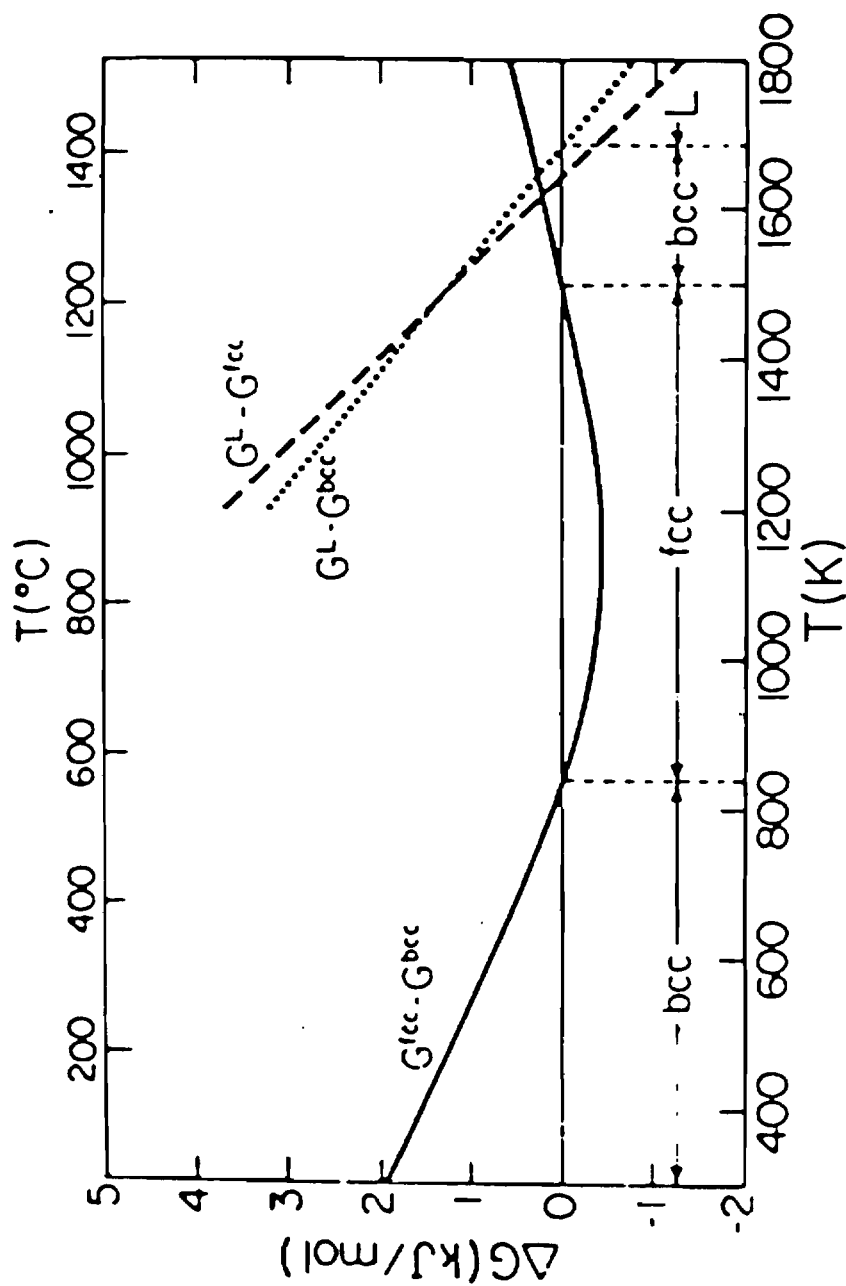
Figure 35. Relative thermodynamic stabilities of fcc and bcc phases solidifying from the liquid as a function of temperature in stainless steel. Calculation is for a Cr Eq./Ni Eq. of 1.68 (Hammar-Svensson) and alloy content of 30% (after ref.57).
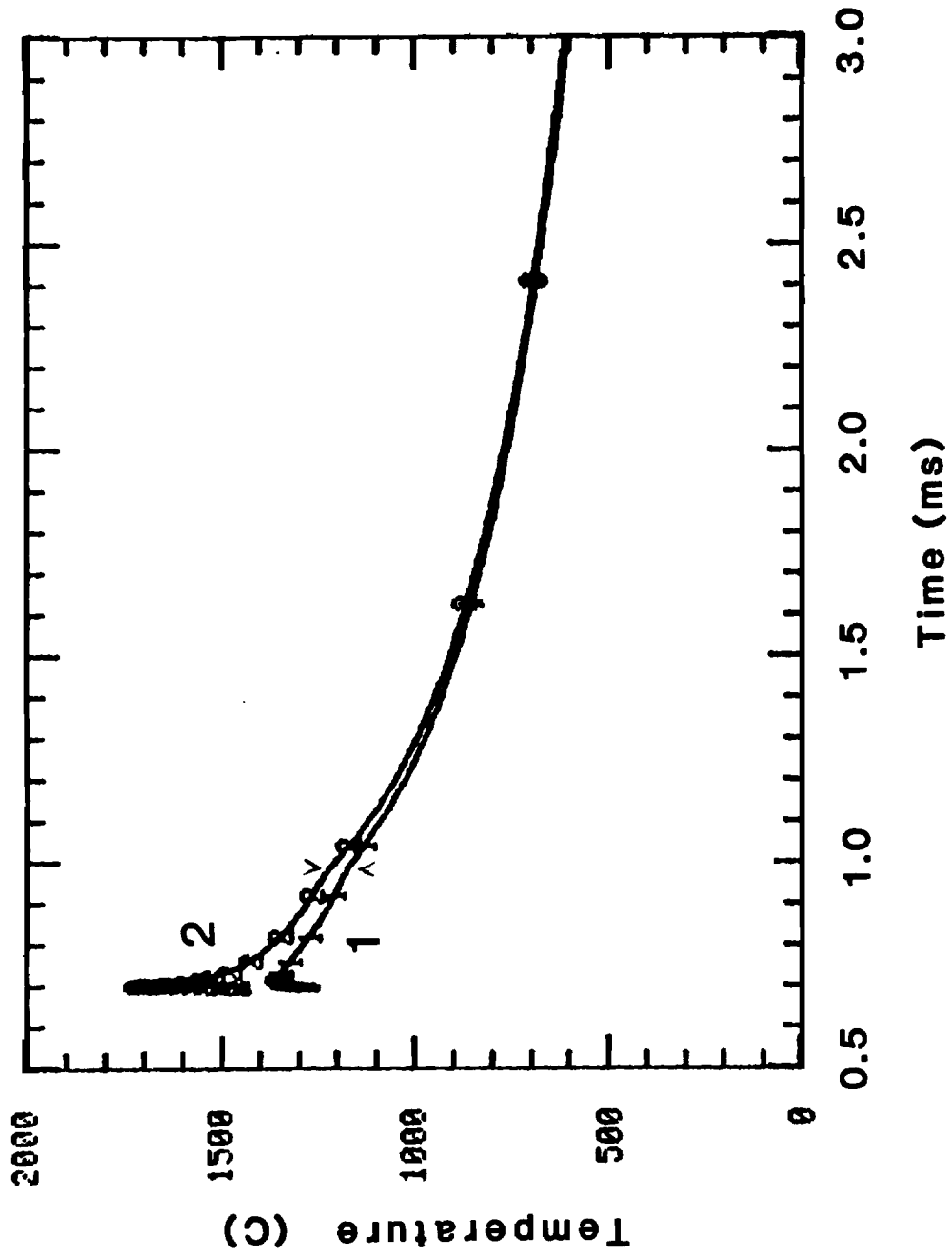
Figure 36. Cooling curves for CD weld in stainless steel with arc time 0.6 ms at: 1. weld fusion line and 2. within fusion zone. Curves were generated by Einerson et al. [82].
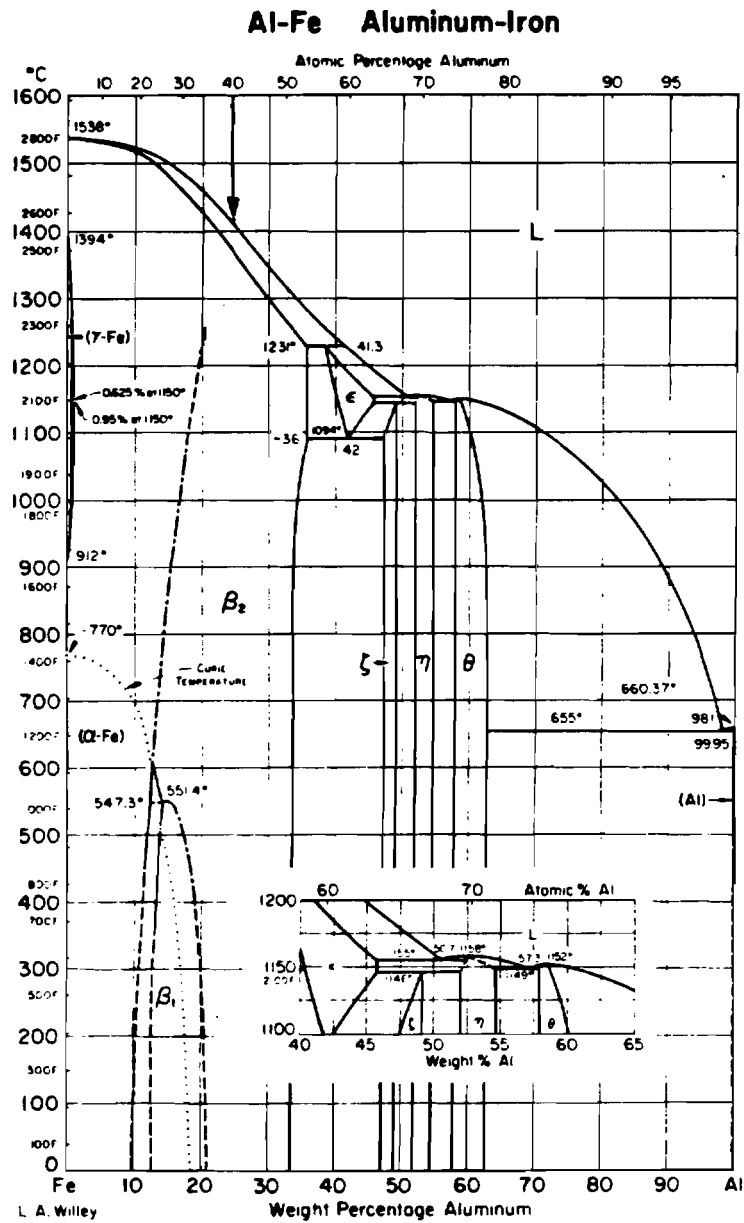
Figure 37. Phase diagram of FeAl binary system (Metals Handbook 8th edition)
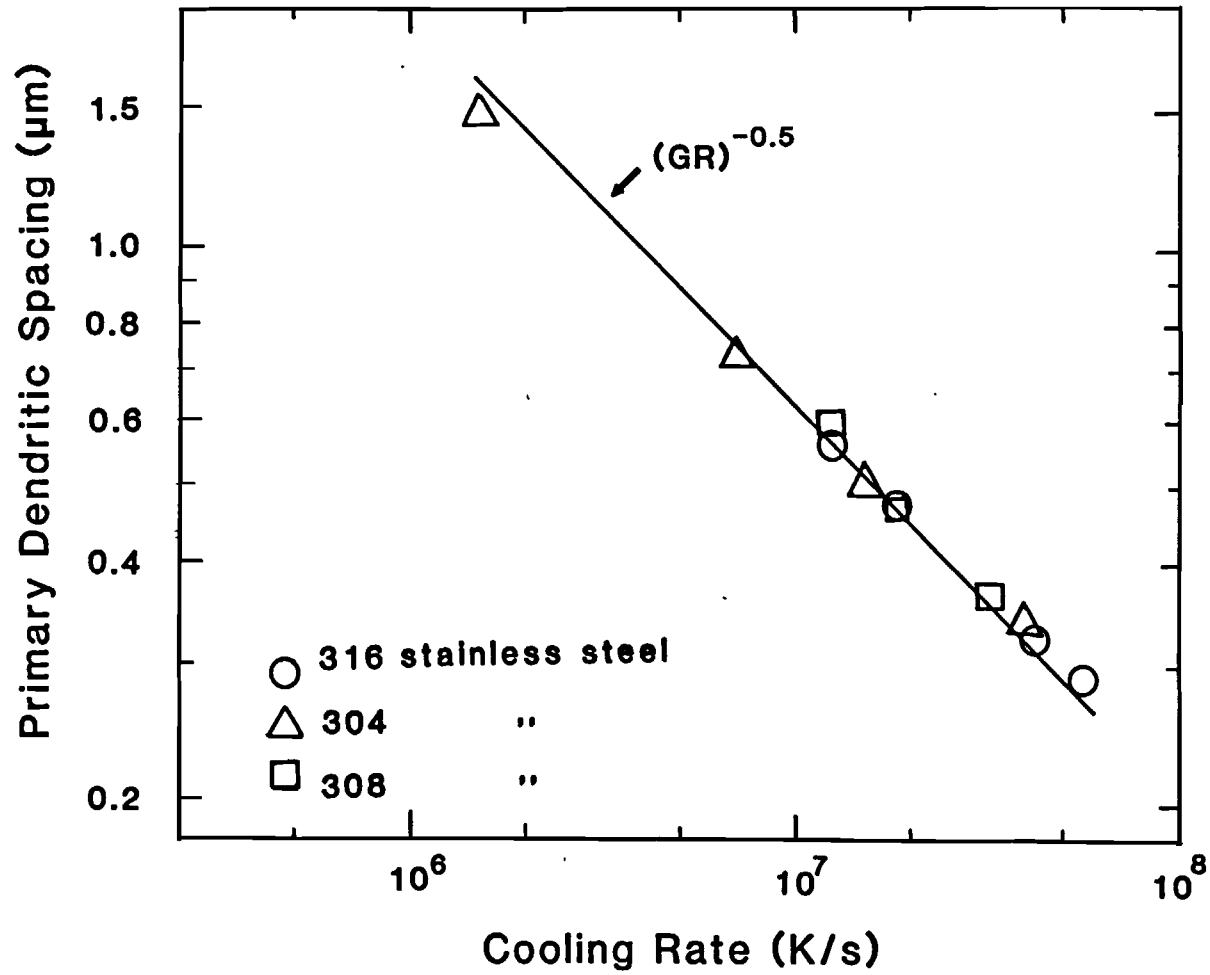
Figure 38. Primary dendritic spacing as a function of estimated cooling rate during CD welding of austenitic stainless steels. Line is relation by Okamoto [60].
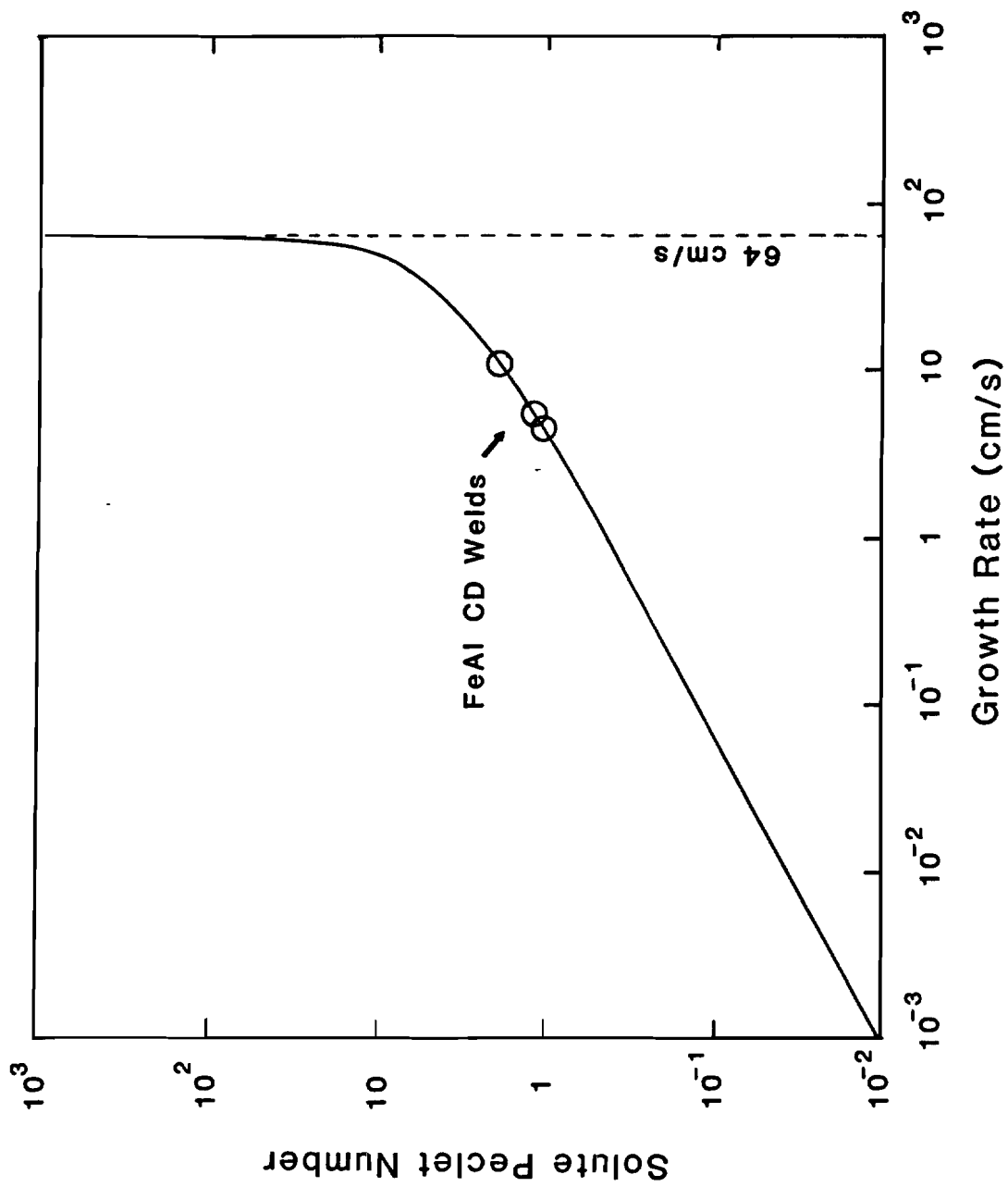
Figure 39. Solute Peclet number as a function of growth rate during solidification of FeAl ordered alloy.
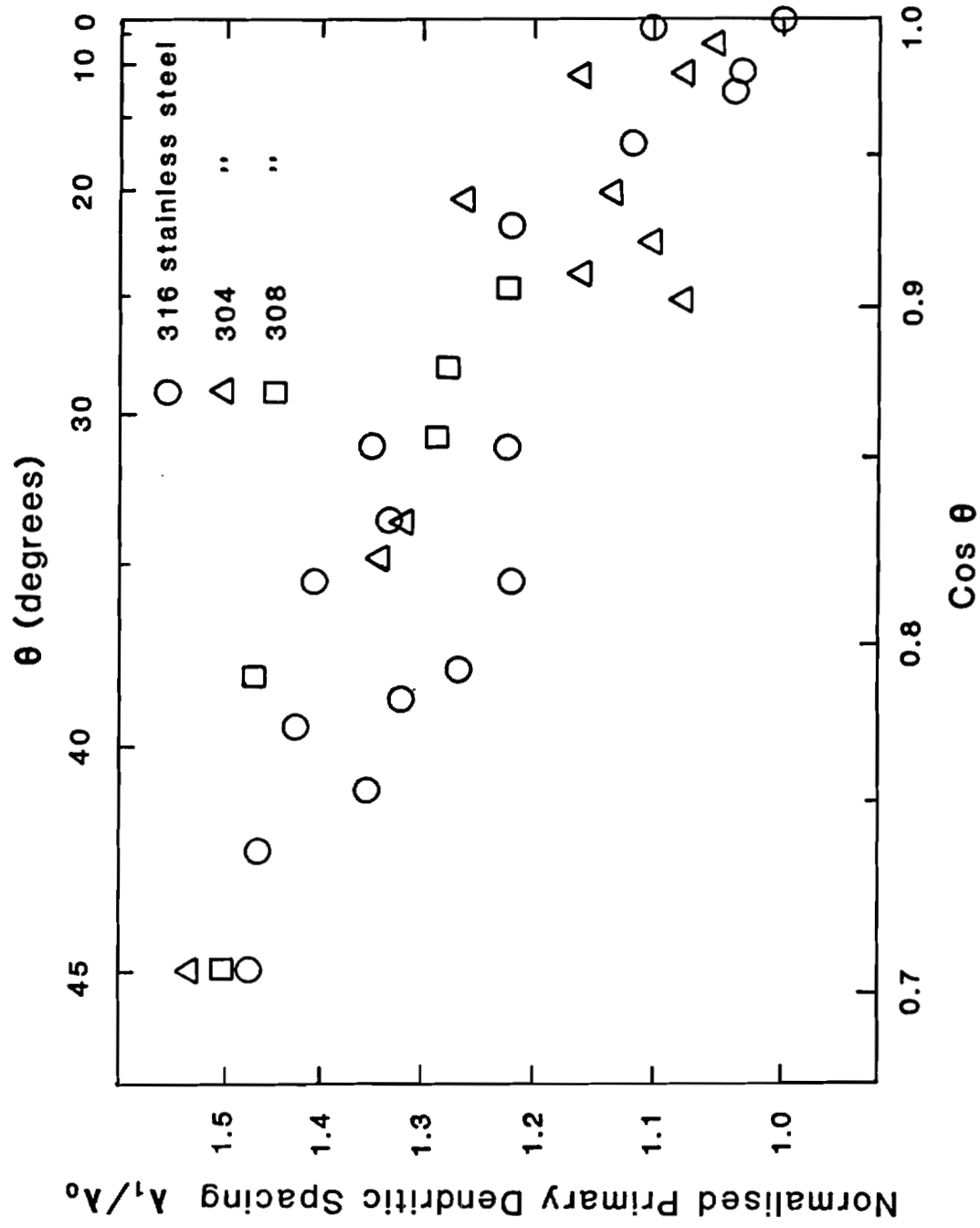
Figure 40. Normalised primary dendritic spacing in stainless steels as a function of cosine of the inclination angle to heat flow direction.
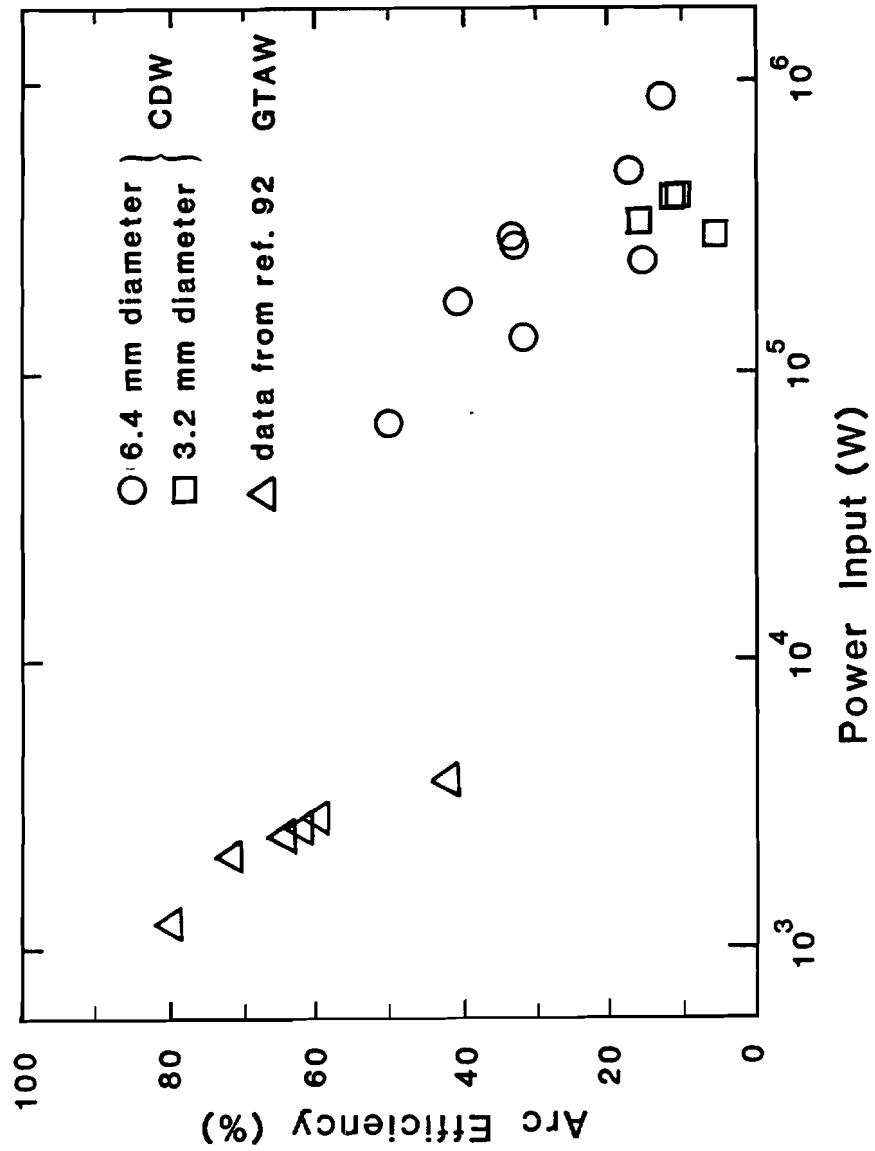
Figure 41. Comparison between arc efficiencies calculated during CD welding and values reported in literature for gas tungsten arc welding as a function of power input.

APPENDIX

For the parametric study of the CD process, welds were made on 6.4 mm diameter stainless steel, using 80 mF capacitance. Drop height, drop weight, voltage and ignition tip dimensions were varied at two levels. Average weld thicknesses obtained are shown for each set of parameters.

WELD	DROP WEIGHT (N)	DROP HEIGHT (mm)	VOLTAGE (V)	IGNITION TIP LENGTH (mm)	AVERAGE WELD THICKNESS (μm)
BASELINE	60	51	90	1.02	90.8
2	60	51	90	0.635	65.0
3	60	51	60	1.02	79.8
4	60	51	60	0.635	72.8
5	60	76	90	1.02	82.8
6	60	76	90	0.635	51.2
7	60	76	60	1.02	61.1
8	60	76	60	0.635	58.1
9	130	51	90	1.02	95.0
10	130	51	90	0.635	71.0
11	130	51	60	1.02	61.5
12	130	51	60	0.635	50.4
13	130	76	90	1.02	78.8
14	130	76	90	0.635	65.0
15	130	76	60	1.02	47.0
16	130	76	60	0.635	41.4

BIOGRAPHICAL NOTE

The author was born on March 27, 1962, in Mysore, India. He attended the Little Flower High School in Salem between 1969 and 1978 and obtained his Pre-University Degree Certificate from St. Joseph's College, Tiruchirappalli, in 1979.

In August 1979 he joined the Regional Engineering College, at Tiruchirappalli and graduated with a B. E. Honours degree in Metallurgical Engineering in 1984. Due to close association with the Welding Research Institute at Tiruchirappalli, the author developed an interest in welding and solidification. This led him to join the Welding Research Program at the Oregon Graduate Center, Beaverton, Oregon, USA, in September 1984. The requirements for the Master of Science Degree were completed by October 1986.